Development of hybrid UV VCSEL with organic active material and dielectric DBR mirrors for medical, sensoric and data storage applications

Dissertation zur Erlangung des akademischen Grades eines Doktors
der Ingenieurwissenschaften (Dr.-Ing.) im
Fachbereich Elektrotechnik / Informatik
der Universität Kassel

vorgelegt von
Dipl.-Ing. Daniel Boychov Todorov, M.Sc.

Kassel, October 2008

Erklärung

Hiermit versichere ich, dass ich die vorliegende Dissertation selbständig und ohne unerlaubte Hilfe angefertigt und andere als die in der Dissertation angegebenen Hilfsmittel nicht benutzt habe. Alle Stellen, die wörtlich oder sinngemäß aus veröffentlichten oder unveröffentlichten Schriften anderer Personen entnommen sind, habe ich als solche kenntlich gemacht.

Kein Teil dieser Arbeit ist in einem anderen Promotions- oder Habilitationsverfahren verwendet worden.

Kassel, den 10.2008

Betreuer: (Supervisor)	Prof. Dr. Hartmut Hillmer
Prüfungskommision: (Board of Examiners)	Prof. Dr. Hartmut Hillmer (1. Gutachter)
	Prof. Dr. J. Salbeck (2. Gutachter)
	Prof. Dr. Arno Ehresmann (Beisitzer)
	Prof. Dr.-Ing. Albert Claudi (Beisitzer)
Tag der mündlichen Prüfung: (Day of oral examination)	05.06.2009

Zusammenfassung

Laser spielen eine wichtige Rolle bei medizinischen, sensorischen und Datenspeicher Anwendungen. Diese Arbeit befasst sich mit der Technologieentwicklung und Herstellung von hybriden oberflächenemittierenden Lasern mit vertikaler Kavität (engl.: *Vertical-Cavity Surface-Emitting Laser; VCSEL*) die im ultraviolettem Spektrum emittieren. Die Strukturen bestehen aus organischen, aktiven Materialien und anorganischen Bragg-Spiegeln (engl.: *Distributed Bragg Reflector; DBR*).

Vielschichtstrukturen, bestehend aus anorganischen Materialien mit unterschiedlichen Brechungsindizes und Extinktionskoeffizienten, wurden untersucht durch Simulation von theoretischem Model. Während die Simulationen die Strukturparametern, wie verwendete Materialien und Schichtdicke wurden geändert. Dabei wurden zwei Arten von VCSEL-Strukturen untersucht. Bei der ersten Struktur handelt es sich um einen index-gekoppelten Laser, der einen unteren und einen oberen dielektrischen DBR Spiegel besitzt. In dem Raum zwischen den beiden Spiegeln befindet sich die Kavität, welche die aktive Zone beinhaltet und somit die Emissionswellenlänge bestimmt. Bei dieser Ausführung liegt das Maximum des elektrischen Feldes in der Kavität und kann das aktive Material überlastet. Der zweite Laser-Typ ist der sogenannte komplex-gekoppelte VCSEL. Bei dieser Art wird das aktive Material nicht nur in der Kavität platziert, sondern zum Teil auch in der DBR-Struktur. Die Simulationen zeigen, dass diese Verteilung des aktiven Materials die Lasing-Schwelle erniedrigt. Eine höhere Effizienz wird erreicht, wenn man das dielektrische Material mit hohem Brechungsindex durch aktives Material in der unmittelbaren Nähe zur Kavität ersetzt.

Die anorganischen Materialien für die DBR-Spiegel wurden sowohl mit *Plasma-Enhanced Chemical Vapor Depostion (PECVD)* als auch *Dual Ion Beam Sputtering (DIBS)* Maschinen abgeschieden und optimiert. Alle Prozesse wurden in Reinräumen der Klasse 1 und 10000 ausgeführt. Die optischen Eigenschaften und die Schichtdicke wurden *in-situ* durch ein spektroskopisches Reflektometer und spektroskopisches Ellipsometer bestimmt. Die Oberflächenrauhigkeit wurde mit einen Rasterkraftmikroskop (engl.: *Atomic Force Microscope, AFM*) analysiert. Bilder von den Strukturen wurden mit einem Rasterelektronenmikroskop (engl.: *Scanning Electron Microscope, SEM*) aufgenommen.

Die Siliziumoxid (SiO_2) und die Siliziumnitrid (Si_3N_4) Schichten, die mit der PECVD Maschine hergestellt wurden, weisen Defekte in der Materialstruktur sowie Absorption im UV-Bereich auf. Dies führt zu geringer Reflektivität der Bragg-Spiegel und verringert die optischen Eigenschaften der VCSEL-Struktur. Auf der anderen Seite kann die Spannung in den Schichten variiert und kompensiert werden.

Die Zerstäubungsmaschine *Ionsys 1000* der Fa. Roth&Rau wurde verwendet um Schichten aus Siliziumdioxid (SiO_2), Siliziumnitrid (Si_3N_4), Aluminiumoxid (Al_2O_3) und Zirkoniumdioxid (ZrO_2) herzustellen. Die Prozesskammer ist mit einer Haupt- (Zerstäubungs-) und einer Hilfsionenquelle bestückt. Die dielektrischen Materialien wurden durch Zufluss von zusätzlichem Sauerstoff beziehungsweise Stickstoff optimiert. DBR-Spiegel mit unterschiedlichen Materialien wurden abgeschieden. Die gemessenen optischen Eigenschaften der hergestellten Multischichtstrukturen zeigen eine hervorragende Übereinstimmung mit den Ergebnissen der theoretischen Modellkalkulation. Die mit der Zerstäubungsmethode hergestellten Schichten weisen hohe Kompressionsspannung (hohen Druck) auf.

Als aktives Material wurde ein neuartiges organisches Material mit einer Spiro-Verbindung benutzt. Zwei Substanzen wurden mittels einer Farbstoffverdampfungsanlage im Reinraum des Instituts Makromolekulare Chemie und Molekulare Materialien (mmCmm) aufgedampft. Das organische Material Spiro-Octopus-1 hat ein Emissionsmaximum von 395 nm; Spiro-Sexi-Phenyl liegt bei 418 nm. Beide haben einen hohen Brechungsindex und können mit einem Material mit niedrigem Brechungsindex, wie Siliziumdioxid (SiO_2) kombiniert werden.

Die abgeschiedenen Materialien mit der Zerstäubungsmethode weisen eine hohe Qualität auf und die Multischichtstrukturen zeigen eine hohe Reflektivität. Die unteren DBR-Spiegel wurden für alle VCSEL mit der DIBS-Anlage hergestellt, wohingegen die oberen DBR-Spiegel entweder mit der PECVD oder mit der PECVD und der DIBS Anlage hergestellt wurden. Die VSCSEL Strukturen wurden optisch mit einem Stickstoff-Laser mit einer Wellenlänge von 337 nm angeregt. Die Emission wurde mit einem Spektrometer aufgenommen. Strahlung des VCSEL bei einer Wellenlänge von 392 nm und 420 nm wurde beobachtet.

DOCTORAL DISSERTATION

Dipl.-Eng. Daniel Boychov Todorov, M.Sc.

Development of hybrid UV VCSEL with organic active material and dielectric DBR mirrors for medical, sensoric and data storage applications

Kassel, October 2008

Abstract

Lasers play an important role for medical, sensoric and data storage devices. This thesis is focused on design, technology development, fabrication and characterization of hybrid ultraviolet Vertical-Cavity Surface-Emitting Lasers (UV VCSEL) with organic laser-active material and inorganic distributed Bragg reflectors (DBR).

Multilayer structures with different layer thicknesses, refractive indices and absorption coefficients of the inorganic materials were studied using theoretical model calculations. During the simulations the structure parameters such as materials and thicknesses have been varied. This procedure was repeated several times during the design optimization process including also the feedback from technology and characterization. Two types of VCSEL devices were investigated. The first is an index coupled structure consisting of bottom and top DBR dielectric mirrors. In the space in between them is the cavity, which includes active region and defines the spectral gain profile. In this configuration the maximum electrical field is concentrated in the cavity and can destroy the chemical structure of the active material. The second type of laser is a so called complex coupled VCSEL. In this structure the active material is placed not only in the cavity but also in parts of the DBR structure. The simulations show that such a distribution of the active material reduces the required pumping power for reaching lasing threshold. High efficiency is achieved by substituting the dielectric material with high refractive index for the periods closer to the cavity.

The inorganic materials for the DBR mirrors have been deposited by Plasma-Enhanced Chemical Vapor Deposition (PECVD) and Dual Ion Beam Sputtering (DIBS) machines. Extended optimizations of the technological processes have been performed. All the processes are carried out in a clean room Class 1 and Class 10000. The optical properties and the thicknesses of the layers are measured *in-situ* by spectroscopic ellipsometry and spectroscopic reflectometry. The surface roughness is analyzed by atomic force microscopy (AFM) and images of the devices are taken with scanning electron microscope (SEM).

The silicon dioxide (SiO_2) and silicon nitride (Si_3N_4) layers deposited by the PECVD machine show defects of the material structure and have higher absorption in the ultra violet range compared to ion beam deposition (IBD). This results in low reflectivity of the DBR mirrors and also reduces the optical properties

of the VCSEL devices. However PECVD has the advantage that the stress in the layers can be tuned and compensated, in contrast to IBD at the moment.

A sputtering machine Ionsys 1000 produced by Roth&Rau company, is used for the deposition of silicon dioxide (SiO_2), silicon nitride (Si_3N_4), aluminum oxide (Al_2O_3) and zirconium dioxide (ZrO_2). The chamber is equipped with main (sputter) and assisted ion sources. The dielectric materials were optimized by introducing additional oxygen and nitrogen into the chamber. DBR mirrors with different material combinations were deposited. The measured optical properties of the fabricated multilayer structures show an excellent agreement with the results of theoretical model calculations. The layers deposited by sputtering show high compressive stress.

As an active region a novel organic material with spiro-linked molecules is used. Two different materials have been evaporated by utilizing a dye evaporation machine in the clean room of the department Makromolekulare Chemie und Molekulare Materialien (mmCmm). The Spiro-Octopus-1 organic material has a maximum emission at the wavelength $\lambda_{emission}$ = 395 nm and the Spiro-6ϕ has a maximum emission at the wavelength $\lambda_{emission}$ = 418 nm. Both of them have high refractive index and can be combined with low refractive index materials like silicon dioxide (SiO_2).

The sputtering method shows excellent optical quality of the deposited materials and high reflection of the multilayer structures. The bottom DBR mirrors for all VCSEL devices were deposited by the DIBS machine, whereas the top DBR mirror deposited either by PECVD or by combination of PECVD and DIBS. The fabricated VCSEL structures were optically pumped by nitrogen laser at wavelength $\lambda_{pumping}$ = 337 nm. The emission was measured by spectrometer. A radiation of the VCSEL structure at wavelength 392 nm and 420 nm is observed.

Table of contents

Chapter 1

Introduction and motivation

1.1. Background and history of Lasers

Nowadays the LASER (acronym for **L**ight **A**mplification by the **S**timulated **E**mission of **R**adiation) is one of the most important inventions in the world. It can be used not only in the science but also in the everyday live. LASERs are used to determine the distance, to communicate [1; 2], to store and retrieve information, and to fix not only machines but the human body as well [3].

In 1917, the concept about LASERs is first proposed by Albert Einstein. He has shown that light consists of wave energies called photons. Each photon has an energy that corresponds to the frequency of the waves. Einstein and S. N. Bose have developed the laser theory based on the phenomenon that the photons have tendency to travel together [4].

The precursor to the LASER is the MASER (acronym for **M**icrowave **A**mplification by **S**timulated **E**mission of **R**adiation). In 1954, Charles Townes and Arthur Schawlow have invented the maser, using ammonia gas and microwave (MW) radiation. The technology is very close but does not use a visible light.Soon after masers, the scientists have begun to look at the possibility of stimulated emission in other regions of the electromagnetic spectrum. In 1958, Charles Townes and Arthur Schawlow have developed a theory about a laser, which could use infrared or visible light. The first practical laser is invented by a physicist named Theodore Maiman. This laser is used a pink ruby crystal surrounded by a flash tube enclosed within a polished aluminium cylindrical cavity cooled by forced

air. Two years later, a continuous lasing ruby is made by replacing the flash lamp with an arc lamp.

Just before the end of 1960 (published 1961) Ali Javan, William Bennet, and Donald Herriot have made the first gas laser using helium and neon. This type of laser (a He-Ne laser) became the dominant laser for the next 20 years until cheap semiconductor lasers has been investigated and put on the market in the mid-80's.

In 1962, laser action in a semiconductor material is demonstrated by Robert Hall and researchers at General Electric. After about another decade the first semiconductor diode laser, which could operate at room temperature, has been developed. In 1975, Diode Laser Labs of New Jersey is introduced the first commercial room-temperature semiconductor laser.

1.2. State of the art of VCSEL

As the laser power has increased, semiconductor lasers have expanded into other applications. Since 1995, the production of high-power diode lasers has jumped by a factor of 25. In 1999, laser-diode revenues represented 64% of all lasers sold, up from 57% in 1996, and were reached 69% in 2000. In terms of units sold, semiconductor lasers have accounted for about 99% of the total (over 400 million units), which means most laser light is now produced directly or indirectly (via diode pumping) by semiconductor lasers. In addition to industrial applications, semiconductor lasers are being used as pump sources for solid state lasers and fibre lasers, in graphics applications such as colour proofing and digital direct-to-plate printing, and for various medical and military applications. In 2000, *Laser Focus World* estimated that about 34% of medical therapy lasers are of the semiconductor type.

The Vertical-Cavity Surface-Emitting Lasers (VCSELs) [5; 6; 7; 8] and Edge-emitting lasers [9; 10] represent one of the most important classes of lasers in use today. The laser light of the Surface-emitting lasers propagates in the direction perpendicular to the semiconductor wafer surface. Whereas in case of the Edge-emitting lasers the laser light propagates in a direction along the wafer surface of the semiconductor chip and is reflected or coupled out at a cleaved edge.

The edge-emitting lasers are the original and still very widely used form of semiconductor lasers. Their resonator length is typically between a few hundred

micrometers and a few millimeters. This is sufficient for reaching a high gain, so that an edge-emitting laser may lase even if the resonator losses are higher than the losses in the DBRs resonator. Within the edge-emitting laser structure, the laser beam is guided in a waveguide structure. A heterostructure is used to restrict the generated carriers to a narrow region and at the same time to serve as a waveguide for the optical field. This arrangement leads to a low threshold pump power and a high efficiency.

The surface-emitting lasers are the newer type of semiconductor lasers. The device structure consists of two semiconductors Bragg mirrors with active section in between. The major challenge of the VCSEL structure is to reach the laser threshold, because the optical gain for the intracavity laser beam occurs only on a very small distance. It is therefore necessary to realize a laser resonator with very low losses, i.e., Bragg mirrors with high reflectivity. Other type of surface-emitting lasers is the vertical external cavity surface-emitting lasers (VECSELs). It has only a single Bragg mirror on the chip, and the resonator is completed with an external mirror. Such lasers allow much higher output powers in diffraction-limited beams.

There are several advantages of producing VCSELs compared with the production process of edge-emitting lasers. Edge-emitters cannot be tested until the end of the production process. If the edge-emitter does not work, whether due to bad contacts or poor material growth quality, the production time and the processing materials have been wasted. The VCSELs emit the beam perpendicular to the active region of the laser which is opposite to the parallel emission by an edge emitter, tens of thousands of VCSELs can be processed simultaneously on the wafer and tested. VCSELs are tested “on-wafer” at several stages throughout the process to check for material quality and processing issues, before they are cleaved into individual devices. This reduces the fabrication cost of the devices. It is possible to be built the VCSELs not only in one-dimensional, but also in two-dimensional arrays. The larger output aperture of VCSELs, compared to most edge-emitting lasers, produces a lower divergence angle of the output beam, and makes high coupling efficiency with optical fibers possible. The high reflectivity mirrors, compared to most edge-emitting lasers, reduce the threshold current of VCSELs, resulting in low power consumption. However, the VCSELs have lower emission power compared to edge-emitting lasers. The wavelength of VCSELs may be tuned, within the gain band of the active region or by adjusting the thickness of the cavity [11]. Today, VCSELs have replaced edge-emitting lasers in applications for short-range fiberoptic communication.

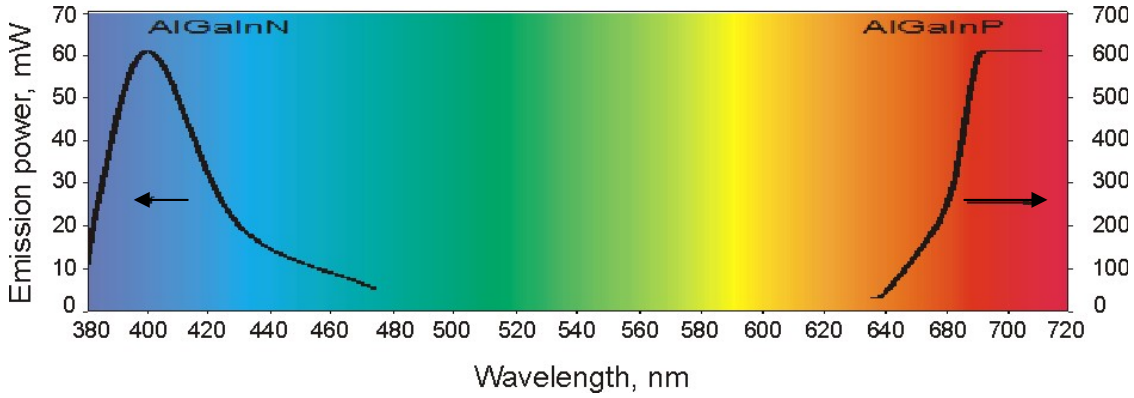

Fig. 1-1. Spectrum of the available semiconductor lasers on the market (the black solid lines).

In Fig. 1-1 the spectrum of the available semiconductor lasers on the market in the visible range is shown. From the graphic it can be seen that the phosphate (P) semiconductor lasers cover the red and near-infrared (NIR) wavelength range and the nitride (N) semiconductor lasers cover the blue range. The not covered wavelengths are the ultraviolet region and the green region.

The standing increase of the information in the data bases and the quality of the multimedia pushes the technology to search for novel high-dense data storage devices. Starting from the CD, which works at wavelength in the infrared range (IR) of the spectrum, the technology follows the tendency and goes to shorter wavelengths (see Table 1-1). The newest data storage device uses high-tech blue semiconductor laser, which finds application in Blu-Ray Discs. The coming generation will use a micro-laser with UV light. It is calculated, that such a device will reach capacity over 100 GB on a single compact disc. In the medicine the UV lasers are used for irradiation and investigation of biological samples [12]. In the sensoric it can be used for detection of hazardous gases and evaluation of concentrations.

Table 1-1. Tendency in the capacity of the data storage devices:

CD	DVD	Blu-Ray / HD	Under investigation (UV Laser)
λ = 780 nm	λ = 650 nm	λ = 405 nm	λ < 300 nm
Capacity: 0.78 GB	Capacity: 4.7 GB	Capacity: 25 GB	Capacity: > 100 GB

For the active region of the III/V or II/VI semiconductor laser an inorganic active material is used. Photoluminescence and optical amplification is achieved by organic active materials as well [13; 14; 15]. Such materials have recently attracted the interest of many research groups because of their physical properties and potential applications in light-emitting devices [16; 17; 18]. Since that time many afford have been directed towards the realization of cheap solid-state organic-based laser devices for diagnostic applications, displays, and data storage.

The organic active materials have some big advantages compared to the inorganic materials:

- the optical properties can be tailored by changing the molecular structure of the materials [19; 20; 21].
- the materials and the deposition methods are cheaper.
- the organic material can be deposited on larger aria [22].
- the emission spectrum of the organic materials is very broad and there are materials which cover almost the whole visible range [12; 23; 24].

Schneider has reported for the first time on the optically pumped DFB organic semiconductor laser operating in the deep blue wavelength range [25]. The radiation of the laser is tuned from 401,5 to 434,2 nm depending on the grating period. Two years later, he has succeeded optically to pump organic DFB laser with emission in the ultraviolet wavelength region between 377.7 and 395 nm [12]. The device uses the novel spiro-linked material with name 2,2',7,7'-tetrakis(4-fluorphenyl)spiro-9,9'-bifluorene.

Optically pumped organic Vertical-Cavity Surface-Emitting Laser (VCSEL) with polymer active material is first demonstrated by Tessler and Friend in 1996 [26]. Two years later Bulovic has used for the laser structure [27] organic material with small molecules based on the host-guest system [28].

Only several materials do not have absorption in the ultraviolet range. These are the oxides of some metals like Al_2O_3, ZrO_2, HfO_2 and SiO_2. They are used for high reflective multilayer structures in different optical devices [29; 30; 31].

Persano has reported in 2006 for the first time on an organic VCSEL with single mode lasing at 509 nm and linewidth of 1,8 nm [32]. He has used spin-coated conjugated copolymer (poly[(9,9-dioctylfluorenyl-2,7-dily)-co-(1,4-diphenylene-vinylene-2-methoxy-5-{2-ethylhexyloxy}-benzene)]) on the bottom DBR as an active material. The bottom and the top mirrors have been made by

deposition of titanium dioxide (TiO_2) and silica dioxide (SiO_2) multilayer structure. To reduce the damages of the organic layer the top DBR has been deposited by low temperature reactive (in oxygen atmosphere) electron-beam deposition method. As a result reduction of the optical properties of the top mirror has been observed. To compensate that it has been deposited with 3 periods more (9,5 periods) than the bottom DBR (7,5 periods). Several months later by utilizing the same procedure Persano has reported for optically pumped organic VCSEL with emission at 443 and 456 nm [33].

The organic VCSEL devices with emission in the deep blue, violet and ultraviolet range stay unexplored. The main effort of this work is concentrated on the simulation, optimization and deposition of hybrid VCSEL structures in the ultraviolet range with dielectric DBR mirrors and organic active material.

Chapter 2

Foundations of technological processes, theory of VCSELs and basics of organic materials

2.1. Foundations of technological processes

There are many of technologies for deposition of different materials. Basically, thin-film deposition methods are either purely physical, such as evaporative methods, or purely chemical, such as gas- and liquid-phase chemical processing. The deposition technologies can be categorized in four different types of processes: evaporative, glow-discharge, gas-phase chemical and liquid-phase chemical processes [34]. In this work thin films were deposited and investigated using two deposition methods: ion beam deposition and plasma enhanced chemical vapor deposition.

2.1.1. Ion Beam Deposition (IBD) method

The sputtering is extensively used in the semiconductor industry to deposit thin films of various materials in integrated circuit processing. Thin antireflection coatings on glass for optical applications are also deposited by sputtering [35]. Because of the low substrate temperatures, sputtering is an ideal method to deposit dielectric layers on organic materials or contact metals for thin-film transistors. Sputtering is also used for deposition of Aluminum metal layer during the fabrication of CD and DVD discs.

Ion beam deposition (IBD) method is based on the sputtering technology [36; 37; 38]. IBD uses an energetic, broad beam ion source carefully focused on a grounded metallic or dielectric sputtering target [39].

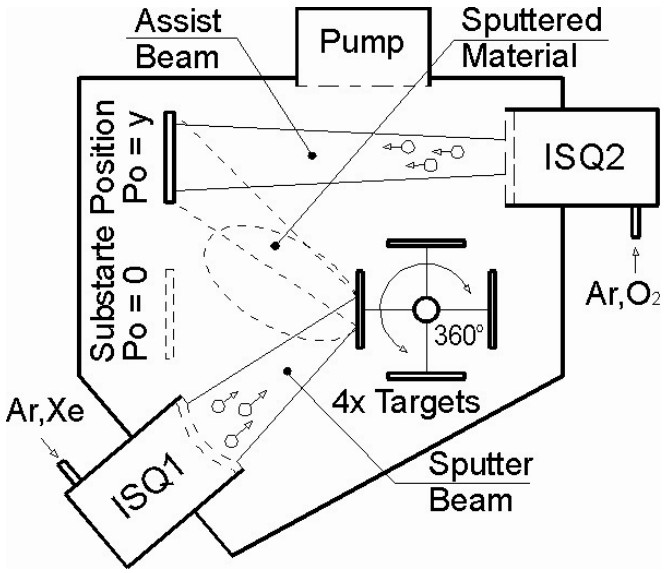

Fig. 2-1. Schematic diagram of ion beam deposition machine with second ion assisted source. The first ion source is used for sputtering of the target and the ion assisted source is used for modification of the deposited material on the substrate and introduction of oxygen or nitrogen in the chamber.

Sputtered atoms ejected into the gas phase are not in their thermodynamic equilibrium state, and tend to deposit on all surfaces in the vacuum chamber. A substrate, such as a silicon (Si) wafer, placed in the chamber will be coated with a thin film. Sputtering usually uses an argon (Ar) or xenon (Xe) plasma. The Xe has standard atomic weight of 131.293 g mol^{-1} and it is used for sputtering of hard materials. The Ar is much lighter and has standard atomic weight of 39.948 g mol^{-1} Some applications also use a second ion assist source (IAD) directed at the substrate to deliver energetic noble or reactive ions at the surface of the growing film. In Fig. 2-1 schematic diagram of ion beam deposition machine with second assisted ion source is shown. The ion source used for sputtering is called ISQ1 and the assisted ion source is called ISQ2. IAD is particularly desirable for metal oxide and metal nitride films as it improves the stability, density, dielectric and optical properties of the films [40].

2.1.1.1. Sputtering mechanisms

Sputtering is the removal of material from the surface of a solid through the impact of energetic particles. The material released from the bombarded surface consists predominantly of single atoms and sometimes sizable fraction of homo- or heteronuclear clusters.

The ions are mostly used as energetic particles. By their impinging on the surface of the solid, several processes are initiated:

1) A small fraction of the incident ions is backscattered in collisions with surface and near-surface atoms. The backscattered particles are mostly neutral atoms with a broad energy distribution. The backscattered yield depends on the energy and mass of the incident ions, as well as on the mass of the target atoms [41; 42; 43; 44; 45; 46].

2) The major fraction of the incident ions is slowed down in collisions with atoms and electrons of the solid. The energy and the momentum, which can be transported back to the surface, may cause also sputtering as a secondary effect [47].

3) At the end of their range the injected projectiles could be trapped and accumulated in the solid. Depending on their chemical properties and temperature of the host material, they could also diffuse back to the bombarded surface or into the bulk. Implanted gaseous ions can form bubbles and cause blistering of the surface layer [47; 48].

4) Ion impact on the surface of the solid could also give rise to the emission of electrons. The electrons can be ejected by potential emission, kinetic emission or Auger emission from excited sputtered particles [47; 49].

As the incident ions are slowed down, from the collisions with the atoms and electrons, energy in excess of the lattice binding energy will be transferred to the atoms of the solid. The atoms removed from their original places are subsequently slowed down in the solid by the same mechanism as the incident ions. Knock-on atoms may also remove other atoms from their lattice places. Thus a collision cascade develops. Surface or near-surface atoms will be emitted if they receive a momentum in the direction of the vacuum half-space with enough energy to overcome the surface binding.

Generally more than 60% of the ejected atoms originate from the first atomic layer, while the remainders originate from the layers underneath [47]. The main effects of the sputtering process are presented in Fig. 2-2.

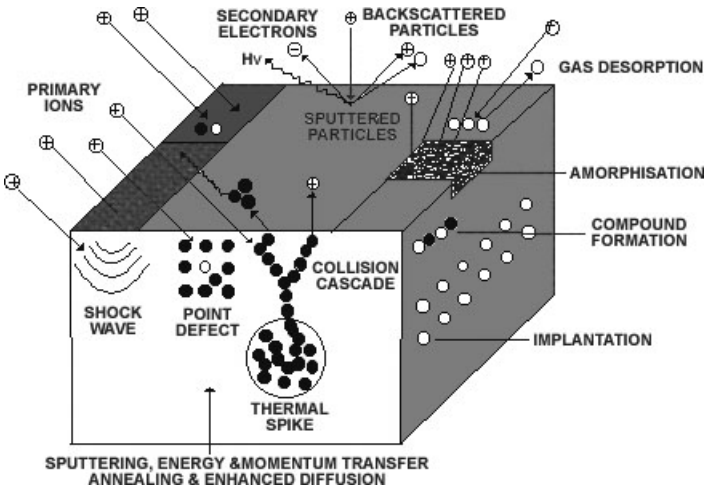

Fig. 2-2. Schematic picture of the main processes involved in ion beam sputtering of solid materials [50].

The removal of surface and near-surface atoms by knock-on sputtering, i.e. by direct momentum transfer in a collision cascade, is called physical sputtering. It is a non thermal process, with a major fraction of the lattice atoms staying stable during the initial spread of the cascade that leads to sputtering. The energy is finally dissipated in displacements of atoms and in lattice vibrations. Most of the atoms removed from their places fall back to their original location.

2.1.1.2. Sputtering yield

The most important and the most widely investigated quantity for describing the sputtering process is the sputtering yield Y_{tot}, which is defined as the average number of atoms released at the solid´s surface per incident particles. The sputtering yield depends on the mass, the energy, and the impact angle of the incident particles, on the mass and the binding energy of the atoms in the solid and at the surface [47]. The crystallinity of the sample and the orientation of low-index direction with respect to the direction of the incident particle beam [51] are important parameters as well.

The total sputtering yield is given by the following equation:

$$Y_{tot} = \frac{N_a}{N_i} \quad 2.1$$

where

N_a the number of the released atoms at the surface of the solid
N_i the number of the incident ions

A partial sputtering yield Y_i of component *i* of a multicomponent material is defined as the average number of sputtered atoms of component *i* per incident ion. Total and partial sputtering yields are then related by:

$$Y_{tot} = \sum_i Y_i \quad 2.2$$

A component sputtering yield Y_i^c is defined as the partial sputtering yield Y_i divided by the equilibrium surface concentration c_i^s of component *i* during sputtering:

$$Y_i^c = Y_i / c_i^s \quad 2.3$$

The partial sputtering yields and also the component sputtering yields generally change if the surface concentration changes during the ion bombardment. At sufficiently low temperature an equilibrium situation will be always developed under particle bombardment where the target looses material in its bulk composition. At steady-state the ratio of the number of sputtered atoms n_A of component A to the number of sputtered atoms n_B of component B must be equal to the ratio of the bulk concentrations c_A/c_B:

$$n_A / n_B = c_A/c_B \quad 2.4$$

Generally, the sputtering yield can be described by concerning two effects: the first one is describing the density of the energy created by the incident particles into nuclear motion of the target atoms near the surface, and the another effect is the material factor, which shows the atomic density and the surface binding energy of the solid [47]. In Table. 2-1 sputtering yields of different materials sputtered with Ar gas and ion beam energy 500 eV are shown.

Table. 2-1. Sputtering yields of different materials sputtered with Ar gas and ion beam energy 500 eV. The pure materials have higher yield, whereas the oxide compounds have lower yield.

Material	Sputter yield
Silver	2.80
Copper	2.00
Gold	1.70
Al	1.00
Si	0.50
SiO_2	0.23
Al_2O_3	0.05

The threshold energy E_{th} characterizes the sputtering yield and has typically value at about 20-50 eV. This is determined by the necessary energy transfer between the incident particles and the atom of the solid, as well as by the surface binding energy U_0 [52]. For bombardment energies larger then E_{th} the sputtering yield increases monotonically with the energy of the incident particles. At higher incident energies the sputtering yield decreases, because the ions penetrate more deeply into the solid and leave less energy near the surface. The sputtering yield increases with increasing the angle of incidence up to a maximum at the angle between 55° and 85° with respect to the surface normal [47]. The decrease at larger angles of incidence is related to larger particle and energy reflection [53].

In order to describe details of the collision cascades in amorphous und single crystals the cascade can be followed by a computer simulation. For an amorphous material this can be done by a Monte Carlo Program, while for single crystal all lattice positions have to be stored in the computer. For energies above 100 eV the binary collision approximation can be used, while for lower energies, a classic dynamical model should be applied. Polycrystalline material can be simulated by a superposition of the results of many differently oriented single crystals [51].

The correlation between the sputtered yield of Si, Al and Zr targets and the incident angle of the Ar ion beam with ions energy 800eV is shown in Fig. 2-3. The Zr material has considerably low sputtering yield compared to Si and Al, but the maximum by all three materials is at about 70° incident angle. The simulations are made with “SRTM2006” software [54; 55; 56; 57].

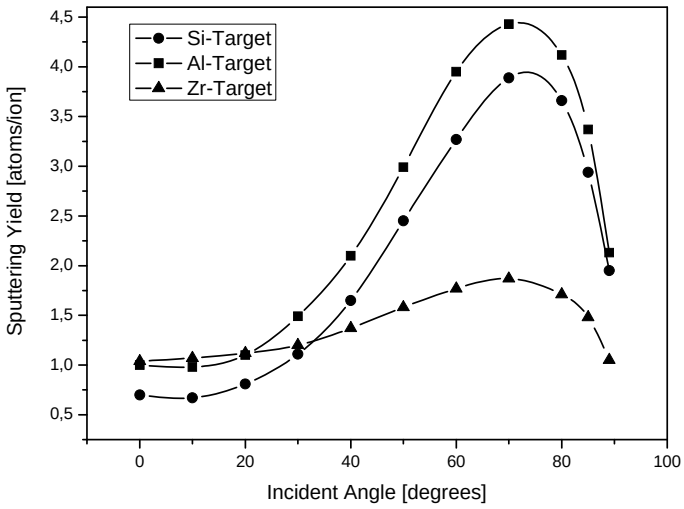

Fig. 2-3. Correlation between the sputtered yield of Si, Al and Zr targets and the incident angle of the Ar ion beam with ions energy 800 eV. At about 70° the sputtering yield has maximum. The simulation was made with program "SRTM2006" [55].

The sputtering yields of monocrystalline targets irradiated by heavy ions of energies exceeding 1 keV show a strong dependence on the crystallographic orientation of the incident beam. The angular distributions of the atoms ejected from single crystal targets showed maximum intensity in directions corresponding to the more closely spaced atomic rows passing to the target surface. This phenomenon is explained as a channeling effect.

The transparency model is used to describe the orientation effect on the yield. In this model a small sphere of radius r is located at each atomic place in the crystal. The radius is chosen so that πr^2 is the cross section for a critical interaction between the incident ions and the lattice atoms. Collisions with impact parameter $p \leq r$ contribute to the sputtering in one way, while those with $p > r$ contribute differently or not at all. Thus, from the viewpoint of the incident ion, the target crystal is an assembly of small spheres, whose size can be regard as energy dependent. If the ion beam is incident parallel to a lattice vector, some ions will collide with these spheres, but because of the translational symmetry of the crystal, the others will penetrate deeply without making collisions with $p \leq r$. This property of the lattice of dividing the beam into colliding and non colliding portions gives the name transparency [51]. Those ions which approach within a critical distance of an atomic row or plane are strongly scattered and lose all memory of their original direction. Estimates can be given of the effects of crystal orientation, ion energy, and temperature on monocrystal sputtering yields.

2.1.1.3. Angular distribution of the sputtered material

One of the very important advantages of the sputtering method is that the deposited material has the same composition as the source material. The equality of the film and target stoichiometry might be different since the sputter yield depends on the atomic weight of the atoms in the target. One component of an alloy or mixture is sputter faster than the other components, leading to an enrichment of that component in the deposited thin layer. However, since only surface atoms can be sputtered, the faster ejection of one element leaves the surface enriched with the others, effectively counteracting the difference in sputter rates. This is in contrast to thermal evaporation techniques, where one component of the source may have a higher vapor pressure, resulting in a deposited film with a different composition than the source.

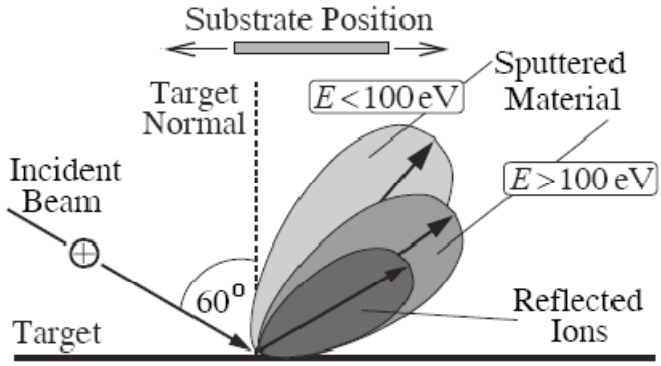

Fig. 2-4. Angular distribution of the sputtered material and the reflected ions under incident angle of 60° of the ion beam with different ion energies [58]. The shape of the sputtered material has a form close to the $\cos^n\alpha$ function.

The angular distribution of the sputtered atom flux has a form close to the $\cos^n\alpha$ function. The coefficient α is the angle between the normal of the target and the incident angle of the ion beam. In general, the deviations often take the form of an “under-cosine” distribution, which is reduced normal to the surface, or an “over-cosine” distribution, which is more peaked in the direction of the surface normal.

In case of direct knock-on regime the angular distribution is under-cosine for perpendicular incidence because the emission takes place at large polar angles. For grazing incidence the emission is mainly in the opposite direction. At intermediate energies and for size of the ions from medium to heavy, the angular

distribution is usually cosine-like, whereas at high incident energy the distribution is over-cosine, i.e. peaked in the direction of the surface normal [59].

The influence of the surface topography or bombardment-induced texturing can also be significant. In contrast to the amorphous materials, single crystal targets show a strongly anisotropic emission. An enhanced emission along the close-packed lattice direction is observed.

The energy distribution of sputtered particles allows the distinction between physical and chemical sputtering. From the different mechanisms for particle ejection in physical and chemical sputtering, differences in the energy distribution of sputtered particles are expected. For the physical sputtering in the linear collision regime the energy distribution is given by [48]:

$$\frac{dY(E_1)}{dE_1} \approx \frac{E_1}{(E_1 + U_0)^{3-2m}} \qquad 2.5$$

where

E	incident ion energy
U_0	surface binding energy
m	exponent for the interatomic potential being generally $m \approx 0.2$ to 0

For $m = 0$ this distribution has a maximum at ½ U_0 and decreases as $(1/E_1)^2$ for high energies.

2.1.1.4. Sputtering in a reactive atmosphere

By sputtering with nonreactive ions (Ar, Xe) in a reactive gas atmosphere, the deposited film is formed by chemical reaction between the material sputtered from the target and the reactive gas which is introduced into the vacuum chamber. Oxide and nitride films are often fabricated using reactive sputtering. The composition of the film can be controlled by varying the relative pressures of the inert and reactive gases. In case of utilizing second assisted ion source (AIS) the reactive gas can by introduced in the vacuum chamber in ionized form. Reactive ion beam can be used for surface modification of the deposited thin layers. Film stoichiometry is an important parameter for optimizing the functional properties, like the stress in SiNx and the index of refraction of SiOx. Also the transparent

indium tin oxide conductor, which is used in optoelectronics and solar cells, is made by reactive sputtering.

The reactive gas introduced in the vacuum chamber reacts chemically with the metal surface of the target, with the chamber walls and with the deposited material on the substrate. The condition of the oxidized target surface defines the sputtering process. By increasing the flow of the reactive gas a permanent oxidation of the target surface is observed. This sputtering regime is characterized as “oxide mode” and has low deposition rate with over oxidized deposited materials. By decreasing the partial pressure of the reactive gas the deposition rate shows a hysteresis curve (see Fig. 2-5).

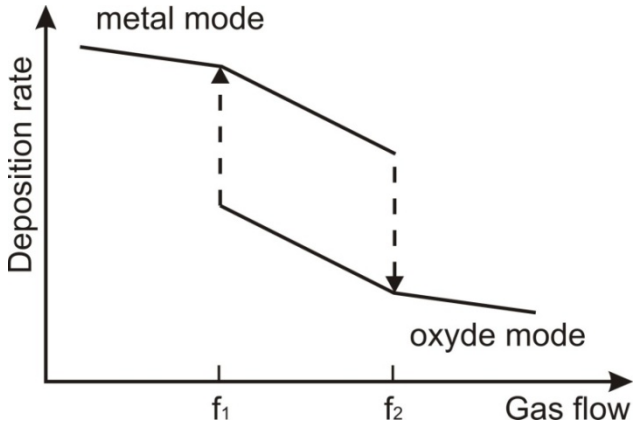

Fig. 2-5. Hysteresis curve of the deposition rate observed by changing the gas flow of the reactive gas [60]. Very interesting is the transition region from oxide to metal mode.

With further reduction of the gas flow a critical point is reached, where the deposition rate increases rapidly. The oxidized or nitrified surface of the target is sputtered and the pure material is reached. Only the sputtered atoms or clusters react with the reactive gas. The lack of the oxygen of the deposited layers with these conditions shows high absorption. This sputtering regime is characterized as “metal mode”. Very interesting is the transition region from oxide to metal mode. In this range a process with high deposition rate and low absorption is achievable.

The ion beam assisted deposition (IBAD) machine gives the possibility to change the parameters of the deposited layer by modifying its surface. A second ion beam is directed to the substrate and can be used for etching or implantation. If this ion beam works with reactive ions, like oxygen, the degree of oxidation can be controlled. High kinetic energy of the ions causes re-sputtering of the deposited

material. This can bring damages in the thin layer and higher absorption. Absorption free layers can be achieved by working with optimal oxygen pressure and small energy of the ion beam.

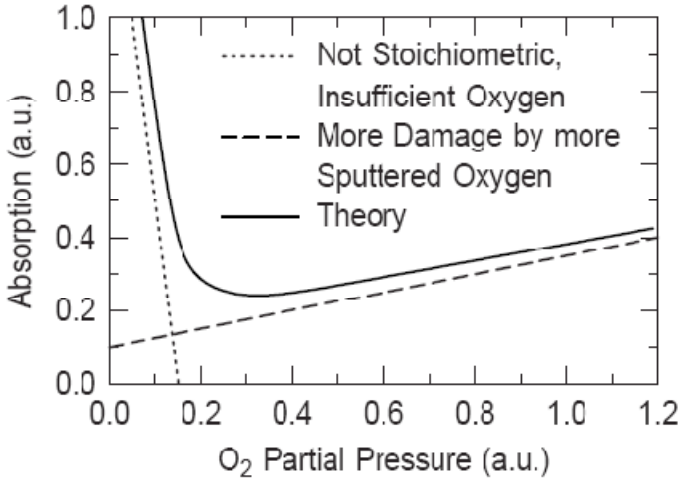

Fig. 2-6. Changes in the partial pressure of the oxygen gas shows big changes in the absorption. The lack of the oxygen of the deposited layers shows high absorption, but high oxygen pressure leads to over oxidized material.

Ion-beam sputtering (IBS) is a method in which the target is external to the ion source. An Electron Cyclotron Resonance Source (ECR) is used as an electrode free plasma device which provides highly-charged ions at low velocities [59]. The ions are generated by collisions with the electrons which are confined by the magnetic field and accelerated in phase with the microwave field (see Fig. 2-7). Thus, the free pathway of the electrons is increasing and provides high density plasma. Such plasma has lower potential and shows low corrosion of the ion source components.

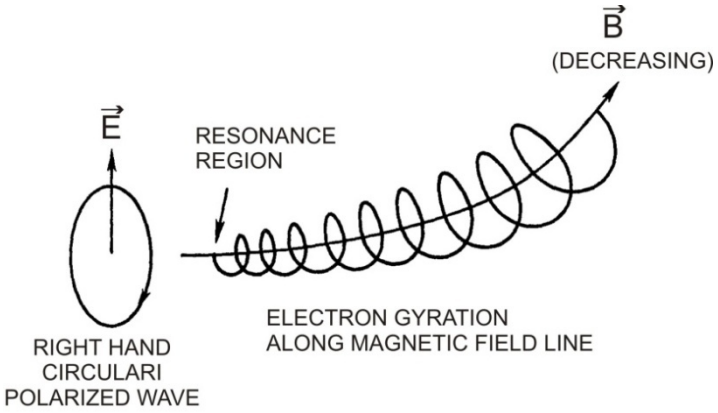

Fig. 2-7. Circularly polarized electromagnetic wave propagating along magnetic field lines [59]. The free pathway of the electrons is increasing and provides high density plasma.

The modern ion sources are equipped with two or three grid systems made by graphite or metals. They are used to confine and accelerate the ions and to form the ion beam. The spatial distribution of the electrical potential in the grid holes is the most important parameter of the beam shape. Focusing or defocusing could be achieved by utilizing of spherical grid system and the focus length is defined by the radius of the curvature. As they leave the source they can be neutralized by electrons from an external neutralizer. Another method for neutralization is the pulsing mode. In this method different modes are used for extraction of the charged particles from the plasma. The potential of the ion source is alternatively changed in range from 100 to 10000 Hz. The ion source works either in ion or electron emitting regime. The amount of the neutralization is defined by the time ratio between the two modes. IBS has an advantage in that the energy and flux of the ions can be controlled independently. Since the flux that strikes the target is composed of neutral atoms, either insulating or conducting targets can be sputtered.

IBD processing yields excellent control and repeatability of film thickness and properties. The process pressures in IBD systems are ~10-4 mBar. Hence, there is very little scattering of either ions delivered by the ion sources or material sputtered from the target of the surface. Compared to the magnetron deposition method the sputter deposition by IBD is highly directional and more energetic. In combination with a substrate fixture that rotates and changes angle, IBD systems deliver a broad range of control over sidewall coatings, trench filling and liftoff profiles. Many applications use an assembly of multiple targets that can be indexed into position to create multilayer thin film devices.

2.1.2. Plasma Enhanced Chemical Vapor Deposition (PECVD) method

Plasma Enhanced Chemical Vapor Deposition (PECVD) is an excellent method for depositing a variety of thin films at lower temperatures than those utilized in CVD reactors without disturbing the film quality. For example, high quality silicon dioxide or silicon nitride films can be deposited at 300 to 350 degrees centigrade while CVD requires temperatures in the range of 650 to 850 degrees centigrade to achieve similar quality of the films.

The PECVD is a technique in which one or more gaseous reactors are used to form a solid insulating or conducting layer. On the surface of the wafer the process is enhanced by the use of a vapor containing electrically charged particles or plasma. The deposition operates under lower temperature.

Some of the attractive properties of PECVD films are good adhesion, good step coverage, and uniformity. Plasma Enhanced Chemical Vapor Deposition offers a wide range of cost effective material processes.

The big success of the PECVD systems is because of its flexibility in deposition of different materials for the thin films such as: Silicon Nitride (SiN_x), Silicon Monoxide (SiO), Silicon Dioxide (SiO_2), Silicon Oxynitride (SiO_xN_y), Amorphous Silicon (a-Si), and Poly Silicon (poly-Si).

These films are used for many different reasons in the manufacture for example for encapsulating, scratch and particle protection, environmental protection, optical anti-reflective coatings, for masks in etching or ion implantation and for multilayer structures [61]. SiN, SiO2, SiO and SiON are all dielectrics and provide different electrical insulating properties. They are used most predominantly for separating one conductive layer from another [62]. a-Si and poly-Si are conductive materials. Depending on their doping quantities they have different conductive properties. Amorphous silicon is often used for production of solar cells.

Plasma processing is used extensively in the semiconductor industry also for etching of thin film materials. The etching process can be divided in chemical, physical or combination of both. The chemical reaction converts the material into a volatile gas which will be desorbed from the surface within the plasma environment and be pumped out of the system [63]. The physical etching is pure mechanical bombardment of the surface. The best etch results are achieved by combination of the both etch processes.

2.1.2.1. PECVD equipments

The chamber where the plasma processing occurs is the so called plasma reactor. Reactors are available in three basic configurations: barrel (or tube) reactor, planer reactor, and downstream reactor. The most popular are the first two reactors. The downstream reactor is a more recent innovation, and has some significant advantages. Different reactor design may result in a different material composition and structure, although the major deposition conditions such as substrate temperature and plasma frequency may be equal.

In the barrel system, the plasma is excited using inductive coils or capacitive electrodes outside of the quartz or glass tube. The substrate is positioned vertically and no electrically bias is applied between the wafer and the plasma. The sample is immersed in the plasma and exposed only to low-energy ion bombardment. The potential of the ions is about 30 eV [64]. High uniformity of the deposited or etched material is difficult to be achieved. This is determined by the nonuniformity in the plasma, the gas flow pattern, and the wafer temperature. The barrel system is the cheapest type for plasma process equipment.

In the traditional barrel and planer reactor the wafer is placed in the plasma generation chamber and is therefore immersed within the plasma. In downstream reactor the wafer is separated from the plasma. This type of PECVD is called remote plasma-enhanced chemical vapor deposition (RPECVD).

The RPECVD has several advantages. First, the particles with high kinetic energy remain in the plasma chamber and do not impinge on the wafer. This reduces the electronic damage. The equipment is configured so that the chemically excited species can reach the substrate. Another major advantage is that the secondary reactant gases can be introduced into the chamber, separate from the plasma chamber. The resulting downstream chemical reactions can produce highly reactive free radical species. Downstream reactors that use only the spaces obtained from the plasma chamber are called primary reactors while those adding downstream gas are called secondary reactors.

Although RPECVD reactors can be constructed using traditional RF discharge plasma sources, most use microwave plasma sources operating at 2.45 GHz. The microwave discharges are electrodeless. A strong electromagnetic field is established within a resonant cavity and results in gas breakdown.

The second method of coupling the microwave signal to the gas in the plasma chamber uses the principle of the electron cyclotron resonance (ECR). The ECR

concept uses a microwave energy source in a strong magnetic field to ionize gas molecules by cyclotron resonance of the outer shell electrons. The magnetic field is usually applied by solenoidal coils placed around the source cavity. A slight difference is made in the applied magnetic field, which serves to extract species from the plasma chamber and direct them toward the wafer. The ion energy is between 10 and 100 eV. The operating pressure is below 10^{-4} mbar which can result in reduced pinhole density of the thin film materials.

Compared to the barrel reactor, the planer reactor configuration can achieve high uniformity of the deposited material. The samples are generally placed horizontally on the lower electrode, which is often used to heat the wafers as well (see Fig. 2-8).

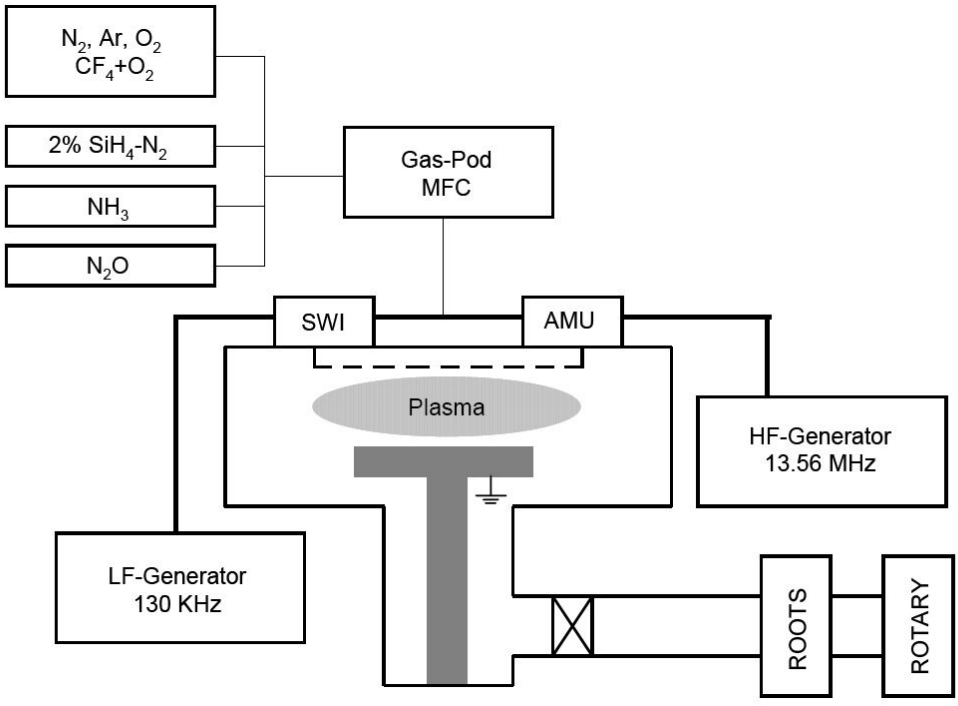

Fig. 2-8. Configuration of the plasma enhanced chemical vapor deposition (PECVD) machine (Plasma Lab 80 plus, Oxford Instruments) [65].

The radio frequency (RF) signal which excites the plasma is applied across the two electrodes. Depending on the way of inlet of the reactant gases in the plasma chamber the reactors are divided in “radial flaw” and “showerhead flow” [66].In case of the radial flow the reactant gases are introduced either at the outer

radius or on-axis, and flow radially between the electrodes. The basic redial flow planer reactor was announced in 1973 [67], and became very popular later.

As indicated in Fig. 2-8, the plasma occupies the region between the two electrodes. It can be excited by any RF, but the most popular frequency is 30 MHz. Some other plasma reactors use a much lower RF of 13.56 MHz. But this lower frequency allows the ions in the plasma to build momentum during each RF cycle. The resulting energetic bombardment of the wafer can cause electrical and mechanical damages. Such an example for electrical damages caused by mechanical damages is the decrease in the current I_{dss} in FET's. At 13.56 MHz, the ions do not have time to build up much momentum, and consequently the potential for electrical damages is much less. On the market reactors are available, which operate with both RFs (30 MHz and 13.56 MHz). By changing the duty cycle between the high and low RF some parameters of the deposited materials are possible to be controlled. Such an example is the stress control of the SiN_x thin layers [68].

The plasma is divided from the immediate vicinity of the electrode surface by electromagnetic effects. This region is called the plasma sheath or the dark region. The plasma is generally neutral, with positive species balancing negative species. However, the plasma sheath is a region of positive space charge and the electrode surfaces are negative with respect to the plasma [69]. This is due to the higher mobility of electrons which move rapidly to the surface of electrodes. The RF voltage is applied through a large blocking capacitor so that no dc bias is intentionally applied.

2.1.2.2. PECVD deposited thin films

The major materials of interest for the optical devices are silicon nitride and silicon dioxide. They are used for multilayer structures and antireflection coating.

In the optoelectronics the silicon nitride (Si_3N_4) is used as high refractive index material. It has higher dielectric constant than silicon dioxide and so is used for capacitor dielectrics. As reactive gases a combination of silane (SiH_4) and ammonia (NH_3) are used. Silane is used for the silicon source, and ammonia for the nitrogen source. Pure nitrogen (N_2) gas is possible to be used, but has bigger ionization potential than ammonia. The chemical reaction is:

$$3SiH_4 + 4NH_3 \rightarrow Si_3N_4 + 12H_2 \qquad 2.6$$

but there are many other possibilities for intermediate reactions. They are caused from the different derivatives of the silane and ammonia in the plasma, such as SiH_4, SiH_3, SiH_2, NH_3, NH_2, and ionized hydrogen. Some other elements may be present in the layer, coming from the background gasses or water. The silicon nitride plasma can contain as much as 20÷25 % hydrogen [70]. This contamination comes from the ammonia itself. The incorporation of the hydrogen is bigger by processes with lower temperature.

The Si / N ratio is a function of the operating parameters and the deposited material is not necessarily to be in stoichiometry with ratio 3 / 4. It was found that the Si / N ratio increase with increasing the deposition temperature and increasing the total pressure [71]. By decreasing of the plasma power the Si / N ratio decreases [72]. Using infrared absorption spectroscopy, in the deposited layer three different configurations for silicon-hydrogen bonding (SiH, SiH_2, SiH_3) and two for nitrogen-hydrogen bonding (NH, NH_2) were identified. Maeda and Nakamura reported that the SiH_2 and NH_2 bond are the thermally most stable groups [73].

The refractive index depends on the composition of the material. It is possible that different compositions result in the same value for the refractive index [74]. By changing the Si/N ratio the refractive index varies proportionally. The depositions are made at a constant H concentration and constant deposition temperature, with all samples prepared in one and the same reactor [75].

In the optoelectronics the silicon dioxide (SiO_2) is used as low refractive index material. The low dielectric constant makes silicon dioxide a popular choice for use as an inter-level spacer to separate metal crossovers with minimum parasitic capacitance. As explained before for silicon nitride likewise the Si / O ratio in SiO_2 material can vary from the stoichiometric value 1 / 2. A certain amount of hydrogen is also found in the deposited material. PECVD of silicon dioxide is generally done by using silane as the silicon source and nitrous oxide (N_2O) as the oxygen source. The chemical reaction is:

$$SiH_4 + 2N_2O \rightarrow SiO_2 + 2N_2 + 2H_2 \qquad 2.7$$

Oxygen has a much greater affinity to react with the silane then with the nitrogen. That is why the silicon dioxide formation dominates over silicon nitride formation. The silicon dioxide and silicon nitride are often deposited in one and the same chamber without major changes in the operating parameters.

2.2. Theory of VCSELs and basics of organic materials

The quarter-wave stack is used as a basic building block for many types of thin-film filters. It can be used as a longwave-pass filter, a shortwave-pass filter, a bandstop filter, a high-reflectance coating, for example in laser mirrors, and as a reflector in a thin-film Fabry-Perot interferometer [76; 77; 78]. It is possible to couple two or more Fabry-Perot filters in series to give a more rectangular pass band. For the great majority of cases the thin films are completely transparent, so that no energy is absorbed.

2.2.1. The light as electromagnetic wave

Electromagnetic waves (EM) were first predicted by James Clerk Maxwell and subsequently confirmed by Heinrich Hertz. Maxwell derived a wave form of the electric and magnetic equations, revealing the wave-like nature of electric field (in SI system - volts per meter [V/m]) and magnetic fields (in SI system - tesla [T]), and their symmetry. Because the speed of EM waves predicted by the wave equation coincided with the measured speed of the light, Maxwell concluded that light itself is an EM wave. According to Maxwell's equations, a time-varying electric field generates a magnetic field and vice versa. Therefore, as an oscillating electric field generates an oscillating magnetic field, the magnetic field in turn generates an oscillating electric field. These oscillating fields together form an electromagnetic wave. The Maxwell's equations describe the interrelationship between electric field, magnetic field, electric charge, electric current, and their space and time derivatives.

In practice there are many types of possible electromagnetic waves. All these possible electromagnetic waves must obey a special wave equation that describes the time and space dependence of the electric magnetic field. In an isotropic and linear dielectric medium, the relative permittivity (ε_r) is the same in all directions and that it is independent of the electric field. The field E must obey Maxwell's EM wave equations:

$$\frac{\partial^2 E}{\partial x^2} + \frac{\partial^2 E}{\partial y^2} + \frac{\partial^2 E}{\partial z^2} = \varepsilon_0 \varepsilon_r \mu_0 \frac{\partial^2 E}{\partial t^2} \qquad 2.8$$

in which μ_o is the absolute permeability, ε_0 is the absolute permittivity and ε_r is the relative permittivity of the medium.

Light is an electromagnetic wave with time varying electrical and magnetic fields, that is E_x and B_y respectively, which are propagating through space in such a way that they are always perpendicular to each other and z is the direction of propagation (see Fig. 2-9).

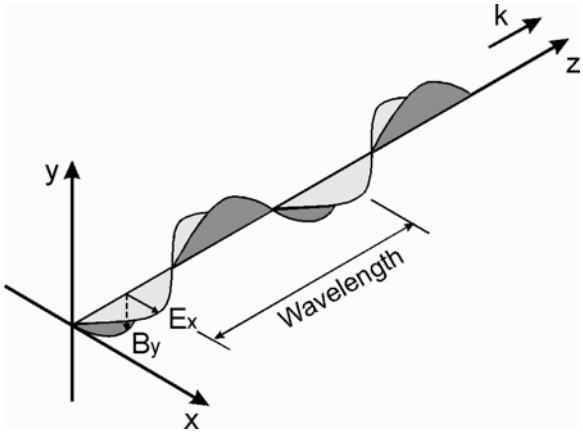

Fig. 2-9. An electromagnetic wave is a traveling wave which has time varying electric and magnetic fields which are perpendicular to each other and the direction of propagation, z.

The simplest traveling wave is a sinusoidal wave that, for propagation along z, has the general mathematical form [79]:

$$E_x = E_0 \cos(\omega t - kz + \phi_0) \qquad 2.9$$

where E_x is the electrical field at position z at time t, k is the propagation constant, ω is the angular frequency, E_0 is the amplitude of the wave and ϕ_0 is the phase constant. Equation 2.9 describes a monochromatic plane wave of infinite extent traveling in the positive z direction. A surface over which the phase of the wave is constant is referred to as a wavefront.

The traveling wave can also be represented by wave vector **k**:

$$E(\mathbf{r},t) = E_0 \cos(\omega t - \mathbf{k} \cdot \mathbf{r} + \phi_0) \qquad 2.10$$

When an EM wave is traveling in a dielectric medium, the oscillating electric field polarizes the molecules of the medium at the frequency of the wave. The net effect is that the polarization mechanism delays the propagation of the wave. The velocity *v* in nonmagnetic dielectric medium is given by:

$$v = \frac{1}{\sqrt{\varepsilon_r \varepsilon_0 \mu_0}} \qquad 2.11$$

The ratio of the speed of light in free space to its speed in a medium is called complex refractive index *N* of the medium:

$$N = \frac{c}{v} = \sqrt{\varepsilon_r} = n - ik \qquad 2.12$$

In equation 2.12 *n* is known as the real part of the refractive index and *k* is known as the extinction coefficient.

2.2.2. Distributed Bragg reflector

The distributed Bragg reflector (DBR) is a multilayer structure with alternating high (n_H) and low (n_L) refractive index thin-films (see Fig. 2-10). Many optical devices relay on the high reflectivity of the DBR structure. The materials used for fabrication of such a mirror are with very low or zero absorption.

The periodic multilayer stack has to obey the Bragg condition:

$$\Lambda = \frac{1}{2}\frac{m}{2}\frac{\lambda_d}{n} \qquad 2.13$$

where Λ is the grating period, λ_d is the wavelength in vacuum, *n* the effective refractive index of the alternating materials and *m* the Bragg order. Constructive interference occurs when *m* takes odd integer values (*m* = 1, 3, 5, ...).

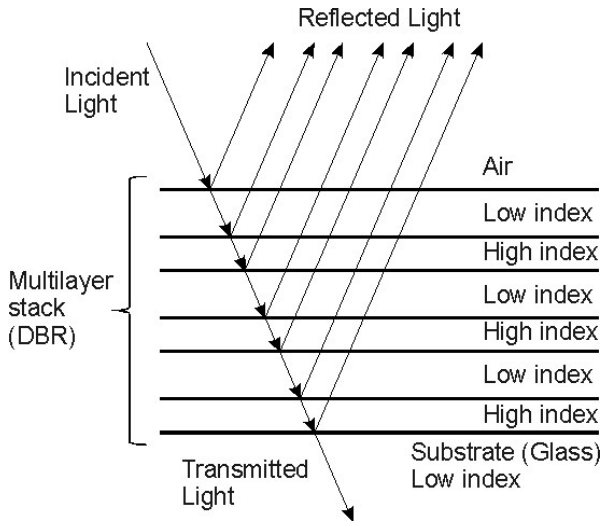

Fig. 2-10. A multilayer structure with alternating low and high refractive index materials. Schematic of a selection of ray traces. The incident light is divided on reflected and transmitted light. (The multiple reflection paths in the DBR mirrors are not shown; the refraction effects are not shown)

The light reflected at the interface between the high and low refractive index layers shows no phase shift on reflection, while that reflected light on the low and high refractive index interface shows a phase change of π. The various components of the incident light produced by the successive reflection at the boundaries throughout the structure will reappear at the front surface all in phase so that they will recombine constructively. So the desired reflectivity of the mirror can be achieved by increasing the number of the layers. It is found that the reflectance remains high over only a limited range of wavelengths, depending on the ratio of high and low refractive indices. Outside of the stop-band, so called fringes are observed with relatively low reflectivity.

For an accurate evaluation of the optical properties of the DBR mirror and the filter, the multiple reflections in the layers must be taken into account. This involves extremely complex calculations. More effective approach has been found in the development of entirely new methods to find solutions of Maxwell's equations. The solution is the product of 2 x 2 matrices, where each matrix represents a single film. This method is so called transmission or transfer matrix method. The method considers the electric (*E*) and magnetic (*H*) fields of a transverse electromagnetic wave propagating in a layer.

The DBR usually consist of a number of boundaries between various homogeneous media. The effect which these boundaries have on an incident

wave should be taken in account. At this boundary region the tangential components of *E* and *H*, that is, the components along the boundary, are continuous across it. The presence of two or more interfaces means that a number of beams will be produced by successive interference of the reflected and transmitted wave.

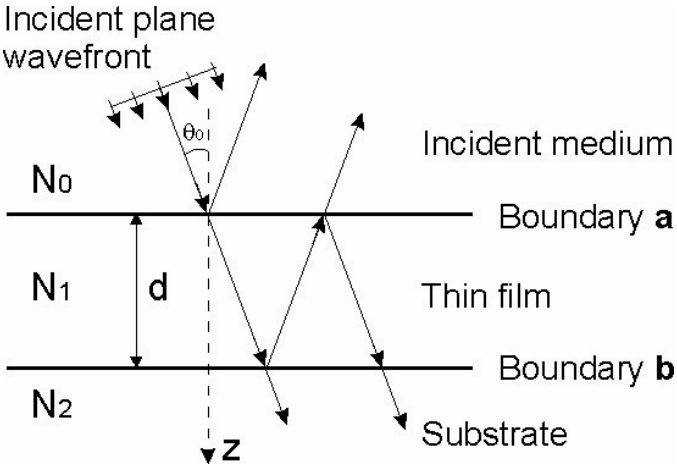

Fig. 2-11. Incident plane wave on a single thin-film and its multiple reflection and transmission at the boundary **a** and **b**.

By using the Maxwell´s equations, the following transmission matrix for a single thin-film (see Fig. 2-11) can be found [80]:

$$\begin{bmatrix} E_a \\ H_a \end{bmatrix} = \begin{bmatrix} cos\delta & (\mathrm{i}\, sin\delta)/\eta_1 \\ \mathrm{i}\, \eta_1 sin\delta & cos\delta \end{bmatrix} \begin{bmatrix} E_b \\ H_b \end{bmatrix} \qquad 2.14$$

where

E_a	tangential component of the electric field at the boundary *a*
E_b	tangential component of the electric field at the boundary *b*
H_a	tangential component of the magnetic field at the boundary *a*
H_b	tangential component of the magnetic field at the boundary *b*
η	the tilted optical admittance

Since the tangential components of *E* and *H* are continuous across a boundary and there is only positive going wave in the substrate, the equation 2.14 shows the relationship between the tangential components of *E* and *H* at the incident interface and the tangential components of *E* and *H* which are transmitted

through the final interface. The 2 x 2 matrix on the right-hand side is known as the characteristic matrix of the thin film.

The equation 2.14 can be normalized by dividing by E_b to give the coefficients *B* and *C*. These coefficients represent the normalized electric and magnetic fields at the front interface. From them the properties of the thin-film system can be extracted.

The reflectance of an assembly of *q* layers is calculated by the concept of optical admittance. The characteristic matrix is simply the product of the individual matrices taken in the correct order:

$$\begin{bmatrix} B \\ C \end{bmatrix} = \left\{ \prod_{r=1}^{q} \begin{bmatrix} cos\delta_r & (\mathrm{i}\, sin\delta_r)/\eta_r \\ \mathrm{i}\, \eta_r sin\delta_r & cos\delta_r \end{bmatrix} \right\} \begin{bmatrix} 1 \\ \eta_m \end{bmatrix} \quad 2.15$$

where

B	normalized electric field
C	normalized magnetic field
q	number of layers
η_m	substrate admittance

The order of multiplication of the matrix is, if *q* is the layer next to the substrate:

$$\begin{bmatrix} B \\ C \end{bmatrix} = [M_1][M_2] \ldots [M_q] \begin{bmatrix} 1 \\ \eta_m \end{bmatrix} \quad 2.16$$

Using the normalized electric and magnetic fields (*B* and *C*) the reflectance, transmittance and absorption can be calculated:

$$R = \left(\frac{\eta_0 B - C}{\eta_0 B + C}\right)\left(\frac{\eta_0 B - C}{\eta_0 B + C}\right)^* \quad 2.17$$

$$T = \frac{4\eta_0 Re(\eta_m)}{(\eta_0 B + C)(\eta_0 B + C)^*} \quad 2.18$$

$$A = \frac{4\eta_0 Re(BC^* - \eta_m)}{(\eta_0 B + C)(\eta_0 B + C)^*} \quad 2.19$$

Phase shift on reflection, measured at the front surface of the multilayer, is given by:

$$\varphi = arctan\left(\frac{Im[\eta_m(BC^* - CB^*)]}{(\eta_m^2 BB^* - CC^*)}\right) \quad 2.20$$

$$\zeta = \arctan\left[\frac{-Im(\eta_0 B + C)}{Re(\eta_0 B + C)}\right] \quad 2.21$$

The transfer matrix method is a very simple and accurate method. Calculation by hand of the properties of the given multilayer, particularly if there are absorbing layers present and a wide spectral range is involved, is an extremely tedious and time-consuming task. The preferred method of calculation is to use a computer. In Fig. 2-12 the reflectivity of 15 periods SiO2/ZrO2 DBR mirror simulated by the transfer matrix method is shown.

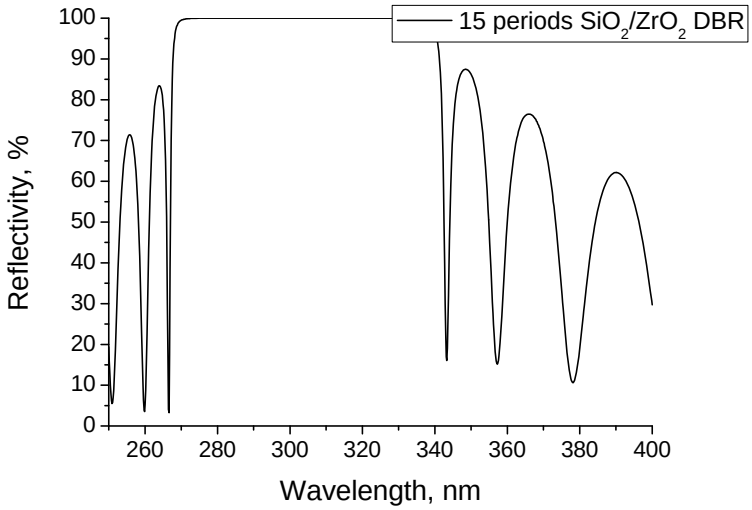

Fig. 2-12. Reflectivity of 15 periods SiO_2/ZrO_2 DBR mirror calculated by transfer matrix method.

2.2.3. Optical Fabry-Perot filters

The optical filter is a multilayer structure and consists of DBR mirrors and Fabry-Perot optical resonator [81]. The Fabry-Perot resonator has two mirrors M_1 and M_2 separated by a distance d_s aligned so that they are parallel to a very high degree of accuracy. The schematic diagram of the resonator or so called etalon is shown in Fig. 2-13a. This structure leads to constructive and destructive

interference of the light reflected from the mirrors M_1 and M_2. The distance between the two mirrors is called cavity. The result is a series of allowed standing electromagnetic waves in the cavity called cavity modes (see Fig. 2-13b).

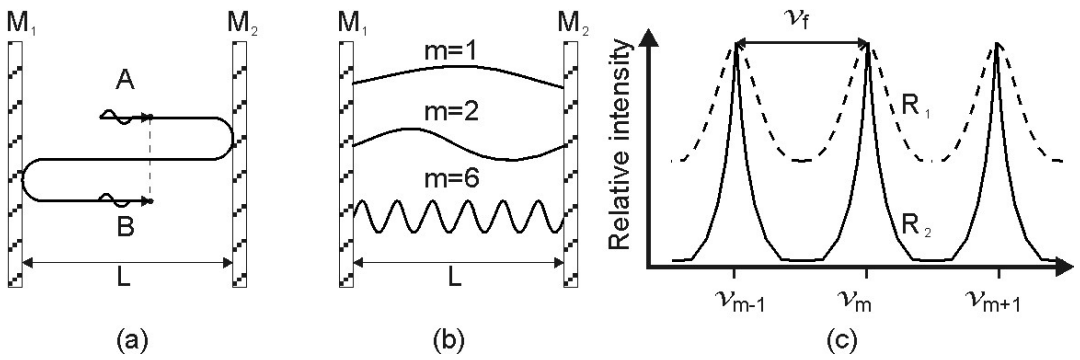

Fig. 2-13. Schematic illustration of the Fabry-Perot optical cavity and its properties. (a) Reflected waves interface. (b) Only standing EM waves of certain wavelengths are allowed in the cavity. (c) Intensity vs. frequency for various modes. R is mirror reflectance and lower R means higher loss from the cavity.

Each EM wave allowed in the resonator is defined as cavity mode, and the cavity length should satisfy the following equation:

$$L = m\left(\frac{\lambda}{2}\right), \quad m = 1, 2, 3 \ldots \qquad 2.22$$

The corresponding frequencies ν_m of the allowed modes is known as resonant frequencies of the cavity:

$$\nu_m = m\left(\frac{c}{2L}\right) = m\nu_f \qquad 2.23$$

with

$$\nu_f = \frac{c}{(2L)} \qquad 2.24$$

where ν_f is the free spectral range. It shows the lowest frequency corresponding to m = 1, the fundamental mode, and the frequency separation of two neighboring modes. If the mirrors are perfectly reflecting and there is no absorption in the cavity the peaks at frequencies ν_m defined by equation 2.23 are thin and sharp lines. If the mirrors are not perfect and some radiation escapes

from the cavity, then the peaks are not sharp enough and the lines are thicker Fig. 2-13c.

After one round trip between the mirrors the traveling wave will be reflected but with different phase and magnitude due to the refractive index difference and non-perfect reflections. If we assume that the first wave is A and the second B then A and B will interfere and the result will be:

$$A + B = A + Ar^2 \exp(-j2kL) \quad 2.25$$

The wave B has one round-trip phase difference of *k(2L)* and a magnitude r^2 with respect to A. After infinite round-trip reflections and corresponding interferences the cavity intensity I_{cavity} is given by the following formula:

$$I_{cavity} = \frac{I_0}{(1-R)^2 + 4Rsin^2(kL)} \quad 2.26$$

A smaller mirror reflectance *R* means more radiation loss from the cavity, which affects the intensity distribution in the cavity. From equation 2.26 can be seen that smaller *R* values result in broader mode peaks and a smaller difference between the minimum and maximum intensity in the cavity. This can be seen in Fig. 2-13c. The spectral width $\delta\nu_m$ of the Fabry-Perot etalon is the full width at the half maximum (FWHM) of an individual mode intensity. The spectral width is represented by the following equation:

$$\delta\upsilon_m = \frac{\upsilon_f}{F} \quad 2.27$$

where *F* is called the finesse of the resonator, which increases as losses decreases. Large finesses lead to sharper mode peaks. It can be calculated by the equation:

$$F = \frac{\pi R^{1/2}}{1-R} \quad 2.28$$

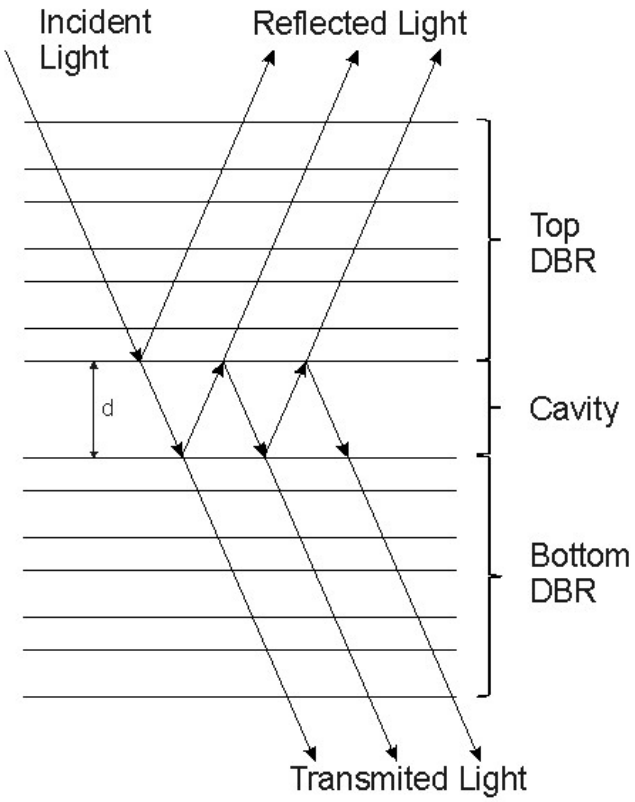

Fig. 2-14. Structure of the Fabry-Perot interference filter with top and bottom DBR, as well as cavity. Schematic of a selection of ray traces. A part of the incident light is reflected and the other part is transmitted. In the cavity only the allowed modes are existing. (The multiple reflection paths in the DBR mirrors are not shown; the refraction effects are not shown)

The combination of the Fabry-Perot optical cavities and the high reflective DBR structures are widely used in laser, interference filters, and spectroscopic applications. The Fabry-Perot interference filter consists of two DBR multilayer structures and a cavity space between them (see Fig. 2-14). By combination of the high reflectivity of the DBR structure and the filtering mode of the Fabry-Perot etalon a wave with very thin FWHM can be transmitted.

To cover the requirements of the constrictive interference, in case that the multilayer stack contacts with the air the filter should finish with high refractive index material. Depending on the spacer there are only two cases which need to be considered. If *x* is the number of high-index layers in each stack, not counting

the cavity (spacer) layer, then in case of the high-index spacer, the transmission of the stack is given by:

$$T = \frac{4n_L^{2x} \cdot n_s}{n_H^{2x+1}} \quad 2.29$$

and in the case of the low-index spacer by:

$$T = \frac{4n_L^{2x-1} \cdot n_s}{n_H^{2x}} \quad 2.30$$

The parameters of the Fabry-Perot filter vary with variation in the angle of the incident light. This variation can be used in the production to tune the filter in any device for the desired wavelength in an acceptable tolerance.

The phase thickness of a thin film at oblique incidence is:

$$\delta = 2\pi nd.\cos\theta/\lambda \quad 2.31$$

which can be thought as an apparent optical thickness of $ndcos\theta$ which varies with angle of incidence so that the layers seem thinner when tilted. This change in the thickness moves the filter pass band to shorter wavelength.

2.2.4. Light emitting organic semiconductor materials

The organic semiconductor materials used in optical devices can be classified into three categories according to their structure [22]:

- chelate metal complexes
- conjugated polymers
- organic dyes (without metal atoms)

Examples of chemical structure of some common organic materials are shown in Fig. 2-15. The organic material Spiro-Octopus-1 is an example for material with new structural concept based on the spiro-linkage of identical molecular entities [82; 83]. The chelate metal complex Alq_3 is a relatively small molecule with limited extension of the conjugated system [20]. In contrast to the chelate metals complexes the conjugated polymers consist of many identical (conjugated) repeated units [84], called monomers. Dyes are aromatic organic compounds

which are based fundamentally on the structure of benzene [85; 86]. Dyes, either as solutions or vapors, are the active material in pulsed and CW dye lasers. They emit in comparatively narrow spectral range. It is typically 30 nm and to cover bigger spectral range a variety of dyes is necessary to be used [85].

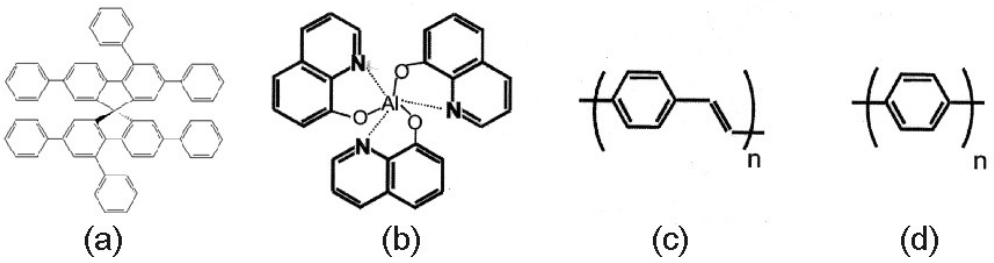

Fig. 2-15. Chemical structure formula of several organic semiconductors [20]: (a) Spiro-Octupos-1, (b) Alq_3, (c) Poly(p-phenylenevylene), PPV, (d) Poly(p-phenylene), PPP.

The benzene ring shown in Fig. 2-16 is the base component of the organic materials. Each carbon atoms provides four valence electrons, three of whom form so called σ-bonds with neighboring carbon or hydrogen atoms. In this way the steric geometry is defined. The remaining 6 valence electrons of the 6 carbon atoms occupy p_z orbitals, which are aligned perpendicular to the plane of the σ-bonds. The p_z electrons from two neighboring carbons form an additional π-bonds, so that the benzene ring consists of several alternating single and double bonds.

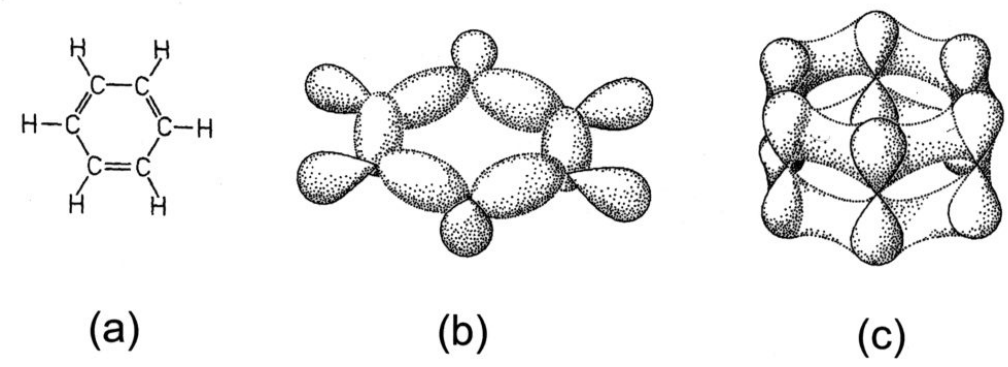

Fig. 2-16. C_6H_6 (benzene): (a) chemical structure formula, (b) spatial distribution of the σ-orbitals which are responsible for the steric configuration, (c) spatial distribution of the π-orbitals forming a delocalized π-system.

Whenever an electronic transition occurs in a molecule the nuclei are subject to a change in Coulombic force as a result of the redistribution of electronic charge that accompanies the transition [87]. As a consequence, electronic transitions are strongly coupled to the vibrational modes of the molecule. In the absorption (fluorescence) spectrum these vibronic transitions cause characteristic side-bands above (below) the purely electronic transitions.

A σ orbital can be formed either from two s atomic orbitals, or from one s and one p atomic orbital, or from two p atomic orbitals having a collinear axis of symmetry. The bond formed in this way is called a σ bond. A π orbital is formed from two p atomic orbitals overlapping laterally. The resulting bond is called a π bond. Absorption of a photon of appropriate energy can promote one of the π electrons to an antibonding orbital denoted by π*. The transition is then called π → π*. The promotion of a σ electron requires a much higher energy (absorption in the far UV). A molecule may also possess non-bonding electrons located on heteroatoms such as oxygen or nitrogen. The corresponding molecular orbitals are called n orbitals. Promotion of a non-bonding electron to an antibonding orbital is possible and the associated transition is denoted by n → π*. To illustrate this in Fig. 2-17 is shown the energy levels of formaldehyde as an example, with all the possible transitions.

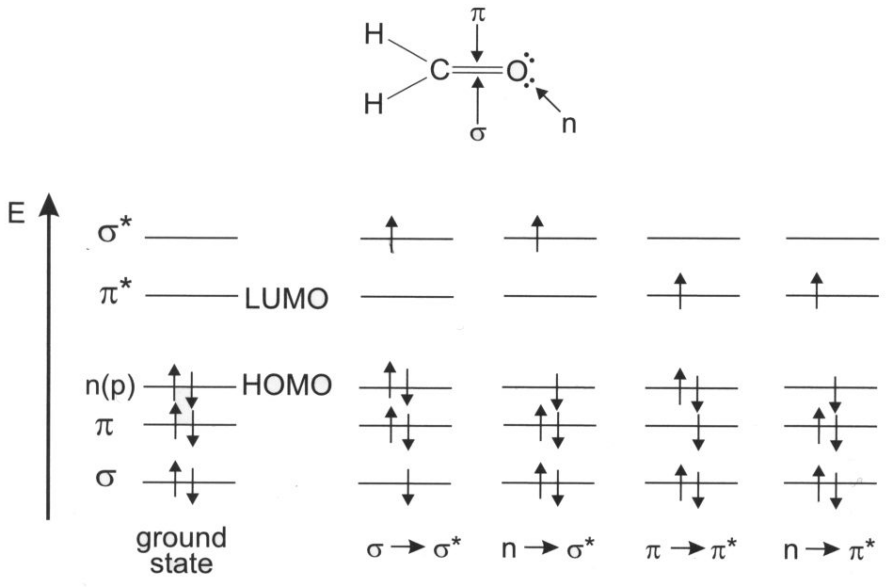

Fig. 2-17. Example of energy levels of molecular orbitals in formaldehyde and possible electronic transitions.

In absorption and fluorescence spectroscopy, two important types of orbitals are considered: the Highest Occupied Molecular Orbitals (HOMO) and the Lowest Unoccupied Molecular Orbitals (LUMO). Both of these refer to the ground state of the molecule. For example in formaldehyde the HOMO is the n orbital and the LUMO is the π^* orbital (see Fig. 2-17).

When one of the two electrons of opposite spins is promoted to a molecular orbital of higher energy, its spin is in principle unchanged so that the total spin quantum number remains equal to zero. Because the multiplicity of both the ground and excited states is equal to 1, both are called singlet state. The corresponding transition is called singlet-singlet transition.

Fig. 2-18 shows the molecular potential energy as a function of a generalized nuclear coordinate R for the ground state S_0 and an electronically excited singlet state S_1. The respective vibronic states are denoted by ν and ν'. Since the energy associated with a vibronic excitation is usually much higher than the thermal energy at room temperature, a molecule in thermal equilibrium occupies the state S_0 with ν=0.

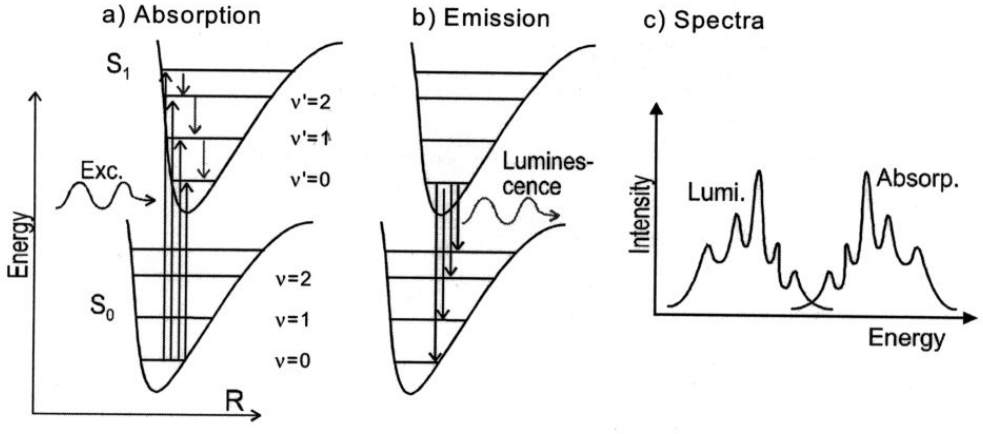

Fig. 2-18. Molecular potential energy as a function of the atomic distance. Vibronic eigenstates are denoted by ν and ν'. The arrows indicate vibronic transitions associated with (a) absorption and (b) emission of a photon. The corresponding absorption and luminescence spectra are shown in (c).

Absorption of a photon of suitable energy causes a transition $S_0,\nu \rightarrow S_1,\nu'$. It is followed by a cascade of radiative and radiationless transitions. The most important transitions are summarized in Fig. 2-19. Following an excitation into a vibronically excited state S_1 a molecule quickly relaxes to the vibronic ground state $\nu'=0$ by internal conversion. In a radiative transition the molecule returns to S_0,ν accompanied by spontaneous (or stimulated) emission of a photon. The resulting absorption and fluorescence spectra are sketched in Fig. 2-18c. In solid state samples the vibronic structure can often not be resolved due to homogeneous and inhomogeneous broadening of the transitions. The apparent Stokes-shift between the absorption and emission maxima of the purely electronic transition is cause by intermolecular structural relaxation and intermolecular energetic dissipation.

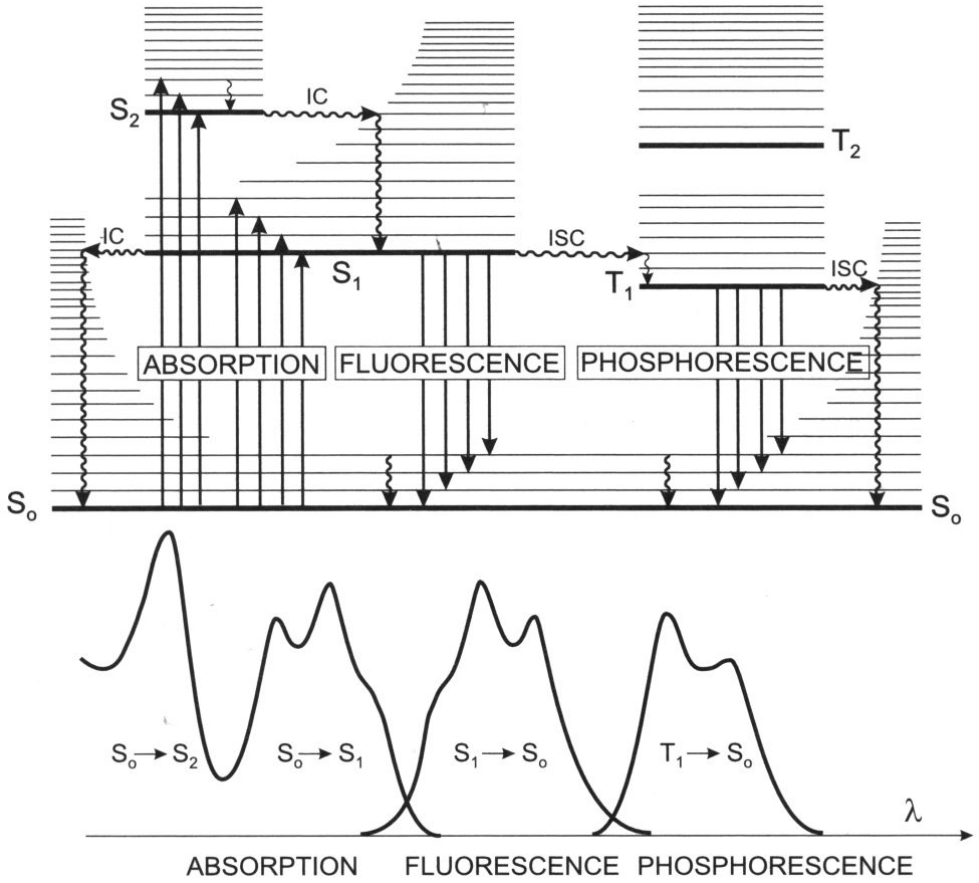

Fig. 2-19. Perrin-Jablonski diagram and illustration of the relative positions of absorption, fluorescence and phosphorescence spectrum.

The molecules of the solid state materials can be arranged in a crystalline, polycrystalline or in amorphous structure. Similarly to the inorganic

semiconductors, the organic semiconductor materials have well defined valence and conduction bands with large charge mobility. The transport of the electrons is done by tunneling from molecule to molecule. All organic semiconductors have weak dielectric constant, which comes from the small intermolecular coupling.

The optical properties of the polycrystalline materials are reduced because of the boundaries of the grain structure. For fabrication of organic photoluminescence devices single crystal or glass materials are used. Since the glass structure is easier to be produced the interest is focused on the glassy materials [19].

2.2.5. Light Amplification by Stimulated Emission of Radiation (LASER)

The various laser types developed so far possess wide range of physical and operating parameters. Concerning the physical state of the laser active material the lasers are divided in solid-state, liquid, or gas lasers. A rather special case is the free-electron laser where the active material consists of free electrons at relativistic velocities passing through a spatially periodic magnetic field. This magnetic field forces the electrons in the beam to assume a sinusoidal path. The acceleration of the electrons along this path results in the release of a photon. The free electron laser has the widest frequency range of any laser type, and can be widely tunable, currently ranging in wavelength from microwaves, through terahertz radiation and infrared, to the visible spectrum, to ultraviolet, to soft X-rays. Output powers cover very big range of values. For continuous wave lasers the power range is typically from a few mW, for optical communications or bar code scanners, to tens of kW, for lasers used for material modification. The peak power by pulsed lasers can reach values at about 1PW. The pulse duration can vary widely from the ms for lasers operating in free-running regime to about 10 fs for some mode-locked lasers. The lasers can be characterized concerning the wavelength of the emitted radiation as infrared, visible, ultraviolet and x-ray lasers. The corresponding wavelength can vary from 1 mm to 1 nm. The physical dimensions are very different. The cavity can be from several nanometers for the shortest laser to some kilometers for the longest laser.

This variety of parameters gives enormous potential the laser to be used for different commercial and scientific applications. On the other hand, this huge amount of possible devices and systems gives a problem by mass production and reduction of the price respectively.

2.2.5.1. Principles of the spontaneous and stimulated emission, and absorption

To describe the phenomenon of the spontaneous and stimulated emission and absorption, two energy levels E_1 and E_2 (where $E_1 < E_2$) of some atom or molecule of a given material are considered. If the atom is initially at level 2, it tends to decay to level 1 (see Fig. 2-20b). The corresponding energy difference $E_2 – E_1$ must therefore be released by the atom. When this energy is delivered in the form of an electromagnetic wave, the process is called spontaneous emission. It is characterized by the emission of a photon with energy:

$$h\nu_0 = E_2 - E_1 \qquad 2.32$$

where

h	Planck's constant
ν_0	frequency of the radiated wave
E_1	energy of the atom at the energy level 1 ($E_1 < E_2$)
E_2	energy of the atom at the energy level 2 ($E_1 < E_2$)

In case the energy difference $E_2 – E_1$ is delivered in some other form of energy then electromagnetic radiation, the phenomenon is called nonradiative decay. The energy may be converted into the kinetic or internal energy of the surrounding atoms or molecules.

The stimulated emission is described by forced transition of the electron from energy level 2 to energy level 1 caused by incident electromagnetic wave on the material (see Fig. 2-20c). The emitted wave has the same frequency as the atomic frequency and the energy difference $E_2 – E_1$ is delivered in the form of an electromagnetic wave that adds to the incident wave. In this case the emission superpose in phase to the incoming wave and in the same direction.

If the electron occupies the ground level 1, it remains in this level unless some external energy is applied. Such energy can be in form of incident electromagnetic wave on the material with frequency $\nu = \nu_0$. In this case there is a finite probability that the atom will be raised to level 2 (see Fig. 2-20a). The energy difference $E_2 – E_1$ required by the atom to do the transition is obtained from the energy of the incident electromagnetic wave. This phenomenon is called absorption.

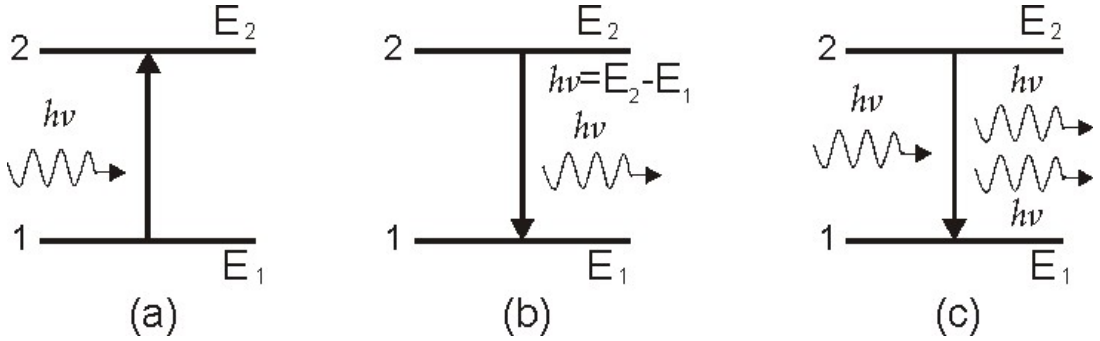

Fig. 2-20. Schematic illustration of the three processes: (a) absorption, (b) spontaneous emission, (c) stimulated emission,

To describe the probability for the emission and absorption phenomenon the quantity population of the level (N_i) is used. N_i is the number of the atoms (or molecules) per unit volume that at time t occupy a given energy level i. The following equation shows the probability that the stimulated process occurs:

$$\left(\frac{dN_2}{dt}\right)_{st} = -W_{21}N_2 \qquad 2.33$$

where $(dN_2/dt)_{st}$ is the rate at which the transition 2 → 1 occur as a result of stimulated emission and W_{21} is the rate of stimulated emission.

2.2.5.2. The principle of the LASER

If a plane wave with a photon flux F is traveling in the z-direction in material with population N_1 and N_2 at the energy levels 1 and 2 respectively, absorption and emission processes can occur. This leads to elemental change dF of this flux along the elemental length dz of the material. In Fig. 2-21 the elemental change dF in the photon flux F for a plane electromagnetic wave in traveling a distance dz through the active material is shown. The change in number between outgoing and incoming photons in the shaded volume S per unit time is represented by SdF, where S is the cross-sectional area of the beam. Since each stimulated process creates a photon and each absorption removes a photon, the difference between stimulated emission and absorption events occurring in the shaded volume per unit time must be equal.

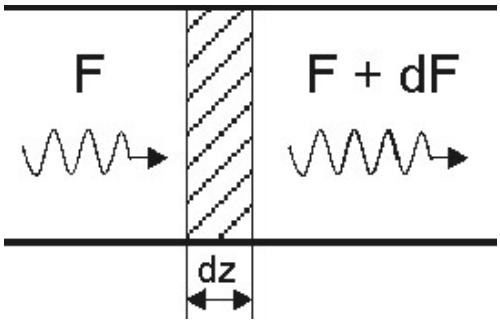

Fig. 2-21. Elemental change *dF* in the photon flux *F* for a plane electromagnetic wave in traveling a distance *dz* through the active material.

The elemental change of the photon flux *dF* is represented by the following equation:

$$dF = \sigma_{21} F \left[N_2 - \left(\frac{g_2 N_1}{g_1} \right) \right] dz \qquad 2.34$$

In this equation the radiative and nonradiative decays are not considered, because of their negligible contribution to the incoming photon flux. The material behaves as an amplifier if $dF/dz > 0$ (see Eq. 2.34) or $N_2 > g_2 N_1 / g_1$ respectively, while it behaves as an absorber if $N_2 < g_2 N_1 / g_1$.

To describe the thermal equilibrium populations a Boltzmann statistics is used and shown by the following equation:

$$\frac{N_2^e}{N_1^e} = \frac{g_2}{g_1} exp - \left(\frac{E_2 - E_1}{kT} \right) \qquad 2.35$$

where

k	Boltzmann's constant
T	absolute temperature of the material
N_1^e	thermal equilibrium population at level 1
N_2^e	thermal equilibrium population at level 2
E_1	energy of the atom at the energy level 1 ($E_1 < E_2$)
E_2	energy of the atom at the energy level 2 ($E_1 < E_2$)

In ordinary conditions the material reacts as an absorber at frequency ν_0 and stays under thermal equilibrium ($N_2^e < g_2 N_1^e / g_1$). In case of population inversion a

nonequilibrium conditions are achieved and the material reacts as an amplifier. The material in which this population inversion is produced is referred to as an active material.

If the transition frequency $v_0 = (E_2 - E_1)/kT$ is in the microwave region, the type of the amplifier is called maser amplifier and if it is in the optical region – is called laser amplifier.

In a real situation an atom is surrounded by many other atoms having different energy levels. Some atoms are at a ground state and other are at an excited state. In one optical dense medium the decay from excited to ground state is due to the simultaneously phenomenon of the spontaneous and stimulated transitions. In a medium with low level of excited atoms the radiation trapping can play a significant role. In this case a photon instead of escaping the medium can be absorbed by another atom and put this atom in excited state. The lifetime of this photon depends on the atomic density and the geometry of the material.

The phenomenon of amplified spontaneous emission (ASE) can be observed in optically dense medium with high ratio of excited atoms. The amplified spontaneous emission shows some similarity to the laser processes. For example it has some degree of directionality; the bandwidth is relatively narrow compared to this of the spontaneous emission; the ASE shows a soft threshold behavior with very intense light of the beam.

In Fig. 2-22 the solid angle of emission Ω in the case of amplified spontaneous emission is shown. If the gain of the active material $G = \exp \sigma (N_2 - N_1)/l$ is large enough, the fluorescence power preferentially emitted into the solid angle Ω can be strongly amplified by the active medium. If the structure is so designed that D << l then the emission solid angle Ω is given by the following equation:

$$\Omega = \frac{\pi D^2}{4l^2} \qquad 2.36$$

where

D	diameter of the active material
l	length of the active material

In the case of high reflective mirror on one side of the structure (see Fig. 2-22b):

$$\Omega = \frac{\pi D^2}{16 l^2} \qquad 2.37$$

the emission solid angle is even smaller and results in narrow and more concentrated outgoing beam. If the wave starts from point O (see Fig. 2-22b) then reflects from the mirror on the other end of the structure and goes out under smaller angle than those in Fig. 2-22a.

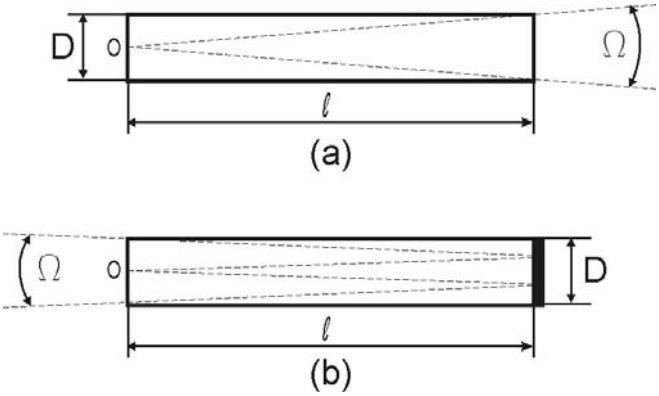

Fig. 2-22. Solid angle of emission Ω in the case of amplified spontaneous emission: (a) structure without high reflective end mirror, (b) structure with high reflective end mirror

At the first case shown on the Fig. 2-22a the emitted radiation can exit the active medium in both directions. If a totally reflecting mirror is placed at the one end of the structure the emission is redirected and forced to exit the material only from the other side (see Fig. 2-22b). This configuration combined with the amplified spontaneous emission is usually used to obtain directional and narrow bandwidth radiation of high intensity. Examples are high-gain mediums like nitrogen excimer or plasma for X-Ray. Since either one mirror only or no mirror at all is required, the system is called mirrorless lasers. Similarly to the laser, the ASE emission has some spatial and temporal coherence but consists of amplified spontaneous-emission noise only.

To make an oscillator from the amplifier and to achieve positive amplification at the resonance frequency v_0 a suitable positive feedback is necessary. Such a feedback is achieved by placing the active material between two highly reflective

mirrors as it is shown in Fig. 2-23. At each passage through the active material the plane electromagnetic wave is amplified. If one of the two mirrors is partially transparent, a useful output beam is obtained from that mirror. It is obvious that the outgoing useful beam is a loss for the light amplification in the laser structure.

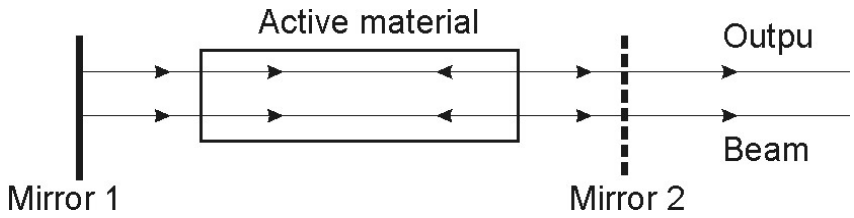

Fig. 2-23. Scheme of a laser. The active material is placed between the two high reflective mirrors, where the Mirror 2 is partially transparent. The feedback of the electromagnetic wave is responsible for the amplification of the light.

To achieve a lasing phenomenon some important threshold conditions must be achieved. In the laser case, oscillation begins when the gain of the active material compensate the losses in the laser. Such losses are for example due to output coupling. At the threshold the photon flux *F'* after one roundtrip must be equal to the photon flux *F* at the beginning. The threshold is reached when the population inversion reaches a critical value, called critical inversion. The critical inversion is given by the following equation:

$$N_c = -\frac{\ln R_1 R_2 + 2\ln(1 - L_i)}{2\sigma l} \qquad 2.38$$

where

R_1	power reflectivity of the mirror 1
R_2	power reflectivity of the mirror 2
l	length of the active material
L_i	internal loss per pass in the laser cavity

Once the critical inversion is reached, the spontaneous emission is the outgoing point for the oscillation. Photons spontaneously emitted along the cavity axis in fact initiate the amplification process.

Several pumping schemes are available which can describe the population inversion in a given material. In Fig. 2-24 are shown two different types of laser

schemes, namely three-level (see Fig. 2-24a) and four-level (see Fig. 2-24b) schemes. The population inversion is only to be achieved be using materials with multilevel laser schemes.

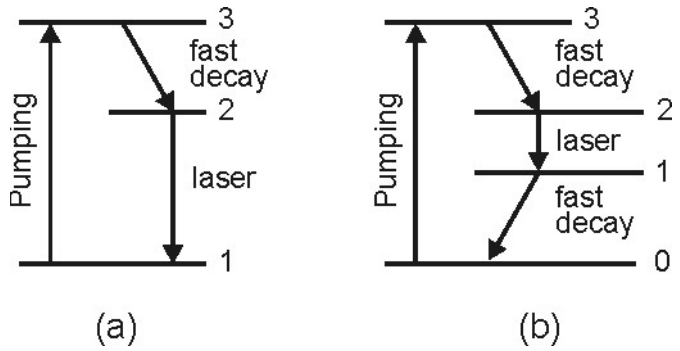

Fig. 2-24. Laser schemes of pumping: (a) three-level and (b) four-level.

Nowadays the so-called quasi-three-level lasers have also become a very important laser category. In this case the ground level consists of many sublevels, where the lower laser level is one of these sublevels.

The process in which the atoms are raised from level 1 to level 3 in case of three-level-schemes, or from the ground level to level 3 in case of quasi-three-level lasers is known as pumping. There are several ways in practice how this process can be accomplished. The most important ways are by an electrical discharge in the active material or by some sort of eradiation with sufficient intensity. The first one is known as electrical pumping and the second one as optical pumping.

The unique properties of the laser are used in various applications. The laser radiation is characterized by an extremely high degree of monochromaticity, coherence, directionality, and brightness. Very interesting are lasers with short duration capable of to producing short light pulses.

The monochromaticity is influenced by the range of frequencies which can be amplified and by the allowed frequency in the resonant cavity. The coherence can be divided in spatial and temporal coherence. The spatial coherence concerns the phase correlation of the electrical field at two difference point at time t=0, and the temporal coherence concerns the phase correlation between the electrical field at a given point P at time t and time t + τ. The directionality concerns the divergence of a plane electromagnetic wave due to the diffraction. In case of perfect spatial

coherence the divergence is obtained from the diffraction theory and obeys the following equation:

$$\theta_d = \frac{\beta\lambda}{D} \qquad 2.39$$

where

λ	wavelength
β	numerical coefficient
D	the diameter of the beam

In case of partial spatial coherence the divergence is grater by the minimum value set by diffraction. The brightness of electromagnetic wave of given source is defined by the power emitted per unit surface area per unit solid angle.

2.2.5.3. Vertical-Cavity Surface-Emitting Lasers (VCSEL) and Distributed Feedback Lasers (DFB)

The Vertical-Cavity Surface-Emitting Lasers (VCSEL) and Distributed Feedback Lasers (DFB) [88; 89] represent one of the most important classes of lasers in use today. They are involved in large variety of applications.

The vertical-cavity surface-emitting laser is a type of laser diode with laser beam emission perpendicular from the top surface, contrary to conventional edge-emitting lasers which emit from surfaces formed by cleaving the individual chip out of a wafer.

The VCSEL resonator consists of two distributed Bragg reflector (DBR) mirrors (see 2.2.2.) parallel to the wafer surface with an active region for the laser light generation in between. The planar DBR-mirrors consist of layers with alternating high and low refractive indices. Each layer has a thickness of a quarter of the laser wavelength in the material, yielding reflectivity above 99%. High reflectivity mirrors are required in VCSELs to balance the short axial length of the gain region. The cavity length of VCSELs is very short typically 1-2 wavelengths of the emitted light. As a result, in a single pass of the cavity, the photons have a small chance of trapping. This conventional structure is so called index coupled VCSEL. In Fig. 2-25a the index coupled laser structure with distribution of the

electrical field and the refractive index profile is shown. In this structure the light electrical field is concentrated in the middle of the laser, where the active material is located [90]. This increase the efficiency of the stimulated emission, but the thickness of the cavity is limited. By this concentration of the energy some heating problems can damage the active organic material. To overcome this problem and to bring same other advantages a new VCSEL structure is proposed and patented at INA, University of Kassel in 2003 [91]. This structure is called complex coupled laser structure.

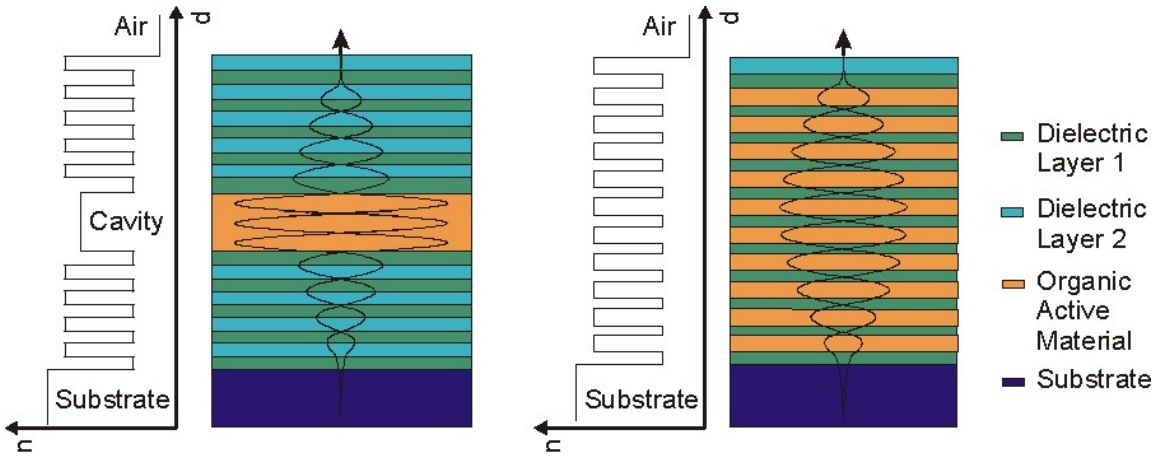

Fig. 2-25. VCSEL structures with refractive index profile. The multilayer configuration requires an alternating sequence of high and low refractive index materials: (a) Index coupled laser structure with concentrated energy of the electrical field in the cavity of the VCSEL; (b) Complex coupled laser structure with distributed energy of the electrical field [91].

In Fig. 2-25b the complex coupled laser [91] structure with distribution of the electrical field and the refractive index profile is shown. In this case the active material is distributed in the structure. All parts of the light electrical field can be used. The energy is distributed in the whole structure. Nevertheless, this structure is more complicated for deposition and does not have the possibility for tuning of the emitted wavelength. The side modes are more predominant because the lasing takes place at the left or the right side of the stop band.

In general the VCSELs provide high degree of wavelength selectivity. To achieve constructive interference of all partially reflected waves at the interfaces the structure should obey on the following equation:

$$n_1 d_1 + n_2 d_2 = \frac{1}{2}\lambda \qquad 2.40$$

where

λ	free-space wavelength
n_1, n_2	refractive index of material 1 and 2
d_1, d_2	thickness of the layers 1 and 2

The wavelength in equation 2.40 is chosen to coincide with the maximum of the optical gain of the organic active material. The height of the laser is not more than several micrometers. Therefore the longitudinal mode confinement is sufficiently large to allow only one longitudinal mode to operate. However, there may be more lateral modes depending on the lateral size of the cavity.

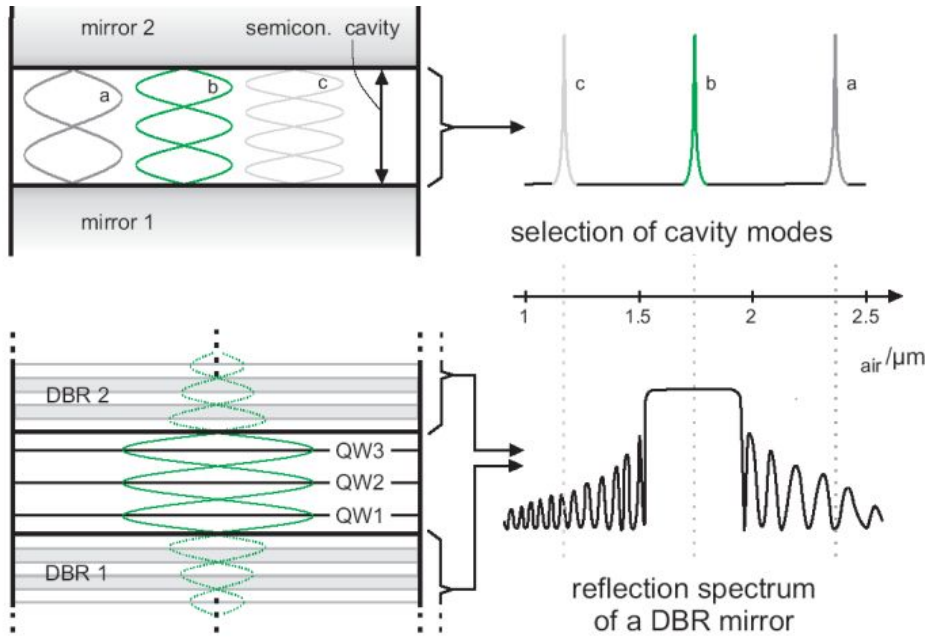

Fig. 2-26. Spectral components of the VCSEL structure. Standing waves in the cavity with the resultant spectrum (above) and the reflectivity of the DBR 1 and DBR 2 shown with brackets (bottom) [92]

In Fig. 2-26 the spectral components of the VCSEL structure are shown. It consists of the spectrum of the standing waves in the cavity in combination with the reflectivity of DBR structures [92]. In Fig. 2-27 the resultant reflectivity of the VCSEL structure with main-mode at 300 nm is shown.

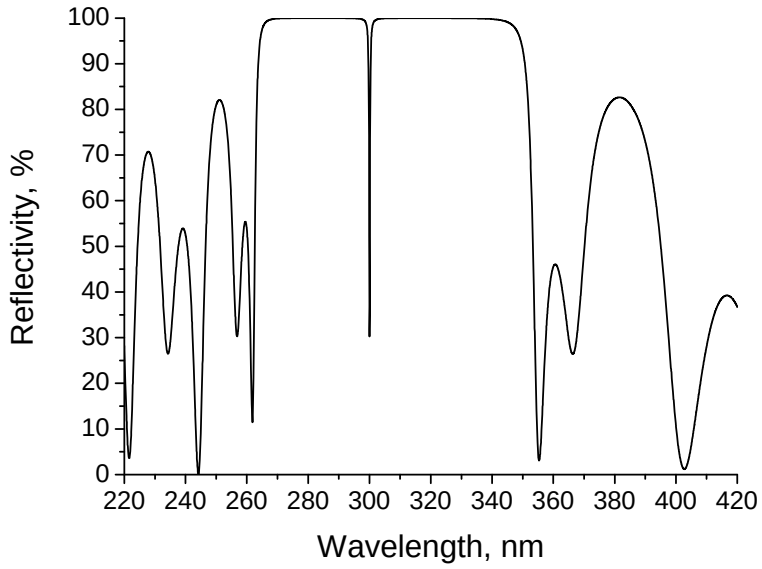

Fig. 2-27. Reflectivity spectrum of VCSEL with design wavelength 300 nm.

The Distributed Feedback Lasers consist of an active medium in which a periodic thickness variation is introduced in one of the layers as a forming part of the heterostructure [93; 94; 95]. In Fig. 2-28 schematic DFB structures with a uniform and λ/4-shifted grating are shown. In this case the organic active material is deposited on a structured layer with periodic thickness variation. Since the active material has larger refractive index than the adjacent mediums, the electric field of the oscillating mode will see an effective refractive index n_{eff} along the z-coordinate [96; 97]. Similar to the DBR idea, the DFB laser (see Fig. 2-28a) is effectively coupled with constructive interference if the free space wavelength of the radiation fulfills following equation:

$$\lambda = \lambda_B = 2\langle n_{eff}\rangle\Lambda \qquad 2.41$$

where

λ	free-space wavelength
Λ	the pitch of the periodic thickness change
n_{eff}	effective refractive index

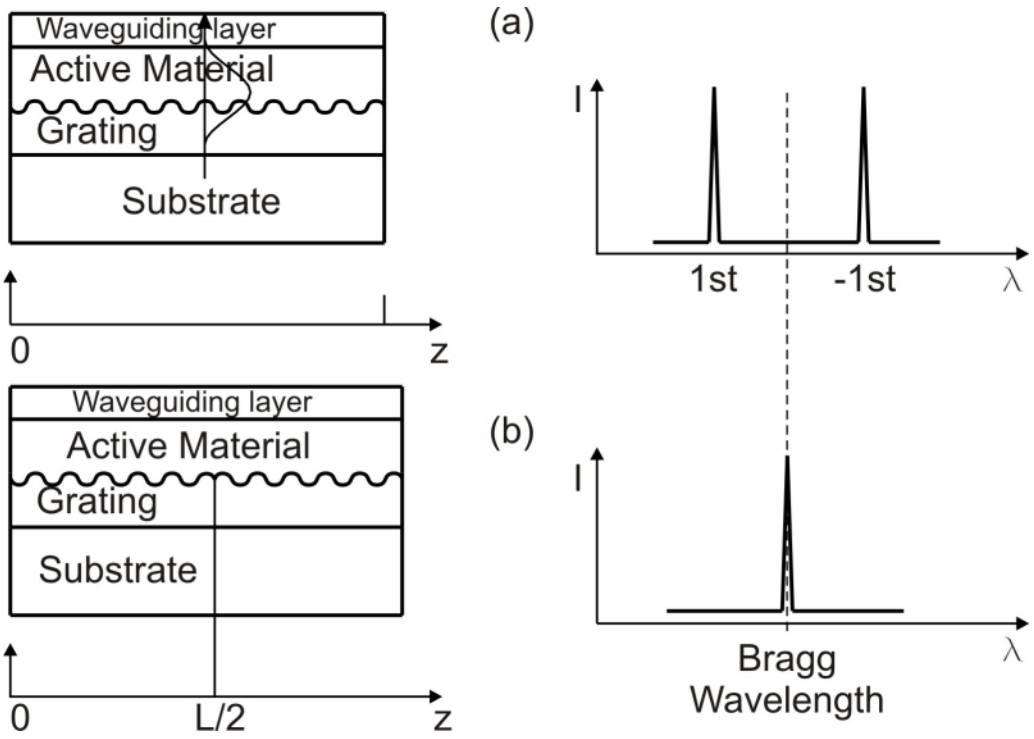

Fig. 2-28. Schematic structures of DFB laser with (a) a uniform and (b) λ/4-shifted grating. At the first case there are two symmetrical modes and at the second case there is only one mode exactly at the design Bragg wavelength.

The emission of this DFB laser is characterized by two symmetrical modes. In the most cases this multimode behavior is not desirable. To solve this problem the so called λ/4-shifted DFB laser was proposed [98]. The main idea is to incorporate a shift of λ/4 at the center of the periodic grating (see Fig. 2-28b). As a result the peak of the emission occurs exactly at the resonance wavelength λ. Furthermore, the difference between this mode and the two neighboring modes, i.e. the mode selectivity, is higher.

The fabrication of uniform-grating devices and λ/4-shifted DFB lasers presents challenging technological problem. It is difficult to make uniform pitch along the length of the grating and also constant from one grating to the next.

This work will emphasize on simulation, optimization and experimental investigation of VCSEL structures using new hybrid organic-inorganic material systems. The active region is optically pumped by an external light source with a shorter wavelength. In this case a nitrogen laser with emission at λ=337 nm is used.

Chapter 3

Theoretical model calculations and optimizations of VCSELs

The purpose of this chapter is to show the calculations, simulations and optimizations of the multilayers and VCSELs structures. The program Spectrafit written by F. Römer at the Institute of Nanostructure Technologies and Analytics (INA), was used as simulation software. Spectrafit is based on the transfer matrix method, which has already been discussed in Chapter 3. The software Spectrafit is not calibrated (the calibration is not a topic of this work) and represents the results in a.u. (arbitrary units), which are used only for comparison and analyses of the simulated VCSEL structures. To have comparable simulation data only one parameter is changed during the simulation series. To reduce the error, which comes from the used precision, all the calculations for a certain group are done in one and the same wavelength range.

3.1. Simulation and optimization of the Distributed Bragg reflector (DBR) mirror

The distributed Bragg reflector is a multilayer structure and consists of materials with different refractive indices. The sequence of the refractive index should insure a constructive interference for the desired wavelength of the incident radiation. The purpose of the DBR mirror is to give a high reflectivity to the optical applications in range of the light covered from the stop band. Such applications are for example the VCSELs, which require a reflectivity of the mirrors more than 99,9%. The reflectivity with conventional metal mirrors is not more than 95%, which is not enough for the necessarily feed-back of the light. Furthermore, all of

the metal materials are strongly absorptive in the ultraviolet range which is the desired wavelength in this work.

In the transfer matrix method it is assumed that the interfaces between the layers are perfectly abrupt and there is no roughness. The properties of the materials, suitable for the applications operating in the ultraviolet range should cover some requirements. Such a requirement is for example the absorption of the materials used in the DBRs. In Fig. 3-1 the dependence of the reflectivity from the period numbers for different absorptions is shown. All DBR structures are simulated with design wavelength at λ_d = 300 nm. The absorption is changed only for the material with high refractive index, whereas the absorption for the second material with low refractive index is kept zero.

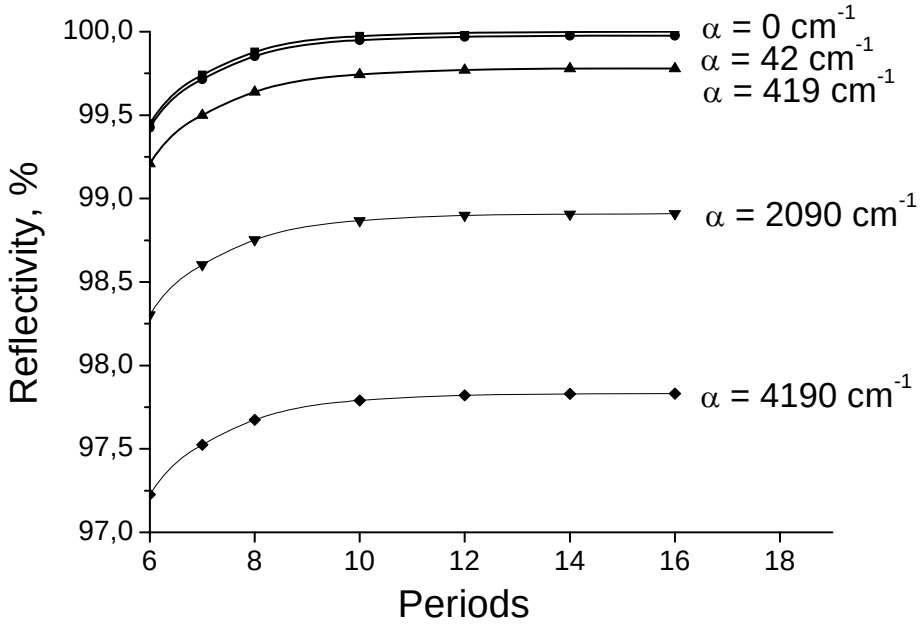

Fig. 3-1. Reflectivity dependence of the DBRs with different number of the periods and with different absorption of the material with the high refractive index. By certain value of the absorption even by increasing the total number of the periods the reflectivity cannot be increased.

The Fig. 3-1 shows that even by a small absorption in one of the layers in the DBR, the total reflectivity of the structure is strongly reduced. By a certain value of the absorption even by increasing the total number of the periods, the reflectivity cannot be increased. The full with of the half maximum (FWHM) of the stop band

is not significantly influenced by the change of the absorption coefficient. On the Fig. 3-2 that the FWHM is strongly decreased by increasing the number of the periods is shown. Be further increasing of the periods the FWHM is not changed and depends only from the refractive index contrast.

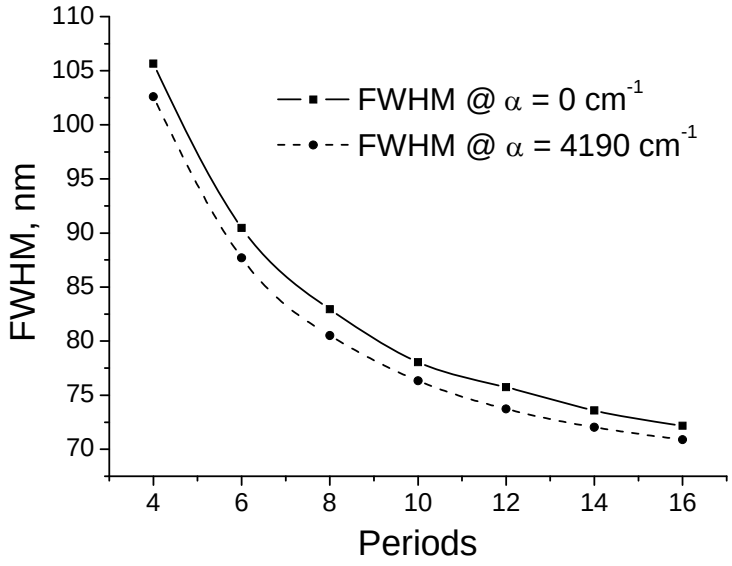

Fig. 3-2. Dependence of the FWHM of DBR structures versus the number of the periods and the absorption of the layer with the high refractive index. The FWHM is not strongly influenced by the change of the absorption, whereas the number of the periods makes a big difference.

The results from this simulations show that the materials used for the multilayer structure should have negligible absorption or no absorption at all. As mentioned before only several materials are totally transparent in the ultraviolet range. Such materials are some dielectric materials, for example the oxides, nitrides and fluorides of certain metals. In Table 2 are shown some dielectric materials with their refractive index and absorption coefficient at 300 nm wavelength. The chemical formulas and the classification concerning the value of the refractive index are also included.

Table 2. Dielectric materials used for deposition of multilayer structures and optical coatings in the ultraviolet range. The table shows literature data for the refractive index and absorption coefficient at 300 nm wavelength, the chemical formula and the classification concerning the value of the refractive index.

Materials	**Refractive index at 300 nm, [-]**	**Absorption coefficient at 300 nm, [cm^{-1}]**
MgF_2 [99; 100; 101; 102]	1.40 (low index)	0
SiO_2 [103]	1.49 (low index)	0
Al_2O_3 [104]	1.81 (medium index)	0
Y_2O_3 [105; 106]	1.89 (medium index)	113
HfO_2 [107; 108]	2.06 (high index)	0
ZrO_2 [105; 109; 110; 111]	2.45 (high index)	0
Si_3N_4	2.47 (high index)	51830
TiO_2 [112]	3.05 (high index) at 430 nm	28050

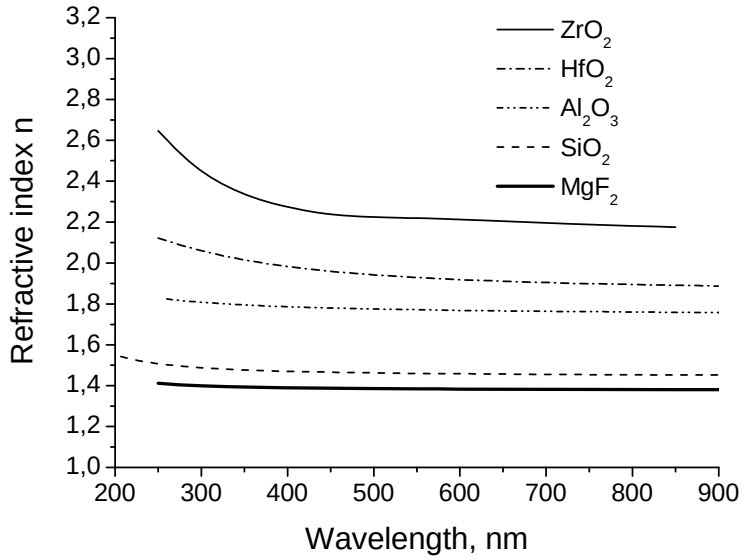

Fig. 3-3. Refractive index dispersion of dielectric materials with very low absorption in the ultraviolet range. The data are used for simulation and optimization of the DBRs.

In Fig. 3-3 are shown the refractive index dispersion of materials from Table 2 with absorption equal to zero.

The simulations are performed only for some material combinations, which are relevant to this work. As a substrate a silicon wafer with crystal structure is used. The sequence of the alternating refractive index is designed to ensure a constrictive interference. The thickness of the layers is a quarter of the design wavelength (in this case λ_d = 300 nm) in the corresponding material.

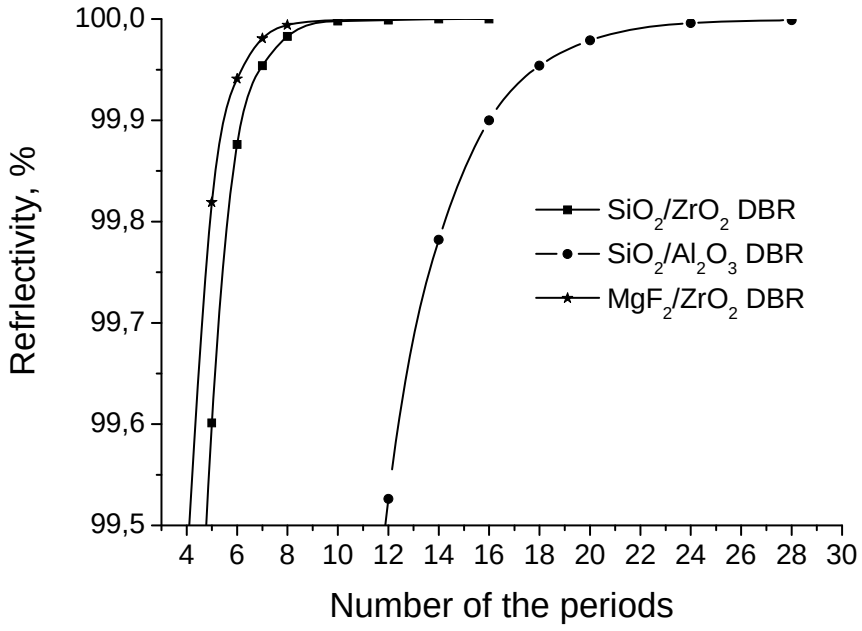

Fig. 3-4. Reflectivity of DBRs with combination of materials with different refractive index contrast. The multilayer structure MgF_2/ZrO_2 has achieved the reflectivity close to 99,99% with less periods than the other structures.

In Fig. 3-4 the reflectivity of DBR multilayer structures with combinations of materials with different refractive indices is shown. The best reflectivity with fewer periods is achieved by the structure with the biggest refractive index contrast, namely MgF_2/ZrO_2 DBR.

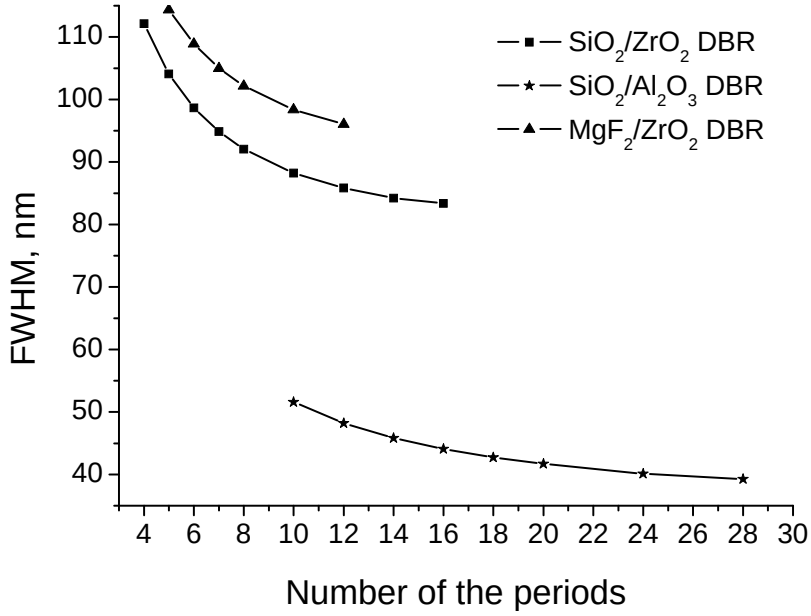

Fig. 3-5. Dependence of FWHM of the stop-band from the number of the periods for different DBR structures. The biggest FWHM has the structure with the biggest refractive index contrast.

In Fig. 3-5 the dependence of the FWHM from the number of the periods for different DBR structures is shown. The smallest FWHM of about 45 nm is obtained by the structure with combination of SiO_2 and Al_2O_3 materials. The refractive index contrast of these materials is very small, $\Delta n = 0{,}32$ at the wavelength $\lambda = 300$ nm. That is why more periods (24 periods) are necessary to be achieved a reflectivity over 99,99%. In practice SiO_2/Al_2O_3 DBRs are used for applications which require a small stop-band and high reflectivity in the ultraviolet range down to 200 nm. This is possible because of their low absorption in the short wavelength spectrum. The MgF_2/ZrO_2 DBR structure has the biggest refractive index contrast of $\Delta n = 1{,}05$ at $\lambda = 300$ nm. It has achieved the widest stop-band of about 105 nm and the highest reflectivity (over 99,99%) with fewer periods (only 8 periods), but due to some problems by the deposition of the MgF_2 the structure is excluded from this work. Such a problem is, for example: to achieve a stoichiometric MgF_2 material a pure fluorine gas has to be introduced in the deposition chamber. The fluorine gas is very reactive and will destroy the active organic material of the laser and even more, the chamber and the pumps of the deposition machine have to be designed in a special way.

In Fig. 3-6 are shown and compared the stop-bands of DBRs with different materials. It is obvious that the different structures need different number of periods in order to achieve a reflectivity more than 99,99%. In some of the next experiments it is shown that the broader stop-band will reduce the influence of the side-mode in the VCSEL emission.

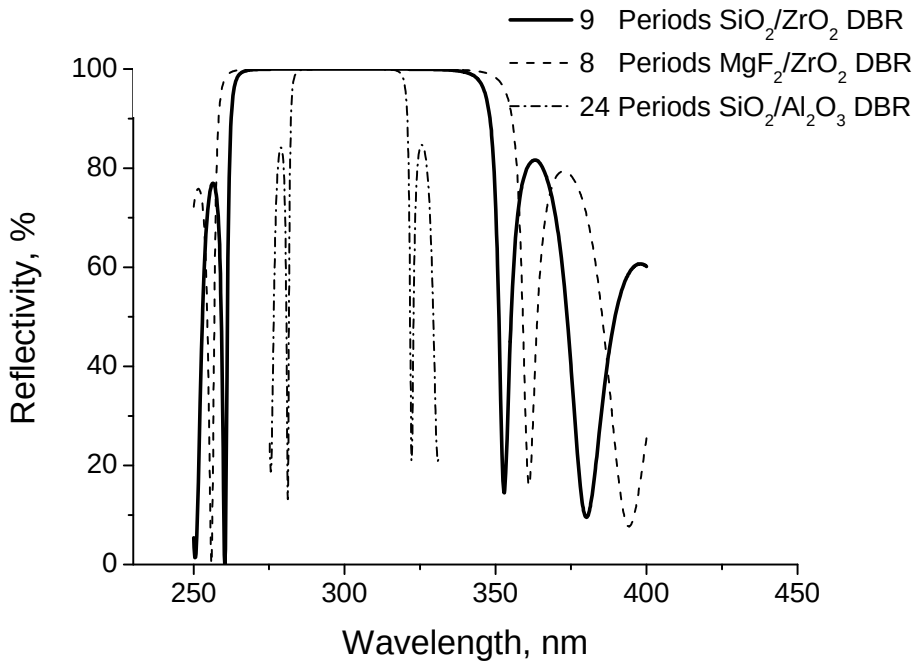

Fig. 3-6. Comparison of the DBR stop-bands and the needed periods for the different structures in order to achieve reflectivity more than 99,99%.

The most interesting combination for the VCSEL in the ultraviolet range is the SiO_2/ZrO_2 multilayer structure. Only 9 periods of SiO_2/ZrO_2 are needed to be achieved a reflectivity more than 99,99% with stop-band of about 92 nm. The refractive index contrast is $\Delta n = 0{,}96$. The deposition process of the SiO_2, ZrO_2 and some other dielectric materials are discussed later in this work. By introducing additional oxygen in the deposition chamber, oxide materials close to the stoichiometric conditions are deposited.

3.2. Simulation and optimization of the filter structure

The multilayer filter structure is the base structure of the VCSEL device. The filters consist of top and bottom DBRs and a cavity between them. The both DBRs ensure very high reflectivity and resonance with maximum amplitude of the standing wave in the cavity. If an active material is placed there, an amplified stimulated emission can be achieved. Before starting the simulation of the VCSELs, some optimization of the filter structures is needed.

As it was calculated, only 9 periods SiO_2/ZrO_2 structure are necessary to achieve a reflectivity, more than 99,99% with stop-band of about 92 nm at design wavelength 300 nm. The cavity thickness is calculated by the following equation:

$$d_{cavity} = \frac{1}{2} m \frac{\lambda_{design}}{n_{mat}}, (m = 1, 2, 3, \dots) \quad 3.1$$

where

λ_{design} free space design wavelength

n_{mat} refractive index of the material at the λ_{design} wavelength

The simulated filter has structure as it is shown in the Table 3:

Table 3. Structure of the filter used for the simulations. The number of the DBR periods is chosen to ensure a reflectivity more than 99,99%.

9 periods top SiO_2/ZrO_2 DBR
variable thickness of the cavity calculated from the Eq. 3.1 with different values for *m*. The material is chosen to have high refractive index. In this case is ZrO_2
10 and ½ periods bottom SiO_2/ZrO_2- SiO_2 DBR
Si-wafer is used as a substrate

In this structure the filter dip is exactly at 300 nm with simulated FWHM less than 0,1 nm. The reflectivity of the structure is calculated to be more than 99,9999%. In the calculations is assumed that the materials do not have any

absorption, the roughness is zero, the layers in the structure are perfectly parallel and the precision of the calculated values is $1x10^{-6}$.

In Fig. 3-7 the distance between the transmitted filter dips and the coefficient *m* from Eq. 3.1 is shown. The thickness of the cavity defines the resonance wavelength. At this wavelengths are the modes of the filter structure. If this modes are inside the stop-band and are different from the design wavelength, than they are known as cavity side-modes. They are in energy scale equidistant to the left and to the right side of the main-mode. At the lower thickness of the cavity the cavity side-modes are outside of the stop-band. In this case the side-modes are the edges of the DBR stop-band itself. By increasing the cavity thickness the left and the right cavity side-modes appear in the stop-band. By further increasing of the cavity thickness the side-modes are getting closer to the main-mode.

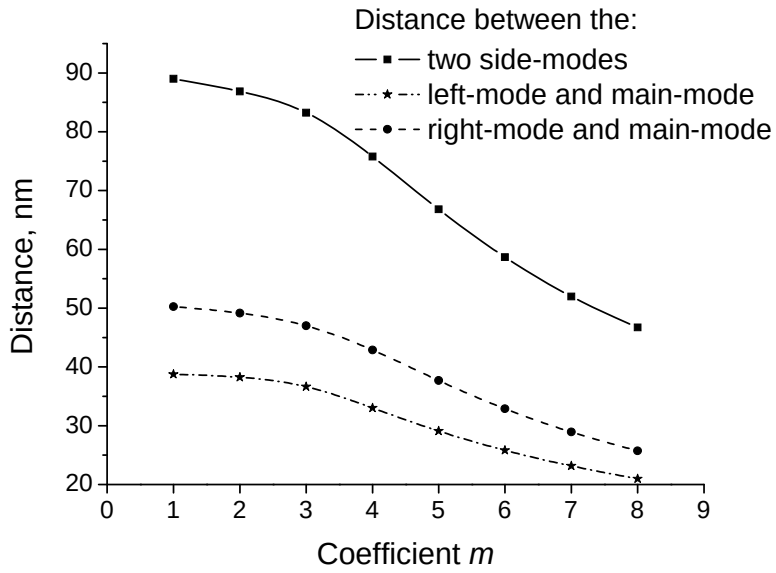

Fig. 3-7. Dependence between the distances of the transmitted filter dips from the coefficient *m* (the thickness of the cavity from Eq. 3.1) for the structure from Table 3. By increasing the cavity thickness the side-modes are getting closer to the main-mode.

In Fig. 3-8 the reflectivity of the structure from Table 3 with thickness of the cavity corresponding to coefficient $m = 7$ is shown. The physical thickness of the cavity with this coefficient is 428,57 nm. Two additional side-modes appear in the stop-band: The left side-mode is at the position 277 nm and the right side-mode is at 329 nm. The FWHM of the stop-band is 87,20 nm.

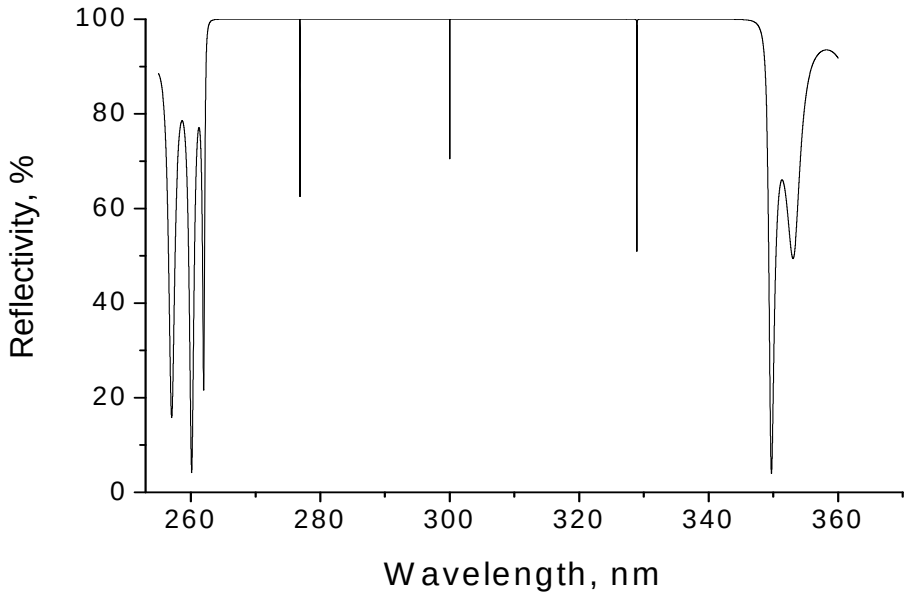

Fig. 3-8. Simulated reflectivity of the structure from Table 3 with thickness of the cavity corresponding to coefficient $m = 7$. In the stop-band two side-modes are visible.

In the VCSEL structure the side-modes can cause reduction of the side-mode suppression ratio (SMSR). The mode competition is stronger and the laser operates in multi-mode regime.

3.3. Optical data used for simulation and optimization of UV VCSEL structures

The VCSEL structure consist of bottom and top DBRs. Between the mirrors in the cavity is located the active material. Both DBRs deliver high reflectivity, which is needed for the feed-back of the light. The maximum intensity of the standing wave is concentrated at the cavity of the structure, where the active material is deposited. This laser is so called index coupled VCSEL. Other possible structure is the complex coupled VCSEL. In this configuration the active material is distributed in the multilayer stack and participates in the alternating refractive index arrangement for the DBR. In this work structures with different material combinations are evaluated and compared.

The active material used in the simulations has high refractive index, which corresponds to the used organic materials in practice. In Fig. 3-9 the refractive index dispersion and the extinction coefficient of the active material are shown.

The relation between the extinction coefficient *k* and the absorption is given by the Eq. 3.2.

$$k = \frac{\lambda}{4\pi}\alpha \qquad 3.2$$

where

λ	wavelength in the vacuum
α	absorption

The gain profile of the active material (shown in Fig. 3-10) has maximum intensity at the wavelength 300 nm. The gain data are generated in analogy to the organic active material Spiro-Octopus-1 with maximum emission at 395 nm. This gain profile is used only for the purpose of the simulations, optimizations and comparison of the UV VCSEL structures. The refractive index dispersion of the dielectric materials used for the DBRs for the simulations of the lasers is taken from the Fig. 3-3.

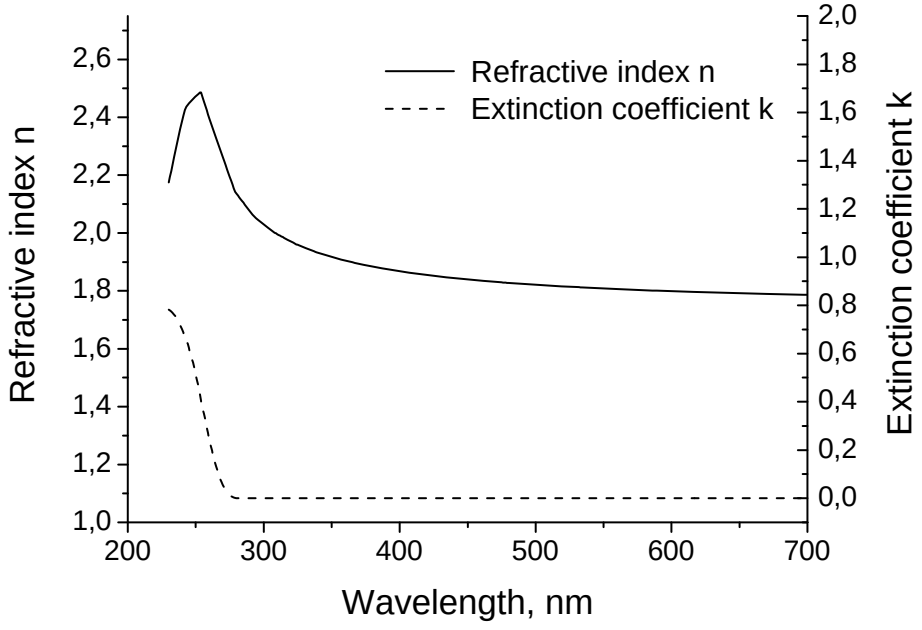

Fig. 3-9. The refractive index dispersion and extinction coefficient of the active material. The absorption at the design wavelength 300 nm is zero. The material participates in the multilayer structure as high refractive index material. The data are measured with spectroscopic ellipsometer.

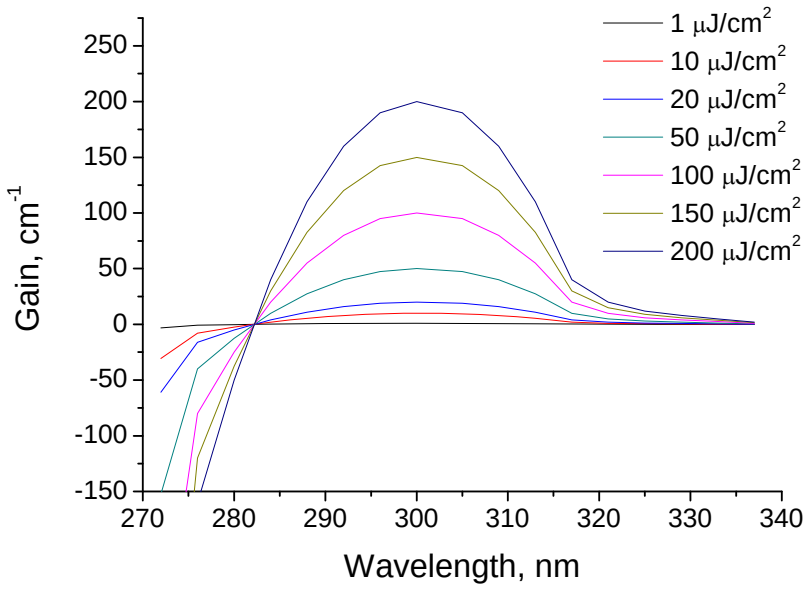

Fig. 3-10. Gain diagram of the active material used by the simulations. The gain is generated from Spiro-Octo-1 for maximum at 300 nm.

3.4. Simulation and optimization of index coupled UV VCSEL

The index coupled VCSEL has a structure similar to the conventional laser. As high refractive mirrors are used dielectric DBR mirrors. The active material is placed in the cavity and has thickness in order of the design wavelength (in most cases $\lambda / 2$ or λ). This ensures the single mode operation of the laser. The structure is schematically shown in Fig. 3-11.

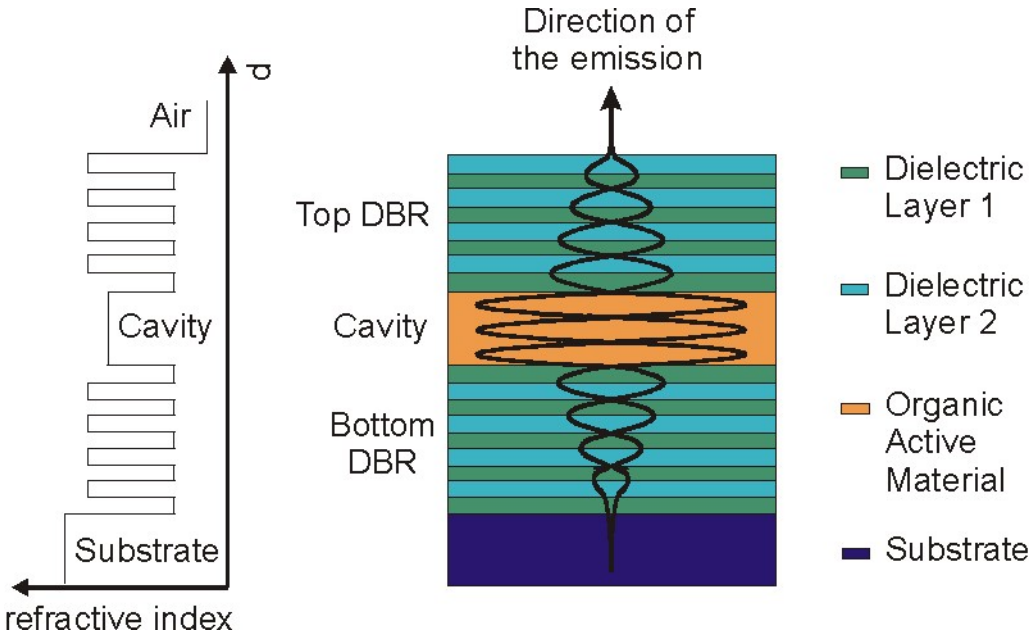

Fig. 3-11. Structure of the index coupled VCSEL with top and bottom DBRs. The active material is located in the cavity. On the left side the refractive index sequence of the materials in the layers is shown.

The active material is located in the middle of the structure, where the intensity of the standing wave has maximum value. The cavity thickness is calculated in such a way to ensure oscillation of the emitted wavelength. Similar to the filter structure the desired radiation is filtered with very small FWHM of the emitted spectrum. The refractive index sequences of the materials and the layer thicknesses should ensure constructive interference of the design wavelength.

In the simulation software the carrier density of the active material is used to show the pumping power. The charge carrier density denotes the number of charged carriers per volume, which is measured in cm^{-3}. Whereas, the charge density is the number of charges per volume at a given energy. The carrier density is obtained by integrating the charge density over the energy that the charges are

allowed to have. The carrier density is used in the simulations as the most important parameter for the analysis of different structures.

The lasing threshold is the lowest excitation level, at which the laser's output is dominated by stimulated emission rather than by spontaneous emission. At this point the losses are exactly compensated from the gain. Below the threshold, the laser's output power rises slowly with increasing excitation. Above threshold, the slope of power vs. excitation is orders of magnitude greater. The line-width of the laser's emission also becomes orders of magnitude smaller above the threshold than it is below. Above the threshold, the laser is said to be lasing. The lasing threshold is reached when the optical gain of the laser medium is exactly balanced by the sum of all the losses experienced by light in one round trip in the optical cavity of the laser.

In Fig. 3-12 the required carrier density at the lasing threshold versus the number of the periods of the bottom DBR is shown. In this case the top DBR has one period less than the bottom DBR mirror, which allows the emission to be coupled out from the top side of the VCSEL.

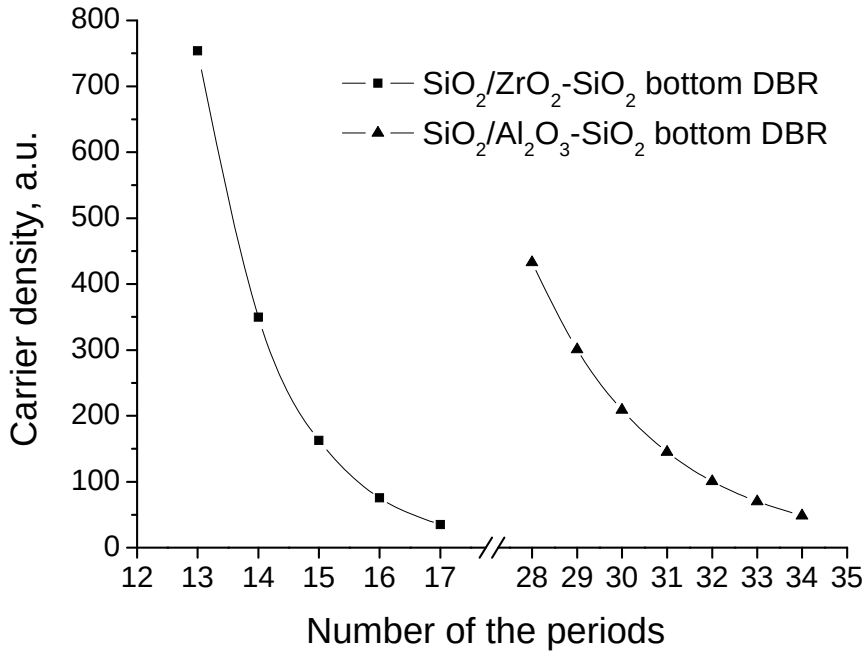

Fig. 3-12. Dependence of the required carrier density at the lasing threshold versus the number of the periods of the bottom DBR. The top DBR is assumed to have one period less. The active material has thickness of one λ for design wavelength 300 nm.

The active material has maximum gain at 300 nm. It is placed in the cavity with thickness one λ (*m* = 2, see Eq. 3.1). In this case the physical thickness is d = 147,78 nm. For the DBRs are used material combinations of high and low refractive index contrast. The SiO_2/ZrO_2 mirror represents the DBR with high refractive index and the SiO_2/Al_2O_3 represents the DBR with low refractive index. From Fig. 3-12 can be concluded, that the laser structures with DBRs with high refractive index contrast need less number of periods to achieve lasing threshold at certain carrier density.

For SiO_2/ZrO_2 bottom mirror are required only 16 periods to be achieved lasing threshold at carrier density 75,3 a.u., whereas in case of SiO_2/Al_2O_3 bottom mirror are needed 33 periods and 70,1 a.u. carrier density. By decreasing the number of the periods the required carrier density increases rapidly. It is calculated, that for laser structure with 13 periods SiO_2/ZrO_2 bottom DBR the required carrier density has a value of 753,8 a.u..

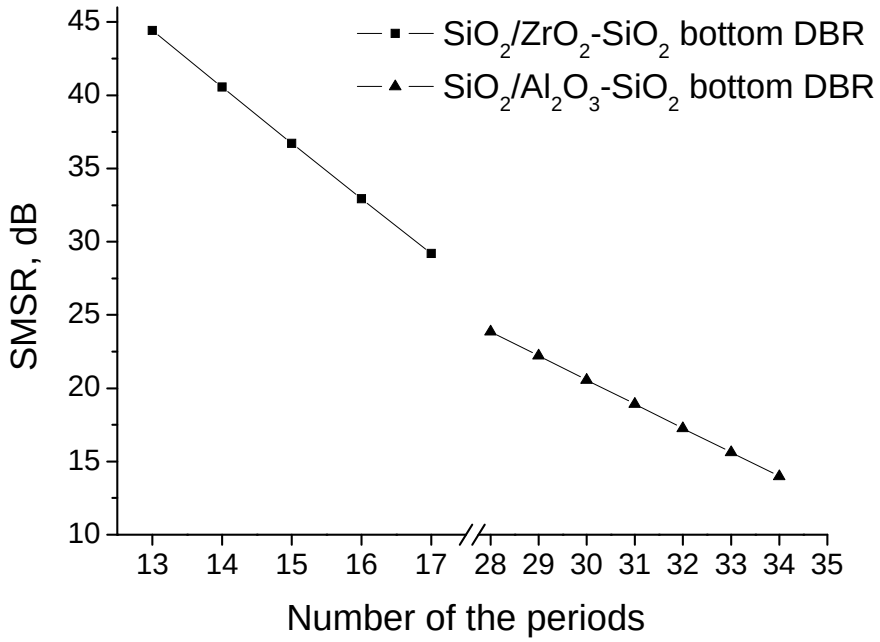

Fig. 3-13. Dependence of the side-mode suppression-ratio of the emitted radiation from the number of the bottom DBR periods. The calculations are done at the lasing threshold. The structure with bigger stop band has better SMSR, because the distance between the side-modes and the main-mode is bigger.

In Fig. 3-13 the dependence of the side-mode suppression-ratio of the emitted radiation from the number of the bottom DBR periods with different materials is shown. All the calculations are done at the lasing threshold. The structure with wider stop-band has better SMSR, because the distance between the side-modes and the main-mode is bigger. The dependence of the distance can be seen on the Fig. 3-14. It was simulated, that for laser structure with 15 periods SiO_2/ZrO_2 bottom DBR and carrier density 162,5 a.u. the SMSR is 37 dB. Compared to the structure with 31 periods SiO_2/Al_2O_3 bottom DBR and carrier density 145,2 a.u. the SMSR is much smaller and has value of 18,9 dB.

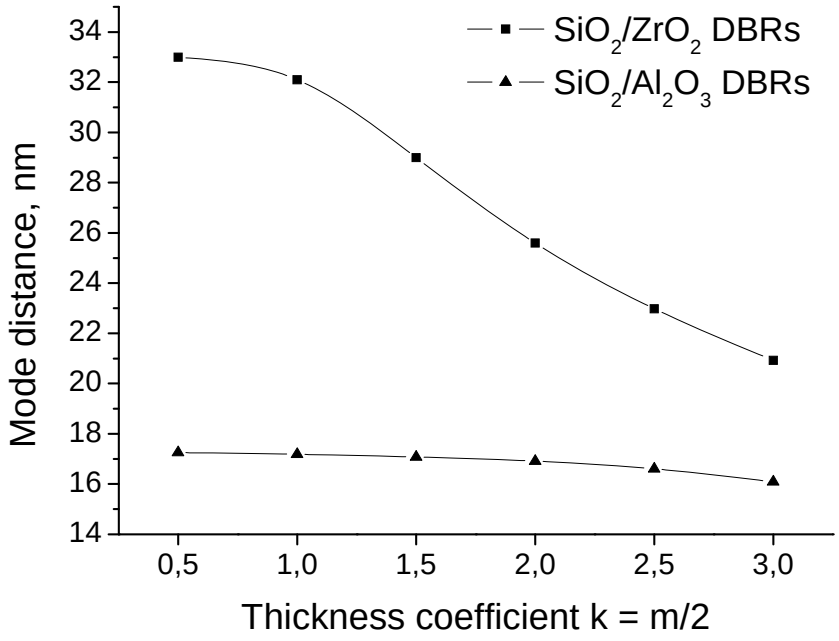

Fig. 3-14. Dependence of the distance between the main mode and the left side mode from the cavity thickness. The side mode for the DBR with low refractive index is closer to the main mode.

In Fig. 3-14 the dependence of the distance between the main-mode and the left side-mode from the cavity thickness is shown. The cavity thickness is represented with thickness in wavelengths, which is equal to *m*/2 (see Eq. 3.1). The periods of the DBRs are kept constant. For the laser structure with SiO_2/ZrO_2 DBRs the number of the periods are 15 for the bottom and 14 periods for the top DBR. For SiO_2/Al_2O_3 structure the number of the bottom DBR periods is 31 and for the top are 30. The side-mode, which comes from the DBR stop-band, for the

multilayer structure with low refractive index contrast (SiO_2/Al_2O_3) is closer to the main-mode. The distance does not depend on the cavity thickness and has almost linear graphic. The curve for the structure with wider stop-band has bigger decay of the SMSR because the cavity side-modes appear in the stop-band.

In Fig. 3-15 can be seen the dependence of the carrier density for lasing threshold versus the thickness coefficient *k* (*k* = *m*/2). By increasing the thickness of the active material the required carrier density decreases. From other side by increasing the cavity thickness the side-modes are more predominant and the SMSR decreases.

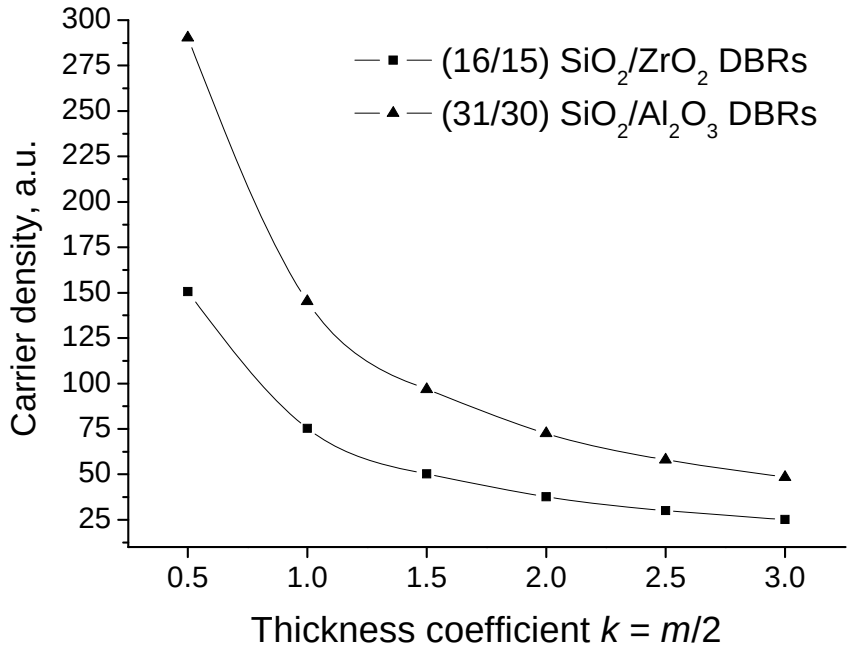

Fig. 3-15. The carrier density for lasing threshold versus the thickness coefficient *k* (*k* = *m*/2). By increasing the thickness of the active material the required carrier density decreases.

From the simulations and the analysis made so far it can be concluded, that the VCSEL structure with SiO_2/ZrO_2 DBRs has lower SMSR, the required carrier density at the lasing threshold is smaller, and the necessary number of the periods for the DBRs are less. In practice, from deposition point of view this structure is easier to be produced. The intermediate surfaces are less and the error is smaller because of the surface roughness.

At last but not least are the production costs. The deposition time of this structure is shorter compared to the VCSEL structure with SiO_2/Al_2O_3 DBRs. Because of the highly sophisticated machines used in the deposition process, the occupation time and the man power are critical in the formation of the price. The reduction of the deposition time leads to reduction of the production costs and to cheaper device.

The following simulations and analysis are concentrated on UV VCSEL structures with SiO_2/ZrO_2 DBR mirrors.

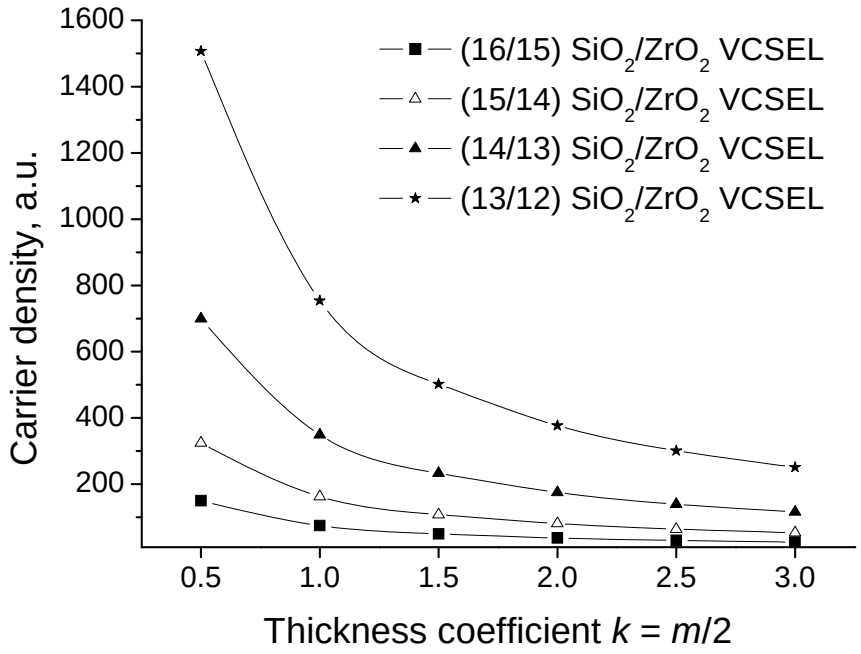

Fig. 3-16. Required carrier density at lasing threshold for VCSEL structures with different number of the periods vs. the thickness of the cavity.

The carrier density is one of the most important parameters, which is measured in cm^{-3}. It shows the required pumping power in which the laser threshold is achieved. As mentioned already on p.62, the carrier density in this work is represented in a.u. In the simulations it is assumed that the maximum value of the carrier density is 250 a.u., which is used as reference value. All the simulations are compared and optimized in respect to this value.

Fig. 3-16 shows the dependence of the necessary carrier density at lasing threshold for structure with different number of periods versus the thickness of the active material. By increasing the number of the periods the required carrier density decreases. The same happens by increasing the active material thickness. So the structure with 16 periods of the bottom DBR and cavity thickness at $k = 0{,}5$ needs carrier density of 150 a.u., or structures with 15 periods of the bottom DBR and cavity thickness at $k = 1{,}0$, needs carrier density of 163 a.u.. In general, structures with less number of the periods are preferred.

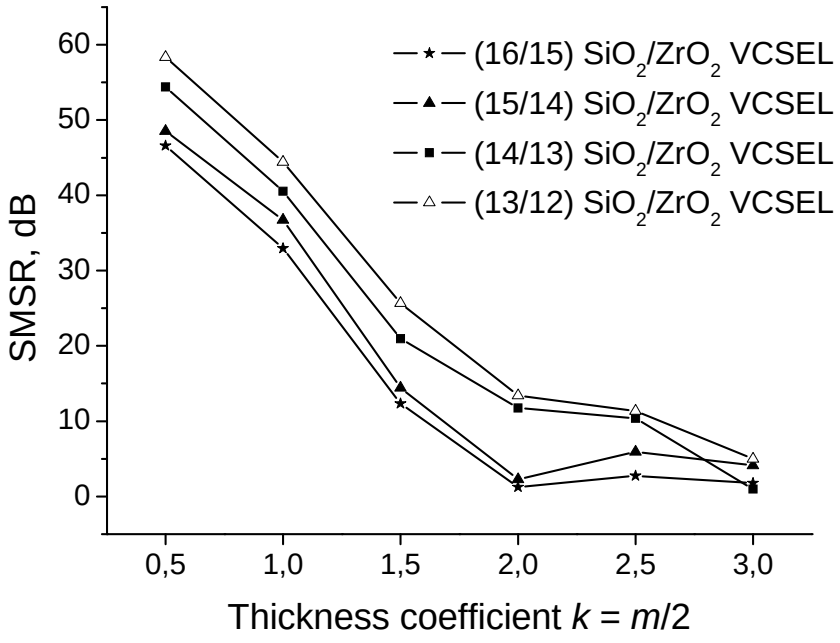

Fig. 3-17. SMSR of the emitted radiation for different thicknesses of the cavity. The simulated VCSELs are with different numbers of the periods. The SMSR reduces by increasing of the cavity thickness.

Other important parameter is the side-mode suppression-ratio (SMSR) of the emitted radiation. The value shows how much the main-mode is predominant over the side-modes in dB. In Fig. 3-17 can be seen that the SMSR reduces by increasing the cavity thickness. The deviations in the curves at thicker cavity are because of the closer standing side-modes and the mode competition between them. Decreasing the number of the periods results in increasing of the SMSR, but less periods requires more pumping power (see Fig. 3-16). The structure with 16 periods of the bottom DBR and cavity thickness at $k = 0{,}5$ has SMSR equal to 47 dB and structures with 15 periods of the bottom DBR and cavity thickness at $k = 1{,}0$ has 37 dB.

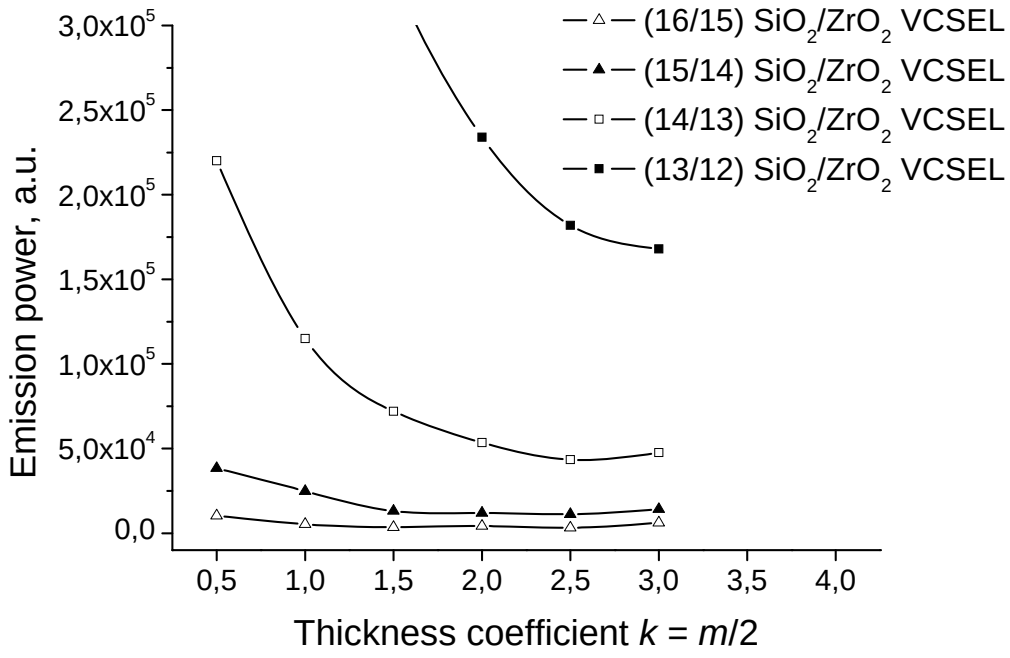

Fig. 3-18. Dependence of the emitted power versus the thickness of the active material. The VCSEL structure with low reflective DBRs shows higher emission power.

The power of the emission depends on the reflectivity of the mirrors and the gain of the active material. Fig. 3-18 shows the emission power of structures with different reflectivity of the mirrors versus the thickness of the active layer. The VCSEL structure with low reflective DBRs shows higher emission power, but the required pumping power for lasing threshold is very high. The lasers with high reflective DBRs keep and concentrate the power in the structure. The usable emission of the laser is lost for the structure and the gain processes.

The required carrier density for lasing threshold depends very much on the number of periods of the top DBR. In Fig. 3-19 are shown simulations of VCSEL structures with different periods of the top DBR. The bottom DBR is kept constant. The optimal structure has top DBR with 0,5 or 1,5 periods less. In this case a VCSEL with 15 periods bottom DBR is calculated and simulated. The laser with top DBR with 14 or 15 periods shows reasonable amount of carrier density of about 170 a.u.

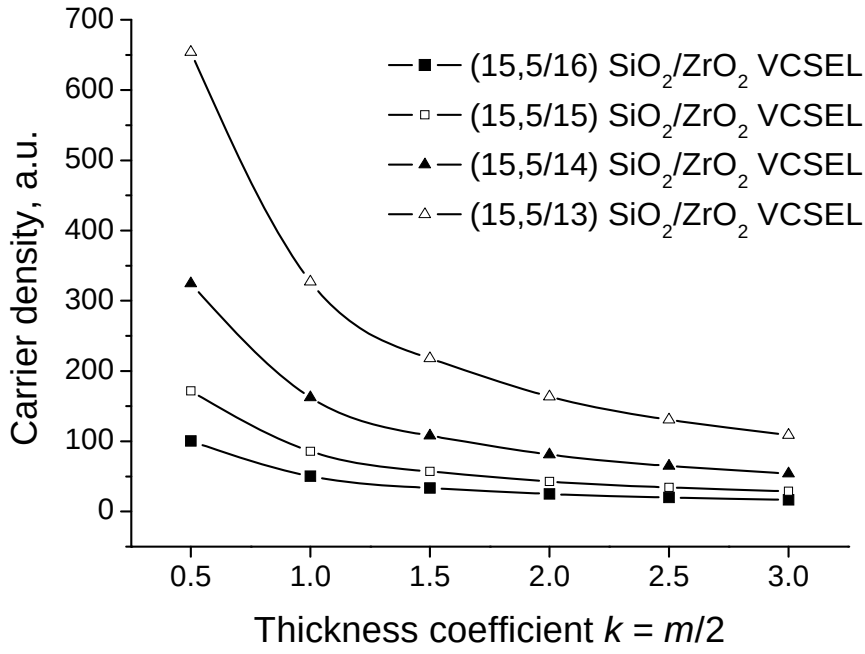

Fig. 3-19. Required carrier density at lasing threshold for VCSEL structures vs. the thickness of the cavity. The periods of the bottom DBR are kept constant.

After the simulations and the analysis made so far it can be concluded, that the structure from Table 4 shows the best results. The required carrier density is below the critical level of 250 a.u. assumed before (see page 79) and has value of 162 a.u.. The SMSR is 37 dB. In Fig. 3-20a are shown the reflectivity of the VCSEL structure of the entire stop-band with very thin transmission dip, and in Fig. 3-20b is the magnification of the transmission dip with better resolution of the wavelength. In Fig. 3-21a are shown the electric field distribution in the VCSEL structure and the refractive index profile, and in Fig. 3-21b is the emission spectrum of the VCSEL with main-mode at 300 nm.

Table 4. UV VCSEL structure with emission at 300 nm. The structure is chosen as a result of the performed simulations and analysis.

14 periods top SiO_2/ZrO_2 DBR
active material with optical thickness 1,0 λ (k = 1,0)
15 and ½ periods bottom SiO_2/ZrO_2- SiO_2 DBR
Substrate - Si-wafer

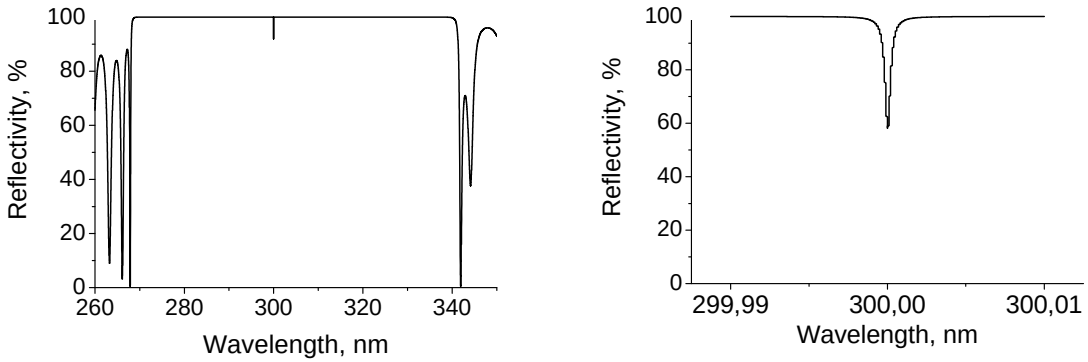

(a) (b)

Fig. 3-20. Reflectivity of the VCSEL structure from Table 4: (a) the entire stop-band with very thin transmission dip; (b) magnification of the transmission dip with better resolution of the wavelength.

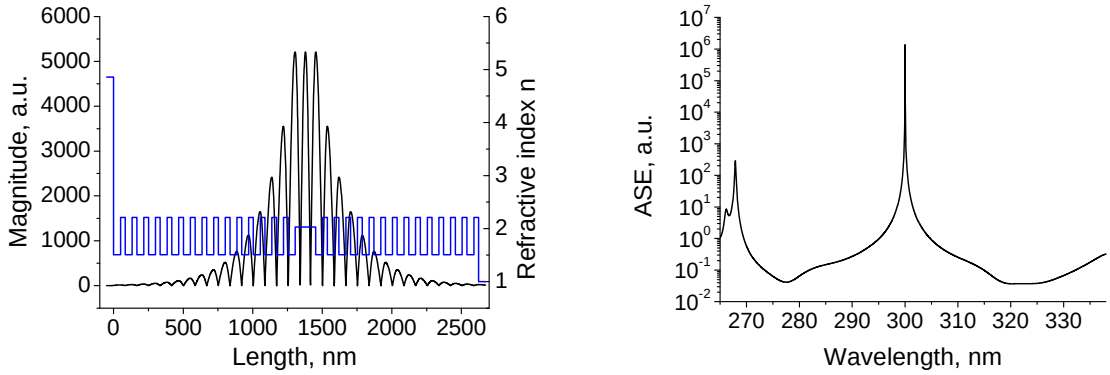

(a) (b)

Fig. 3-21. (a) The electric field distribution in the VCSEL structure and the refractive index profile; (b) The emission spectrum of the VCSEL with main-mode at 300 nm

3.4.1. Simulations and analysis of possible errors by deposition of the VCSEL structure

During the deposition some variation of the process parameters may occur. This leads to a variation of the physical and optical properties of the deposited materials. These deposition errors change the multilayer structure and reduce the optical properties of the VCSEL devices. The task of this investigation is to show how big are the influence of the deposition errors on the required carrier density at lasing threshold and the position of the main-mode. This work is concentrated on errors like deviation in the cavity thickness, deviation in the thickness of the ZrO_2 layers in the DBRs and different absorptions of the ZrO_2 layers. The results from the study are compared with the results from the simulation of ideal structure (Table 4).

All the simulations, calculations and analysis of the laser structures are done at design wavelength 300 nm.

3.4.1.1. Simulation of the error by deviation of the cavity thickness

By evaporation of the organic active material the thickness of the layer is difficult to be controlled. In this case a difference of the cavity thickness is occurred. Fig. 3-22 shows the dependence between the required carrier density at lasing threshold and the thickness deviation of the cavity in percents. By more than ±5 % difference the necessary carrier density at lasing threshold increases dramatically. By more than ±10 % is not possible any more to be reached lasing threshold.

The reason for the reduction in the optical properties of the laser is a result of the main-mode position and the constructive and destructive interference of the multilayer structure.

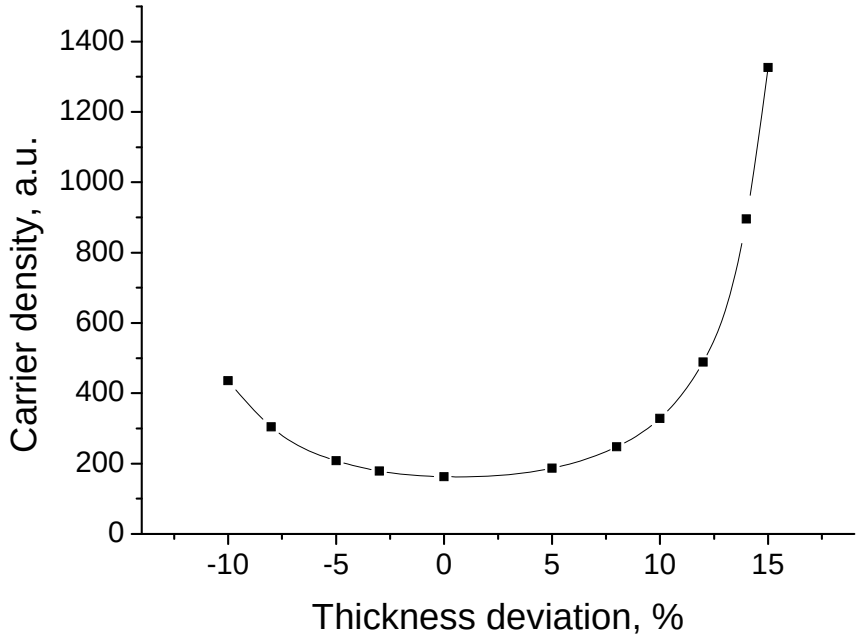

Fig. 3-22. Dependence of the carrier density at lasing threshold from the thickness deviation of the cavity. More than ±5 % difference the required carrier density increases dramatically.

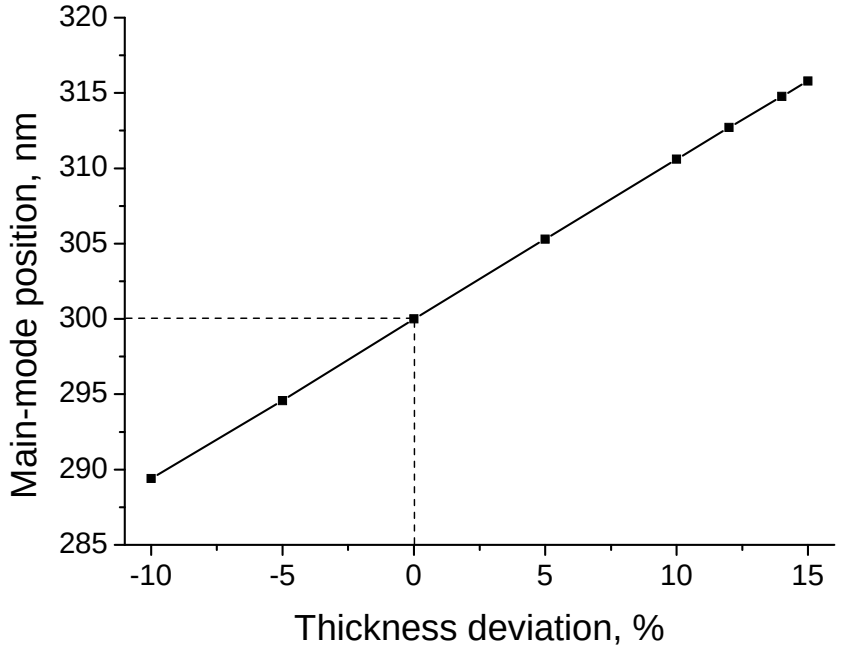

Fig. 3-23. Dependence of the position of the main-mode versus the thickness deviation of the cavity.

In Fig. 3-23 the dependence between the position of the main-mode and the thickness variation of the cavity is shown. The VCSEL structure is designed in such a way, that the transmission dip of the laser is at the maximum emission of the active material. In this case the maximum of the photo luminescence is at 300 nm and the FWHM of the emission curve is about 30 nm. By increasing the cavity thickness the dip moves to the right side of the stop-band and by a reduction of the cavity thickness the dip moves to left side. Each spectral deviation of the emission wavelength, to the left or to the right side from the maximum of the emission, results in a reduction of the gain. To be compensated the laser structure needs more pumping power in a detuned case.

In Fig. 3-24 the dependence of the distance between the left side-mode and the main-mode can be seen. The right side-mode is out of the emission spectrum of the active material.

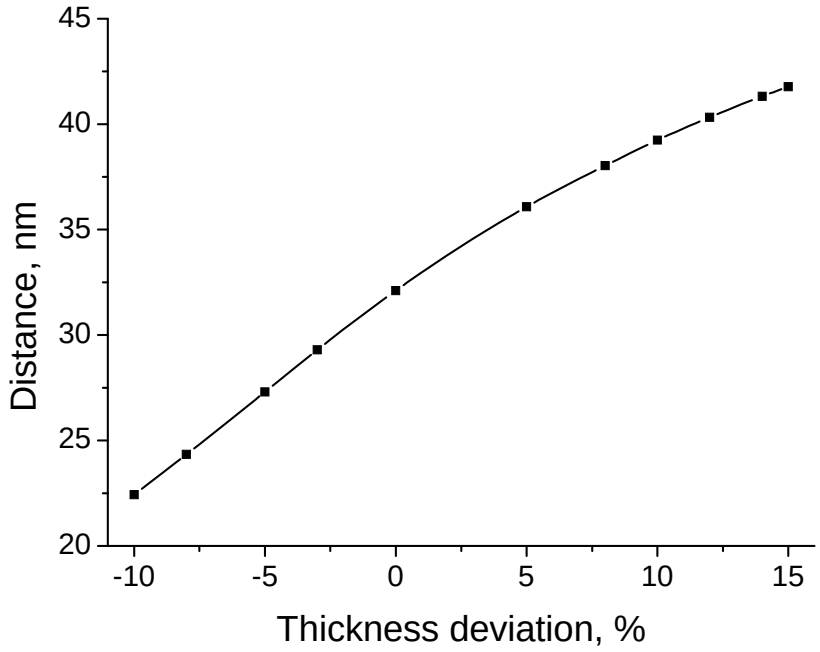

Fig. 3-24. Dependence of the distance between the left side-mode and the main mode versus deviation in the thickness of the cavity

3.4.1.2. Simulation of the error by deviation of the layer thicknesses from the DBR mirrors.

Another possible deposition error is the variation of the optical and the physical properties of the layers in the top and bottom DBRs. It is calculated and simulated the behavior of the laser properties by deviation of the thickness of one layer from the DBR mirrors.

For this simulations and analysis the thickness of the ZrO_2 layers for the both DBRs in the VCSEL structure from Table 4 was varied. The cavity thickness is kept constant at $k = 1$. The design wavelength was 300 nm and the range of the wave spectrum, in which the simulations were done, is chosen to be from 260 nm to 350 nm. The precision of the simulated and plotted data is selected in such a way to deliver high accuracy. For this reason the simulated range were divided in 10000 simulation points.

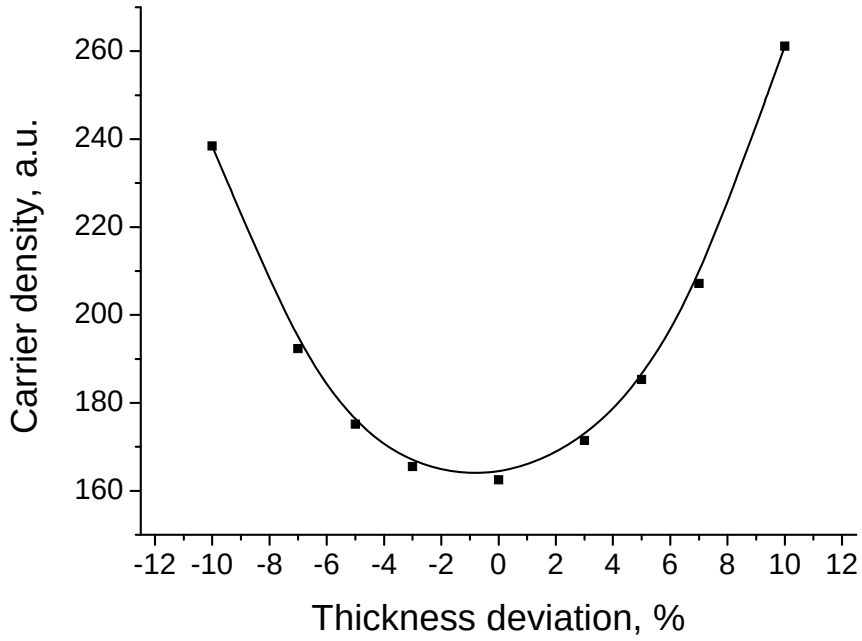

Fig. 3-25. Dependence of the carrier density at lasing threshold versus the thickness deviation in percents of ZrO_2 layers in the VCSEL structure from Table 4.

In Fig. 3-25 the necessary amount of carrier density at the lasing threshold versus the thickness deviation in percents of ZrO_2 layers is shown. Even a small

difference from the design thickness of the layers the required pumping power increases significantly. Furthermore, by deviations more than ±10 % a lasing threshold is not possible to be achieved.

As a result of this deviation the stop band of the structure moves to the right by increasing of the ZrO_2 layer thickness and to the left by decreasing of the layer thickness. In the same time a shift in the main-mode was observed. In Fig. 3-26 the dependence of the position of the main-mode versus the thickness variation in percents of ZrO_2 layers is shown. By deviation in the thickness with ±10 % the shift of the main-mode is about 5 nm.

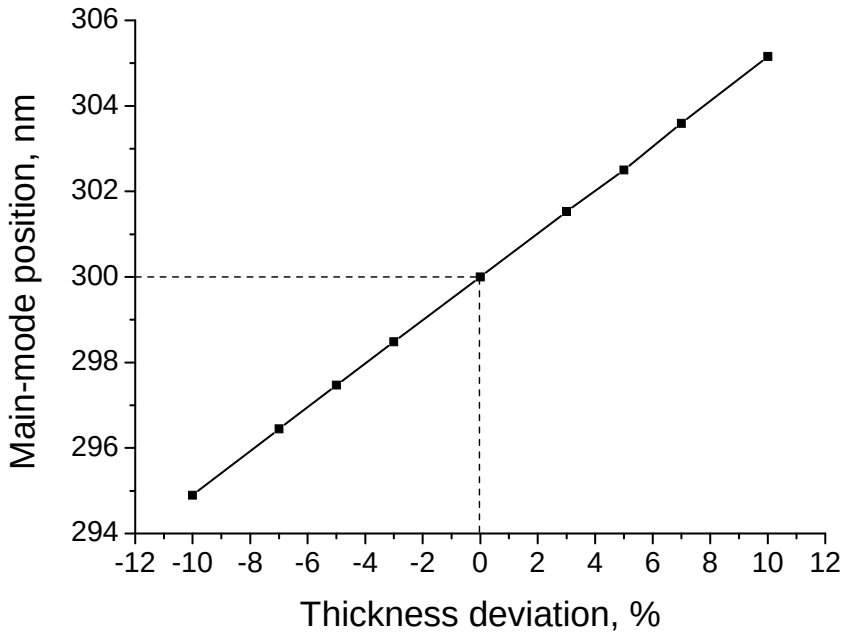

Fig. 3-26. Dependence of the position of the main-mode versus the thickness variation in percents of ZrO_2 layers in the VCSEL structure from Table 4.

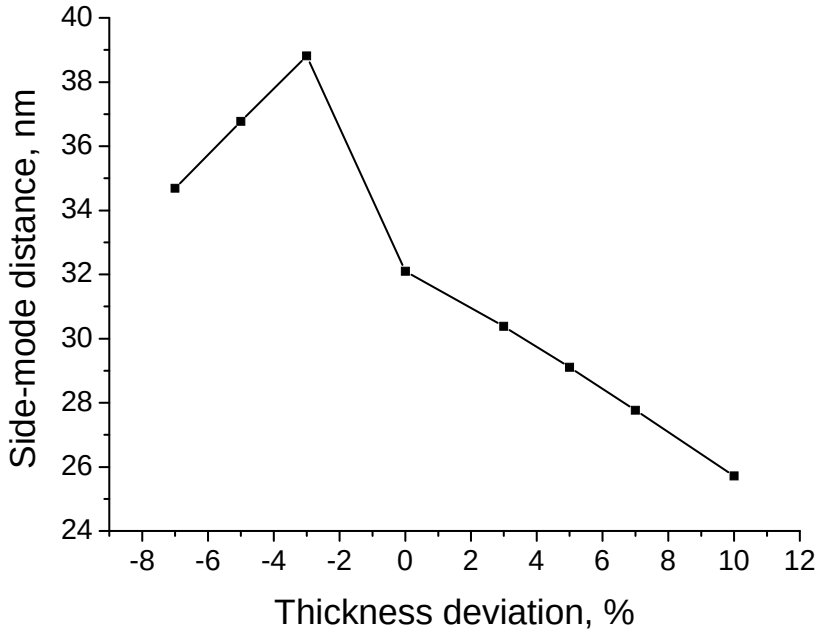

Fig. 3-27. Dependence of the distance of the side-mode versus the thickness variation in percents of ZrO_2 layers in the VCSEL structure from Table 4.

With shift of the stop-band to the left by decreasing of the layer thickness an additional side-mode from the left side appears in the stop-band. This side-mode is a result of the allowed wavelengths in the cavity. That's why the side-mode stays on position 262.02 nm in the stop-band. In Fig. 3-27 the dependence of the distance of the dominant side-mode versus the thickness variation of ZrO2 layers in the VCSEL structure from Table 4 is shown. At the beginning of the graph the side-mode distance is increasing and the main-mode drifts away from the cavity-side mode. By further increasing of the layer thickness in the DBRs the left side of the stop-band moves to the right and reach the cavity side-mode. At -3 % thickness deviation the left side of the stop-band coincides with the left side cavity-mode. The shift of the stop-band to the right is faster than the shift of the main-mode to the right from Fig. 3-26. As a result at -3 % thickness deviation the side-mode distance is decreasing.

The SMSR is decreasing rapidly. The right-shift of the main-mode, by increasing the layer thickness, forces it to escape from the maximum of the active material emission. Furthermore, the left side-mode of the stop-band moves to the right and get closer to the maximum of the emission. The side-mode intensity is increasing and the main-mode intensity is decreasing.

3.4.1.3. Simulation of the error by deviation of the absorption in the ZrO_2 layers in the DBRs

The absorption of the materials, which are part of the high reflective DBRs can reduce the optical properties of the VCSEL. The absorbed energy in the mirrors can increase the temperature of the structure and destroy the sensitive organic active material. In these simulations ZrO_2 with different values of the absorption is used.

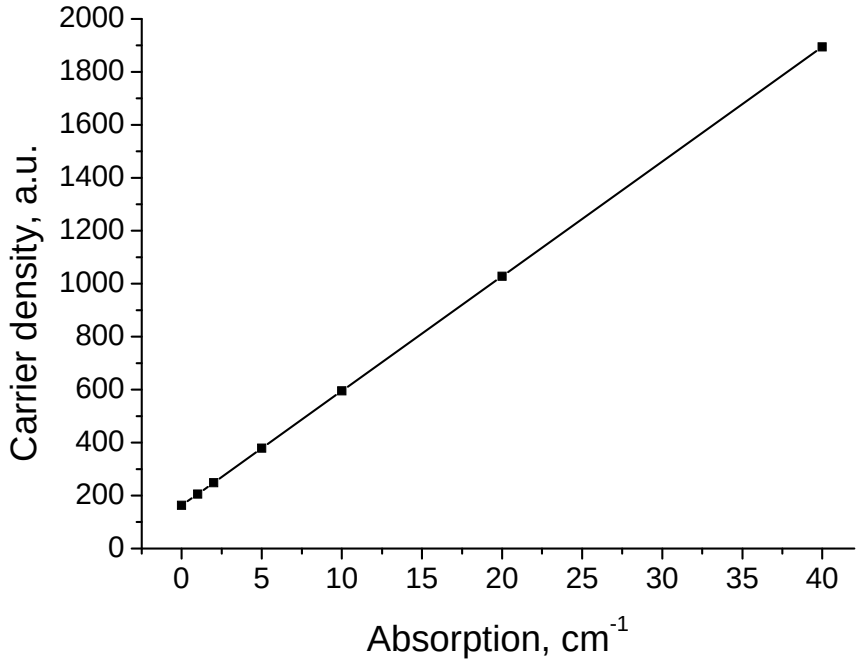

Fig. 3-28. Dependence of the required carrier density at lasing threshold versus the different absorption of ZrO_2 layer in the DBRs.

In Fig. 3-28 the dependence of the required carrier density at lasing threshold versus the different absorption of ZrO_2 layers in the DBRs is shown. The tendency is linear and even for a small absorption in the DBRs the losses are significant. With absorption 5 cm^{-1} the carrier density increases double and has value of 380 a.u. In Fig. 3-1 the dependence of the reflectivity of one DBR with different absorption is shown. Without any absorption the reflectivity of 14 periods DBR is 99,999 % and the same structure with 5 cm^{-1} absorption has reflectivity of 99,976 %.

Chapter 4

Deposition and optimization of the UV VCSEL devices

In this work the DBR structure is deposited by Plasma Enhanced Chemical Vapor Deposition (PECVD), Dual Ion Beam Sputtering (DIBS) process and by combination of both methods. The optical and physical properties of the layers and structures are measured with Ellipsometer and Reflectometer. A series of depositions of different materials are done and compared. By optimization of the process recipe only one parameter is varied at a time. The surface of the layers is measured and characterized by Atomic Force Microscope (AFM), Scanning Electron Microscope (SEM) and Whit-Light Interferometer (WLI). The materials deposited by PECVD show absorption in the UV range and bad optical properties. The sputtering method gave the possibility to deposit low absorptive materials suitable for UV VCSEL structures.

The active organic material is deposited in a dye evaporation machine in cooperation with the group of Prof. Salbeck (mmCmm, University of Kassel). The VCSEL structure is optically pumped by a nitrogen laser.

The optimization of the deposited materials and structures is done for the wavelength range from 300 nm to 500 nm. The range is chosen to cover the emission wavelength of the organic active material. For this range the organic materials developed so far show stable optical and mechanical properties.

4.1. Deposition and optimization of the active organic semiconductor materials

For the active medium utilized in the VCSEL structure organic semiconductor materials are used. The chemical synthesis, the deposition and the optimization of the organic materials are done at mmCmm. The deposition of the thin layers is performed by use of evaporation dye machine. In Table 4-1 are shown some organic materials used in this work as active medium in the VCSEL structures. All of them have high refractive index and the emission is in the blue and UV range. In Fig. 4-2 are shown the chemical formulas of the organic materials from Table 4-1.

Table 4-1. Organic materials used as active medium in the VCSEL structures.

Organic materials	**Emission wavelength, nm**	**Refractive index *n* at the emission wavelength**
Spiro-6ϕ	420	2.05
Spiro-Octopus-1	395	1.95
Spiro-3ϕ	380	1.90

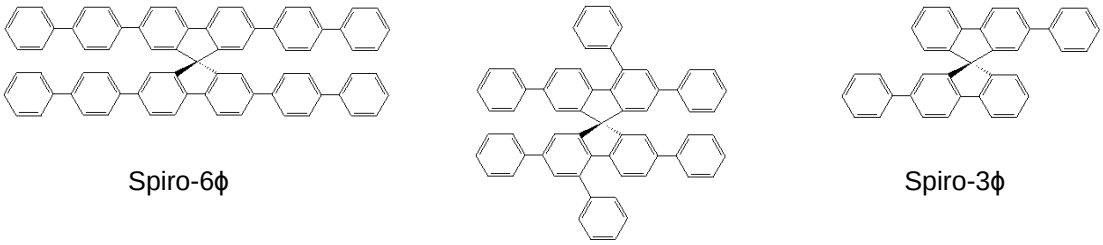

Spiro-6ϕ

Spiro-Octopus-1

Spiro-3ϕ

(a) (b) (c)

Fig. 4-1. Chemical formula of the organic materials used as active medium in the VCSEL structures. (a) Spiro-6ϕ, (b) Spiro-Octopus-1 and (c) Spiro-3ϕ

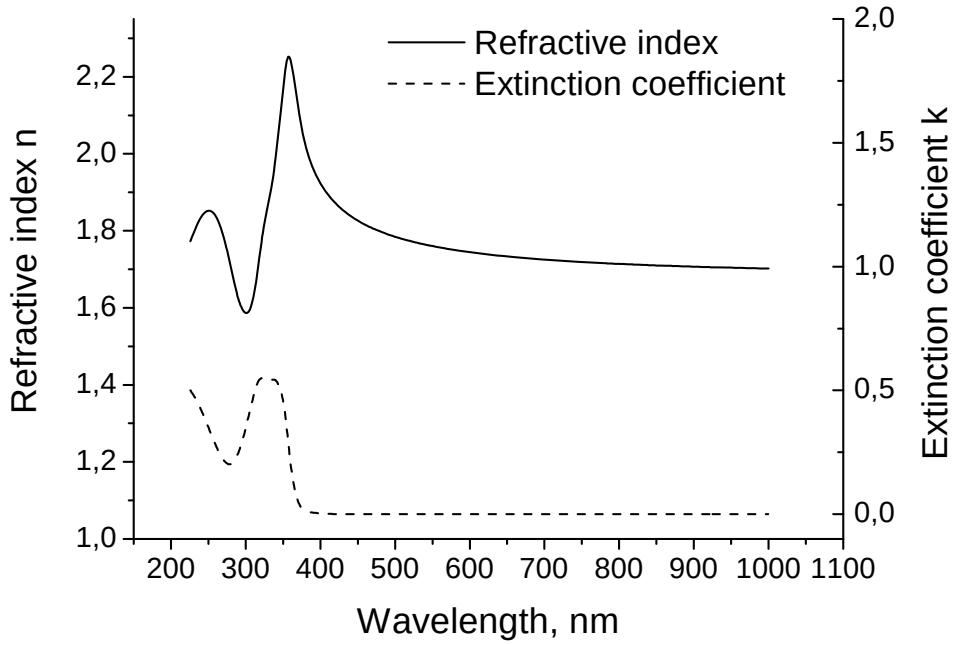

Fig. 4-2. Refractive index dispersion and the extinction coefficient of the organic active material Spiro-Octopus-1. The measurements have been performed at the mmCmm, University of Kassel from Dr. Spehr [122].

The refractive index dispersion *n* and the extinction coefficient *k* of the organic semiconductor material Spiro-Octopus-1 has been measured from Dr. Spehr in the department mmCmm and is shown in Fig. 4-2. The material is included in the sequence of the multilayer structure as high refractive index material with refractive index of n = 1,94. It has maximum absorption at 330 nm.

By optical pumping with nitrogen laser at 337 nm the material Spiro-Octopus-1 shows maximum radiation at 395 nm. In Fig. 4-3 the normalized intensity of the ASE spectrum of the organic material is shown. For the measurement of the ASE spectrum organic layer with thickness 111 nm is deposited on a glass substrate. The organic material is surrounded with low refractive index mediums and works like a wave guide. The structure is pumped perpendicular to the surface and the emission is measured from the side. The gain measurements have been performed at the TU Braunschweig with different pumping power and are shown in Fig. 4-4 [122]. The FWHM of the emission is 21 nm. By increasing the pumping power the gain increases and a small blue-shift of the maximum intensity of the emission can be seen.

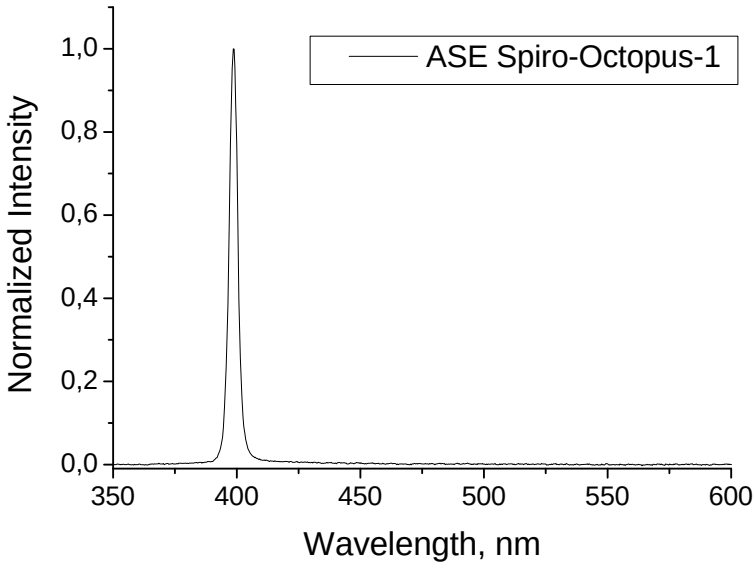

Fig. 4-3. Normalized intensity of the amplified spontaneous emission ASE (solid line) of the organic material Spiro-Octopus-1. The measurements have been performed at the mmCmm, University of Kassel from Dr. Spehr [122].

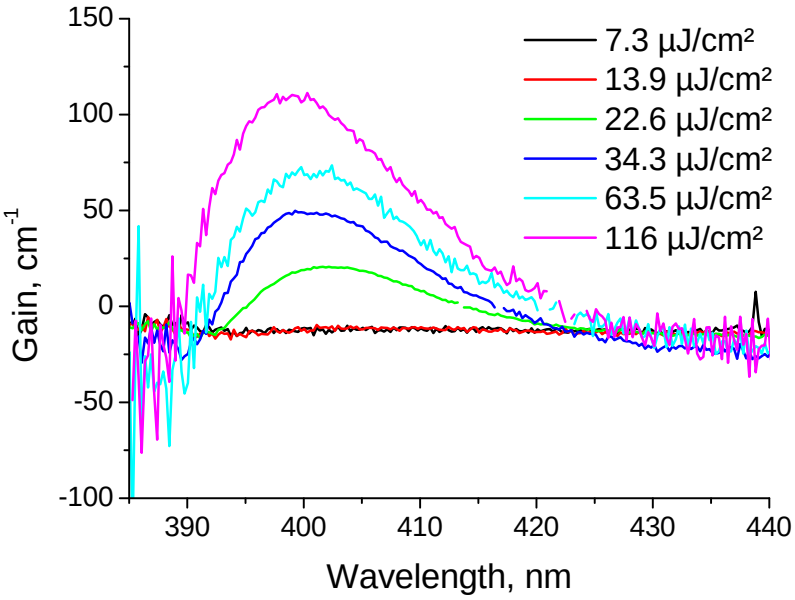

Fig. 4-4. Measured gain at different pumping power of the organic material Spiro-Octopus-1, The measurements have been performed at the TU Braunschweig [122] .

Another organic material used as an active media is Spiro-6ϕ. In Fig. 4-5 is shown its refractive index dispersion *n* and the extinction coefficient *k*, which has been measured from Dr. Spehr in the department mmCmm. The material has high refractive index and can be combined with low refractive index materials like SiO_2 and Al_2O_3.

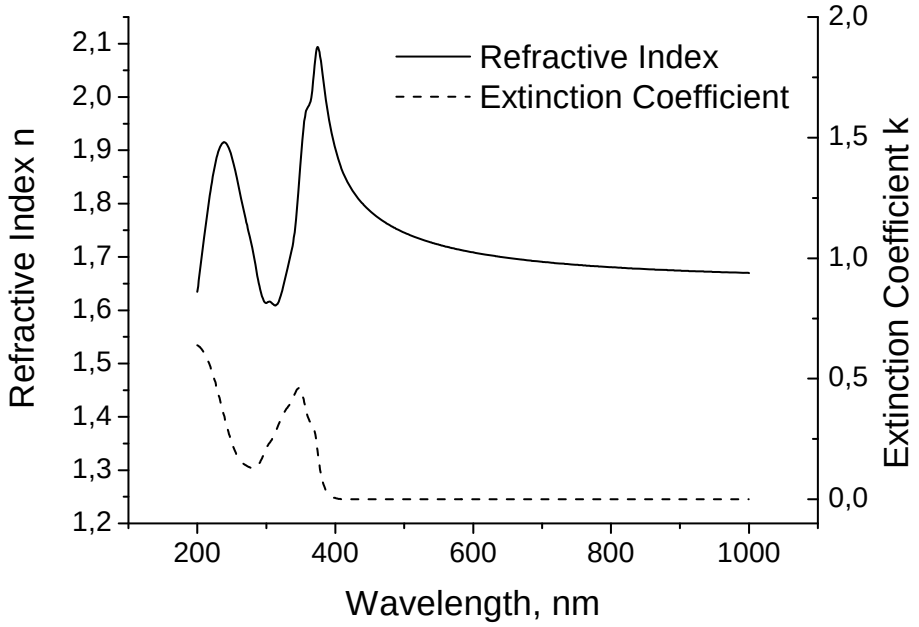

Fig. 4-5. Refractive index and extinction coefficient of the organic material Spiro-6ϕ. The measurements have been performed at the mmCmm, University of Kassel from Dr. Spehr [122].

The gain measurements of the organic material Spiro-6ϕ have been performed at the TU Braunschweig with different pumping power and are shown in Fig. 4-6 [122]. By optical pumping with energy from 0,367 µJ/cm^2 to149 µJ/cm^2 the material shows stable optical and mechanical properties. The maximum emission is at 420 nm wavelength. In Fig. 4-7 the normalized intensity of the ASE spectrum of the organic material is shown. The measurement procedure is similar to the ASE measurement of Spiro-Octopus-1.

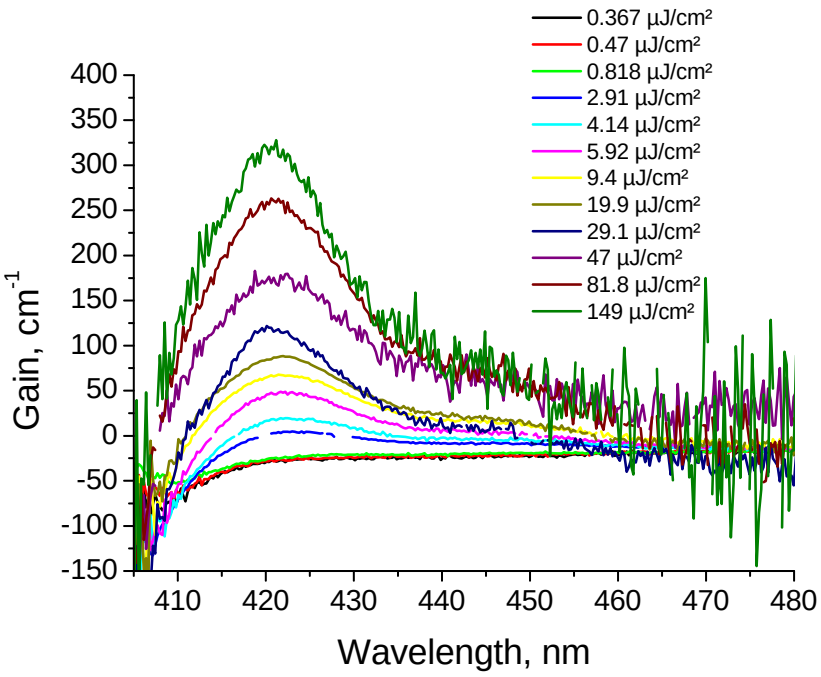

Fig. 4-6. Measured gain at different pumping energy of the organic material Spiro-6ϕ. The measurements have been performed at the TU Braunschweig [122].

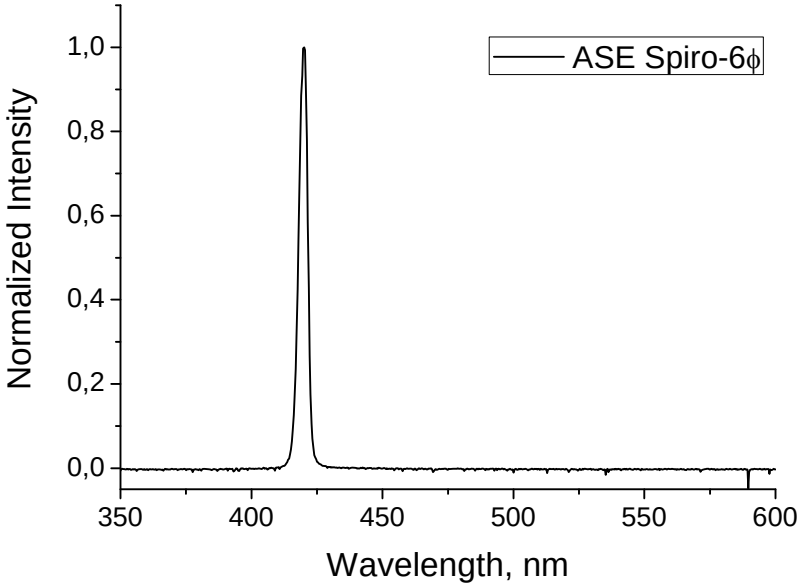

Fig. 4-7. Normalized intensity of the amplified spontaneous emission ASE (solid line) of the organic material Spiro-6ϕ. The measurements have been performed at the mmCmm, University of Kassel from Dr. Spehr [122].

4.2. Deposition and optimization of the dielectric materials and VCSEL structures

The deposition and the measurements are done under clean room conditions in Institute of Nanostructure Technologies and Analytics (INA). The material and structure optimizations prepared by DIBS machine is done in a clean room Class 1 and the PECVD depositions are carried out in a clear room Class 10000.

The reference design wavelength for the optimizations of the dielectrics materials is chosen to be 395 nm. At this wavelength the emission maxima of the organic active material Spiro-Octopus-1, used later for the VCSEL structure is located.

4.2.1. Dielectric materials and VCSEL structures deposited by PECVD

The PECVD is a widely used method for deposition of dielectric materials [113; 114]. The utilized machine is a Plasma Lab 80 plus of Oxford Instruments company. As a gas mixture for the deposition of the silicon nitride (Si_3N_4) is used a combination of 2% silane in nitrogen (SiH4 – N2) and ammonia (NH_3). For deposition of silicon dioxide (SiO_2) combination of 2% silane in nitrogen (SiH4 – N2) as silicon source and nitrous oxide (N_2O) as oxygen source is used. The deposition temperature can be varied from 60°C to 300°C.

Silicon nitride (Si_xN_y) and silicon oxide (SiO_x) layers are deposited at 120°C on Si substrate. The recipes are shown in Appendix A Table 1 and 2. The temperature is chosen to be below the glass transition temperature of the organic active materials used in this structure, which is 160°C. The thickness, the refractive index and the extinction coefficient were measured by Spectroscopic Ellipsometer (SE).

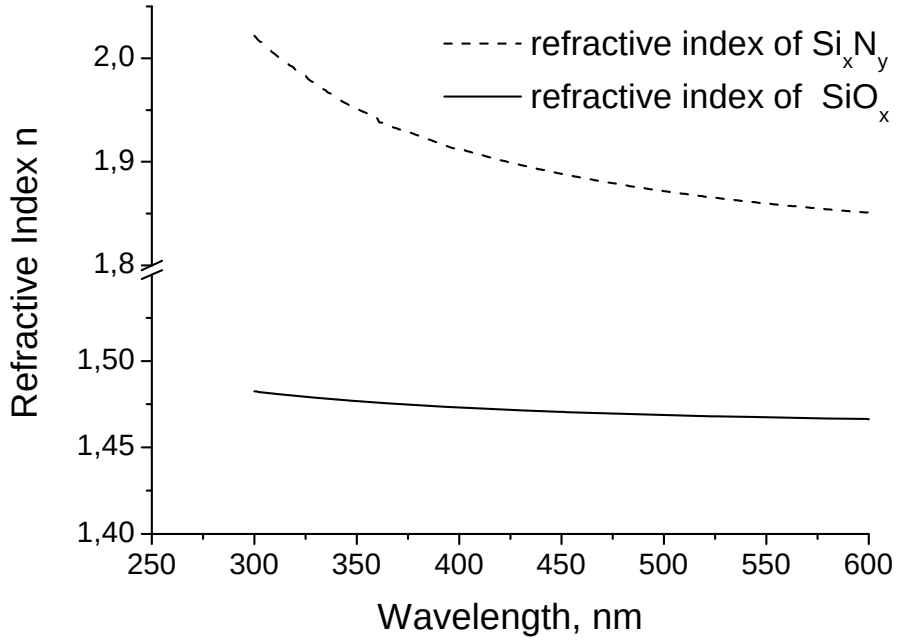

Fig. 4-8. Refractive index dispersion of silicon nitride (Si_xN_y) (dashed line) and silicon oxide (SiO_x) (solid line) deposited by PECVD.

In Fig. 4-8 the refractive index dispersion of the silicon oxide and the silicon nitride materials is shown. The Si_xN_y is used in the multilayer structure as high refractive index layer and in combination with SiO_x forms the DBR structure. The value of the refractive index at wavelength 395 nm for Si_xN_y is n = 1,91 and for the SiO_x is n = 1,47. This gives a refractive index contrast of $\Delta n = 0,44$. As was simulated before a high refractive index contrast requires less periods in the multilayer structure. In Fig. 4-9 the extinction coefficient of both materials is shown. The absorption edge of the silicon nitride starts at 403 nm wavelength: The material can be used for the mirror structures only for longer wavelengths. The measurements for silicon oxide layer do not show any absorption from 300 nm to 600 nm wavelength range.

The measured thicknesses of the layers are 154 nm for the silicon nitride and 74 nm for silicon oxide. The deposition rates are calculated to be 21,13 nm/min for Si_xN_y and 50,58 nm/min for the SiO_x.

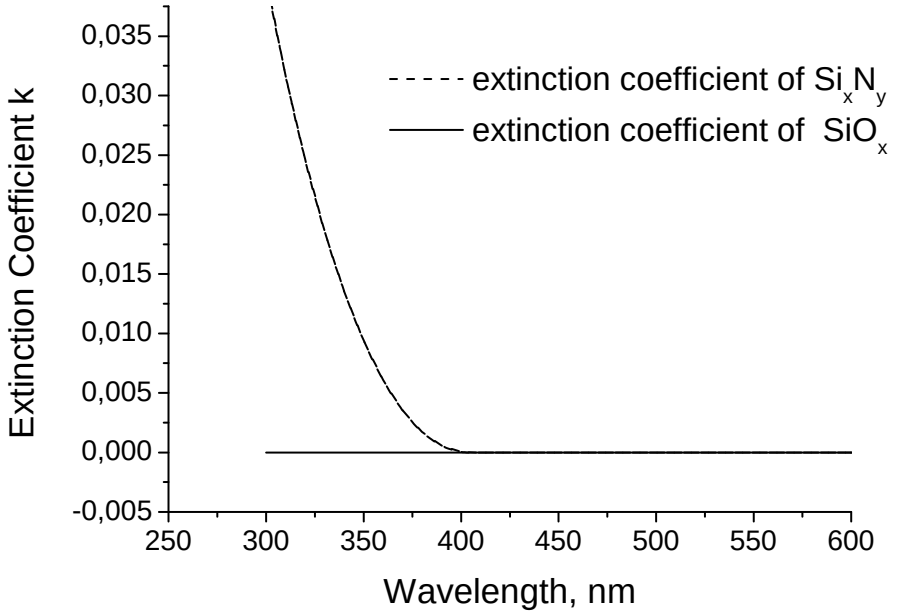

Fig. 4-9. Extinction coefficient of silicon nitride (Si_xN_y) (dashed line) and silicon oxide (SiO_x) (solid line) deposited by PECVD.

DBR mirrors are calculated and deposited for 395 nm design wavelength. Concerning the refractive index of the materials at the design wavelength the thickness of the layers is chosen to be quarter wavelength. This gives the thinnest layer, which covers the Bragg condition. Such a structure is compact and uses less material, which reduce the light scattering and the absorption caused by defects in the material. The deposition time is shorter and the possible deviation of the deposition parameters is smaller.

The reflectivity of three DBR mirrors with 10, 17 and 20 periods are deposited and compared. In Fig. 4-10 is shown that the reflectivity increases by increasing the number of the periods. The maximum reflectivity is measured for 20 periods DBR and has value of 96,3 %. A slope of the stop-band at the wavelengths below 400 nm appears. The reason is that the negligible defects in the deposited materials and the absorption measured for a single thin layer become more dominant in the thicker multilayer structures. The absorption of the materials in the mirror below 325 nm is very high and the DBR fringes in this region are almost deleted. Additionally the big surface roughness of the materials deposited by PECVD increase the scattering of the light and reduces the reflectivity of the mirror [115].

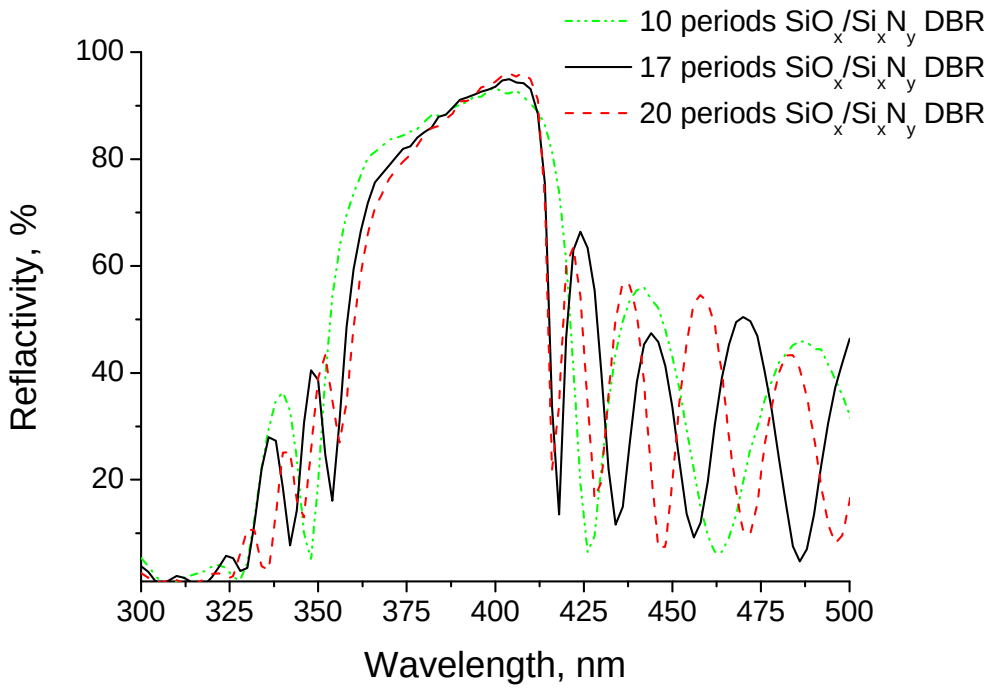

Fig. 4-10. Reflectivity of 10 (dot-dashed line), 17 (dashed line) and 20 (solid line) periods DBR mirrors are compared. A slope of the stop-band appears at the wavelength below 400 nm.

Other DBR with 17 periods and design wavelength at 386 nm is deposited and compared with the DBRs before. In Fig. 4-11 the reflectivity of the two 17 periods multilayer structures with design wavelength at 386 nm and 395 nm is shown. The stop-band of the mirror for 386 nm is shifted to the shorter wavelength with maximum of the DBR reflectivity R = 92,6 % located at 395 nm wavelength. Compared to the previous DBR with 17 periods (R = 94,9 %) the maximum reflectivity is reduced by 2,3 %. In the second DBR the same slope of the stop-band can be observed. For both DBRs the reflectivity at the design wavelength 395 nm is approximately the same and has value of about 93 %. As a conclusion, the shift of the stop-band to the shorter wavelengths didn't increase the reflectivity of the DBR mirror.

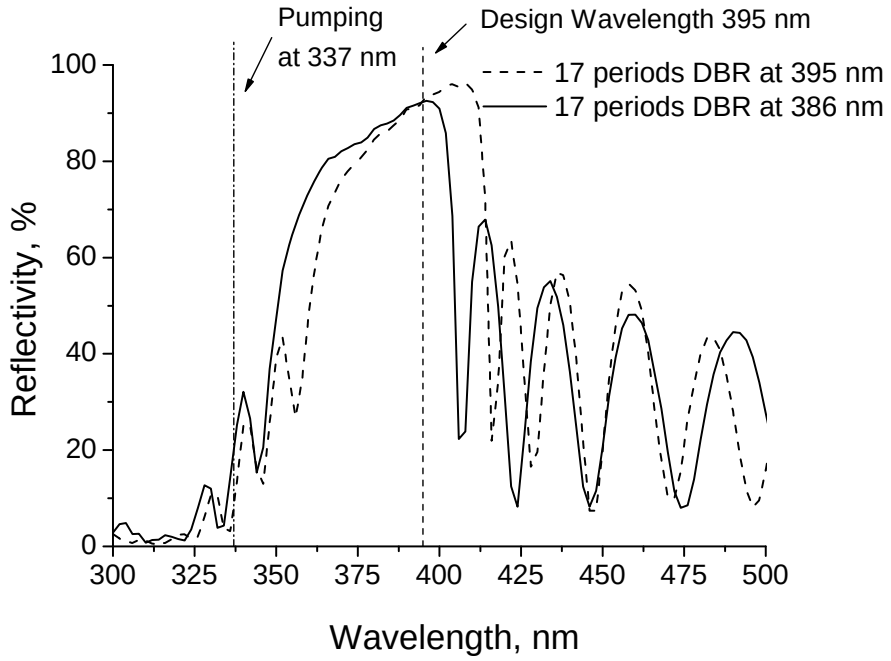

Fig. 4-11. Reflectivity of DBRs with design wavelength at 395 nm (dashed line) and 386 nm (solid line). The both DBRs show slope of the stop band.

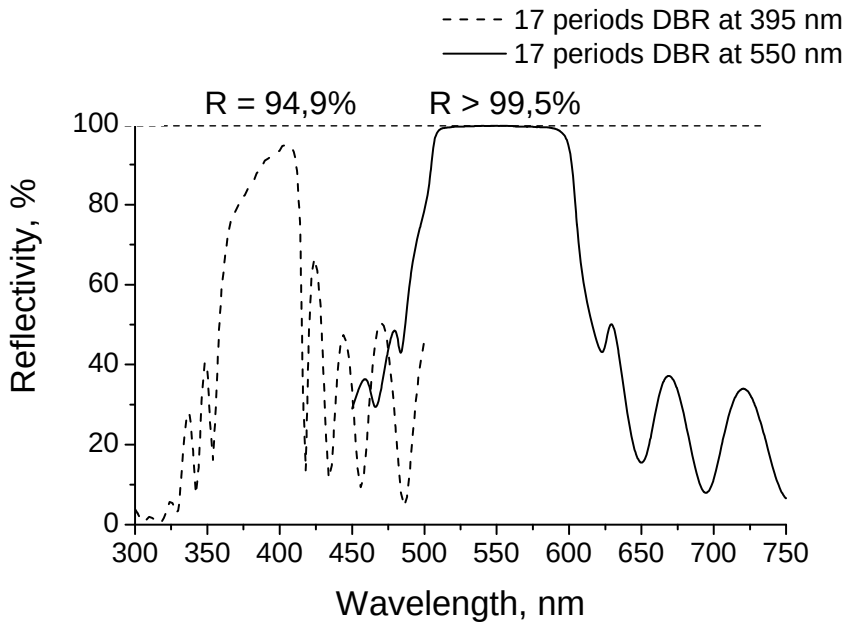

Fig. 4-12. Reflectivity of DBRs with design wavelength at 395 nm (dashed line) and in the visible range (solid line). The slope of the stop-band of the second DBR disappears and the reflectivity is increased.

In Fig. 4-12 the reflectivity of DBRs with design wavelengths in the UV range at 395 nm and in the visible range is shown. The slope of the stop-band for the DBR in the visible range disappears. The reflectivity is measured to be more than 99,5 %.

A VCSEL structure with design wavelength at 395 nm is deposited on silicon substrate. The laser structure is shown in Table 4-2. The bottom DBR consist of 17,5 periods SiO_x/Si_xN_y - SiO_x multilayer structure. As an active material an organic semiconductor material Spiro Octopus 1 is used. It is deposited in the cavity with thickness 2 λ. The deposition is done in mmCmm with an evaporation dye machine. The organic material is designed to be pumped optically at 337 nm and has a maximum emission at 395 nm. The semiconductor has high refractive index and contacts with low refractive index SiO_x layers. A top mirrot with 17 periods SiO_x/Si_xN_y DBR is deposited. The deposition temperature of the dielectric multilayer structure is 120°C, which is below the glass transition temperature of the organic material.

Table 4-2. VCSEL structure deposited by PECVD with design wave length at 395 nm.

17 periods top SiO_2/Si_3N_4 DBR
organic semiconductor material Spiro Octopus 1 d = 2 λ
17 and ½ periods bottom SiO_2/Si_3N_4- SiO_2 DBR
Si-wafer is used as a substrate

In Fig. 4-13 the reflectivity of the VCSEL structure from Table 4-2 is shown. Because of the cavity thickness of 2 λ several side-modes appear in the stop-band. The side-mode dips below 400 nm disappear because of the absorption in the organic and in the silicon nitride materials. At the design wavelength 395 nm a small dip of the main-mode can be seen.

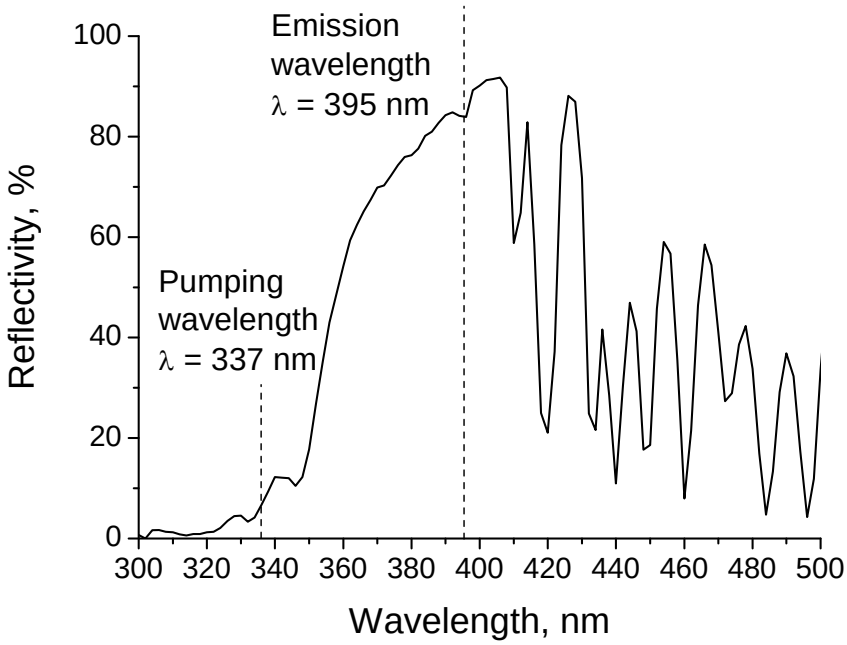

Fig. 4-13. Reflectivity of the VCSEL structure from Table 4-2. Several side-modes are appeared in the stop-band.

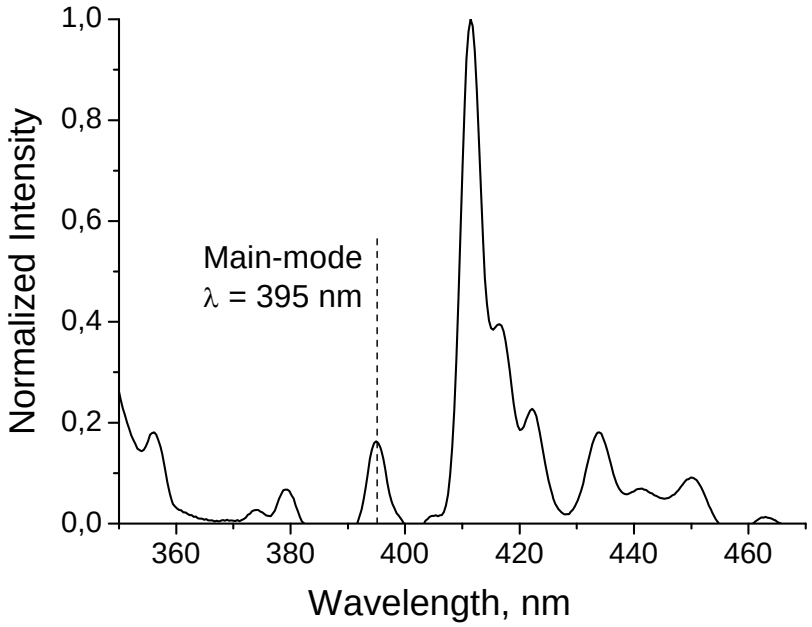

Fig. 4-14. Emission spectrum of the VCSEL structure from Table 4-2. The intensity of the main-mode is very low.

Fig. 4-14 shows the emission spectrum of the optically pumped VCSEL structure from Table 4-2. It can be seen that several side-modes appeared in the spectrum. The intensity of the main-mode is lower because of the absorption of the silicon nitride material in the mirrors.

The organic material is deposited with slight variation of the thickness along the 3 inch silicon wafer. This difference in the cavity thickness shows a small tuning of the emitted radiation. Fig. 4-15 shows the normalized emission spectrum of the VCSEL structure. The measurements are done on different positions on the substrate. A shift of the main-mode can be seen. By increasing of the cavity thickness the radiation peaks are shifted to the right. At the same time the intensity of the main-mode is increasing. This is a result of the absorption reduction of the silicon nitride material in the mirrors. At wavelength 380 nm a signal is measured, which is a result of the side-modes from the pumping nitrogen laser or measurement noise from the surrounding ambient.

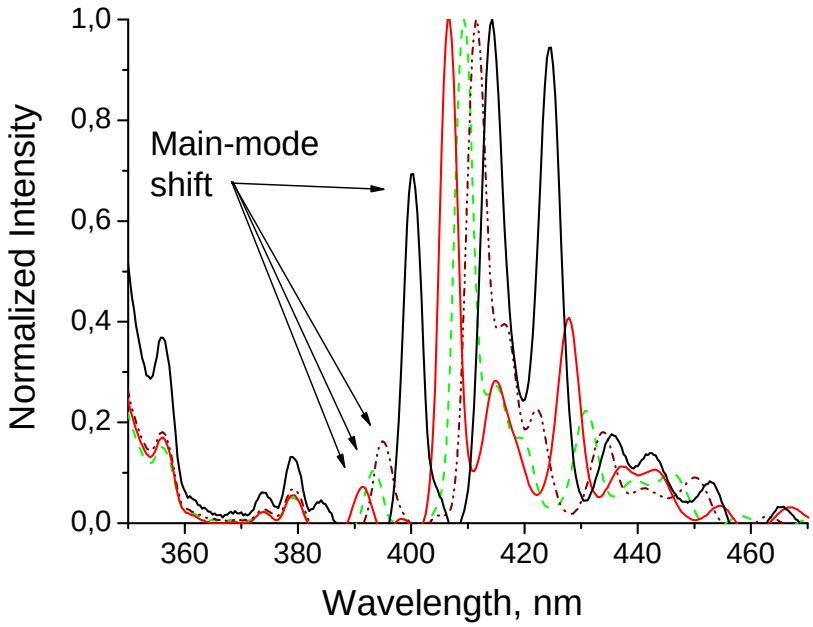

Fig. 4-15. Normalized emission spectrum of the VCSEL structure from Table 4-2 measured on different positions on the substrate.

The DBR mirrors, deposited by the PECVD machine, show high absorption in the wavelength range below 420 nm. This absorption reduces the optical properties of the VCSEL. The materials can be used for optical devices in the

visible (VIS) and infra-red (IR) spectrum [116]. For ultra violet (UV) spectrum another deposition method should be utilized. In this work dielectric materials are deposited and optimized by ion beam deposition machine.

4.2.2. Dielectric materials and VCSEL structures deposited by Dual Ion Beam Sputtering (DIBS) machine

The sputtering method is a very flexible and precise technique for deposition of thin layers. In this work dielectric materials and structures are deposited and optimized utilizing Dual Ion Beam Sputtering (DIBS) machine IonSys 1000 from Roth&Rau Company. The machine consist of deposition chamber, pump system, electrical rack with computer and ion source controllers, measurement set-up and operating gases (see Fig. 4-16).

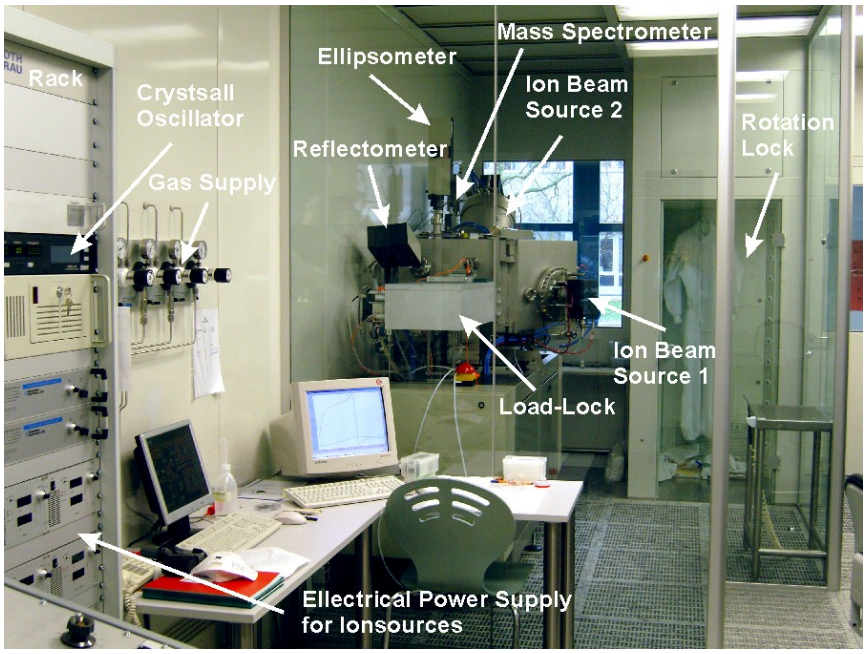

Fig. 4-16. Dual Ion Beam Sputtering (DIBS) machine IonSys 1000 in the clean room Class 1 (INA).

4.2.2.1. Overview of the Dual Ion Beam Sputtering (DIBS) machine and the measurement set-up

On Fig. 4-17 the schematic diagram of the main operating parts of the machine is shown. It is equipped with two RR-ISQ EC/I 125 ion electron cyclotron plasma sources. In the centre of the ion beam an energy from 100 eV to 2000 eV

and density of the ion current from 1 to 5 mA/cm^2 can be achieved. The first ion source is directed to the target system and is used for sputtering of the materials. The ion beam is extracted from the ion source by an ion optic system. It consists of three graphite grids with a radius of the curvature of R = 300 mm. The shape of the grids gives the possibility to focus or defocus the ion beam in a huge range. The ion source used for sputtering is designed to work with noble gases. In this machine Ar (Argon) and Xe (xenon) are connected.

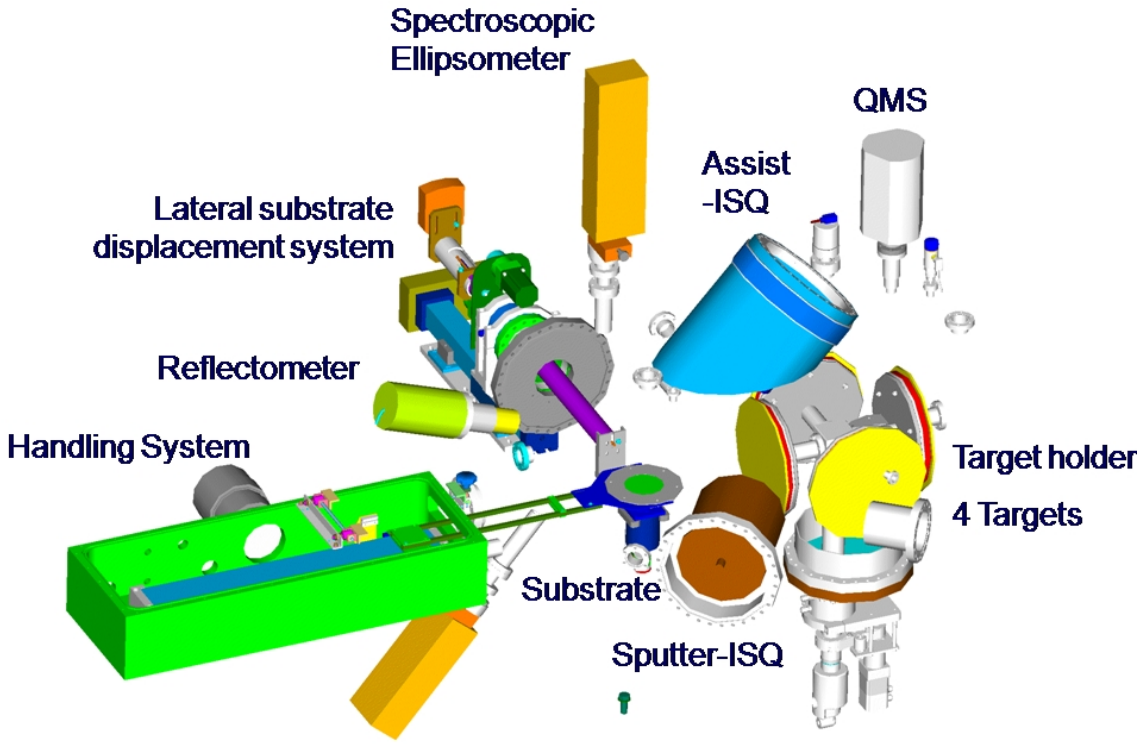

Fig. 4-17. Schematic diagram of DIBS machine IonSys 1000 from Roth&Rau Company. With kind permission of Roth&Rau Company.

The second ion source is so called assisted ion source. It is directed to the substrate and can be used for surface modification and substrate cleaning. The ion optic consists of three plane wolfram grids. The ion beam extracted from the ion source is very broad and homogeneous. This grid system is very convenient for etching processes. The assisted ion source is used for introduction of additional oxygen or nitrogen in the growth chamber. It can be used to control the oxidation or nitridation level of the sputtered metals. It is designed to work with noble gases as well. They are used mostly for etching, pre-cleaning and substrate

smoothing. To the assisted ion source in this machine are connected Ar (argon), O_2 (oxygen) and N_2 (nitrogen).

On the target holder four different materials can be fixed. The automatic positioning of the targets is used for deposition of multilayer structures. The huge diameter of the targets (D = 300 mm) can caver the sputtering ion beam and to prevents re-sputtering from the walls of the chamber.

The mechanism of the substrate holder is designed to position the sample in lateral direction from 0 to 260 mm and under tilt-angle from -80 to 90 degree. This gives the flexibility to deposit material from different places of the sputtered cloud, to deposit or etch the substrate under different tilt-angles. In this way the optical and the mechanical properties of the layers can be tuned in a wide range. The rotation of the substrate is used to increase the homogeneity of the layers and can be adjusted from 0 to 300 rpm. On the substrate holder samples with size up to 6 inch can be fixed.

The size of the deposition chamber is around 450 liters. It is equipped with a pump system, which consists of pre-pump, root-pump, turbo pump and cryogenic pump. The vacuum in the chamber in stand-by regime is around 2×10^{-8} mbar. To prevent humidity and particles from outside to enter into the chamber the substrate holder is loaded first in a separated load-lock. The pump system of the load-lock consists of root -pump and turbo-pump. It can reach vacuum around 10^{-7} mbar. An automatic lading system transports the substrate holder in the deposition chamber and fixes it on the substrate holder mechanism.

The equipment of the ion beam deposition machine and the process parameters are controlled by a compute. The control program with graphical user interface (GUI) is shown in Fig. 4-18. All the components and deposition parameters of the machine can be controlled either under “Manual” or under “Automatic” regime. The risky operations under “Manual” regime are restricted by user “log-in” and adequate rights. The deposition parameters and the process steps of multilayer structures can be given in a recipe and started in “Automatic” regime.

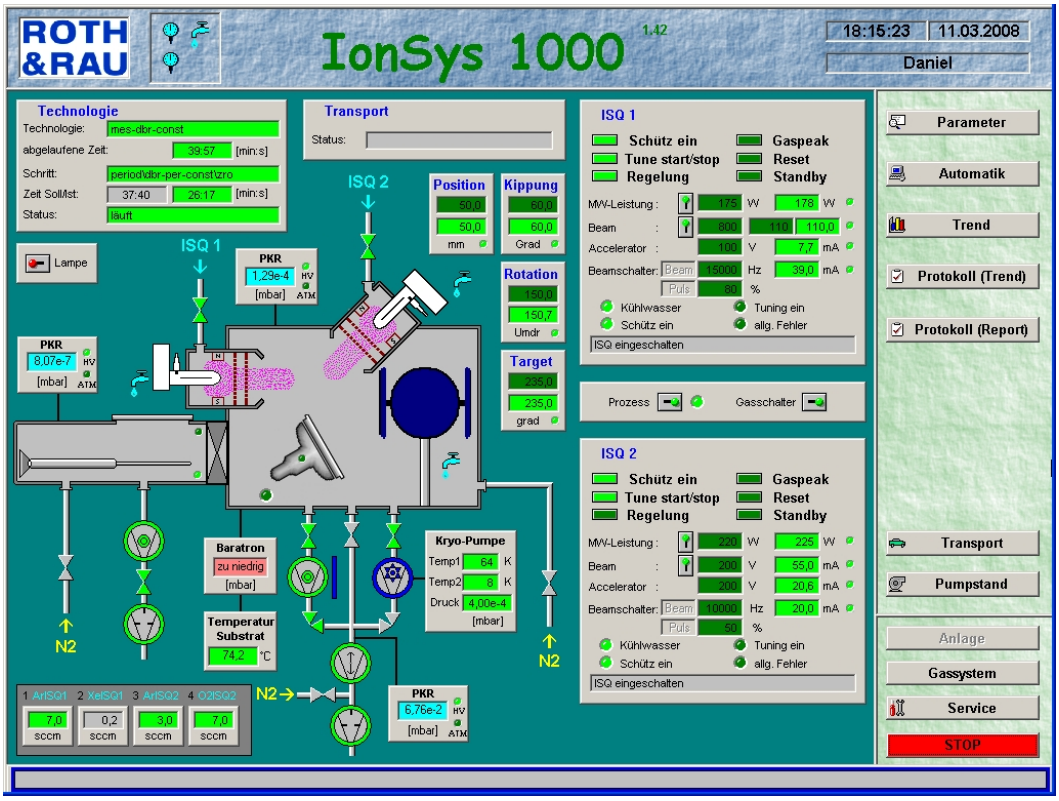

Fig. 4-18. Graphical user interface of the software controlling the ion beam deposition machine. With kind permission of Roth&Rau Company.

The DIBS machine is equipped with a spectroscopic ellipsometer and spectroscopic reflectometer measurement setup from “SENTECH Instruments GmbH” Company. The measurements can be carried out in the wavelength range from 350 nm to 1700 nm. The measurement apparatus are fixed on the deposition chamber under angle of 70 degree for the ellipsometer and under 90 degree for the reflectometer in respect to the substrate (see Fig. 4-19). The refractive index, the extinction coefficient and the layer thickness can be measured by using the ellipsometer. The reflectivity of single layers or multilayer structures can be measured by the reflectometer. All the measurement procedures can be done in-situ without taking out the substrate out of the chamber. Monitoring of the optical parameters and the layer thickness can be done on different stages of the structure deposition. The ellipsometer and reflectometer measurement setup is controlled by separate computers. The software “SpectraRay” is used for fitting and analyzing the measured date.

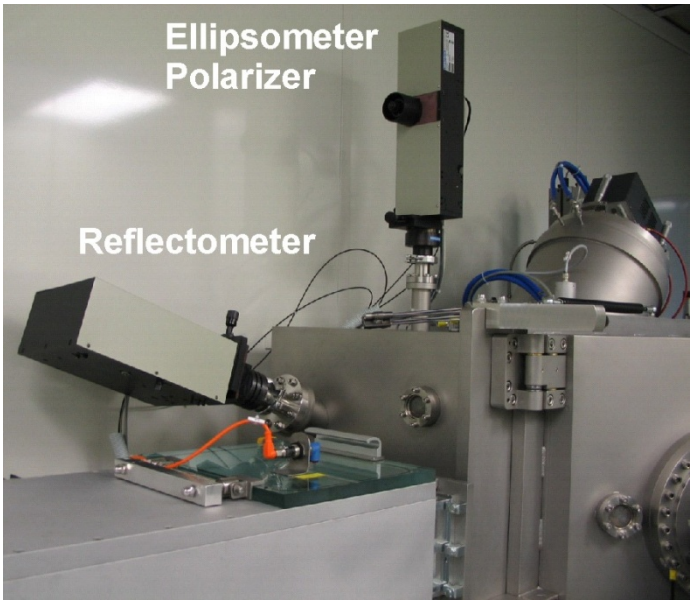

Fig. 4-19. The ellipsometer and the reflectometer are fixed on the deposition chamber.

To reduce the particle defects in the structure the depositions are done in clean room Class 1. Interface software connecting the computers of the DIBS machine and the measurement set-up is developed and test. The program is used to optimize the deposition of the multilayer structures.

4.2.2.2. Deposition and optimization of dielectric materials

In this chapter dielectric materials are deposited and optimized by dual ion beam sputtering (DIBS) machine. Two types of targets are used – ceramic and metal target. The layers deposited by sputtering of ceramic targets show low deposition rate. As a result the deposition time of the entire multilayer structure is very long. To increase the deposition rate and to reduce the deposition time metal targets are used. Additional oxygen introduced into the chamber is used for oxidation of the sputtered material. The optimization processes are performed by variation of the parameters like sputter energy, oxygen flow and assisted beam energy. With the optimized dielectric materials several high reflective DBR mirrors are deposited and measured.

The purity of the targets used in this work depends on the material and can vary from > 99,9 % for Zr (zirconium) to > 99,9999 % for a-Si (amorphous silicon).

Sputtering as deposition method works with charged particles. The process parameters depend on the conductivity of the sputtered materials. The metals can conduct the charge of the ions and neutralization of the beam is not necessary, whereas the ceramic targets are isolators and by sputtering with positive ions the sputtering surface is charged positive. This repels the ion beam and the sputtering yield is dramatically reduced.

The compound materials aluminum oxide (Al_2O_3) and yttrium oxide (Y_2O_3) have been sputtered. The process parameters are shown in Appendix 1 Table 3 The purity of the materials was > 99,95 % for Al2O3 and > 99,9 % for Y_2O_3 respectively. An argon (Ar) gas is used as an operating gas of the plasma and the extracted beam for sputtering. The targets are dielectric ceramic materials and their surface is neutralized by using pulse mode. In pulse mode the grid system of the ion source alternatively extract positive argon ions and neutralize them by extracting negative electrons from the plasma.

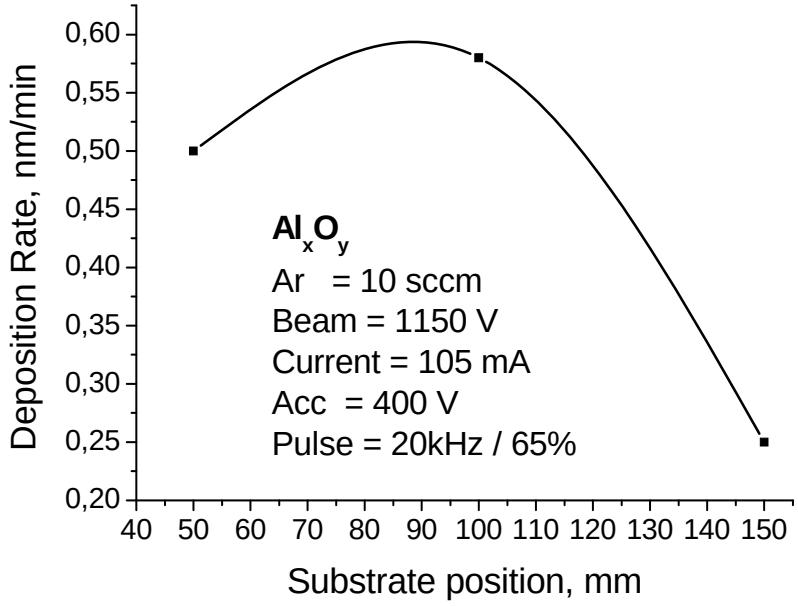

Fig. 4-20. Deposition rate of Al_xO_y material sputtered from compound ceramic target versus substrate position. The sputtering beam parameters are shown in the plot.

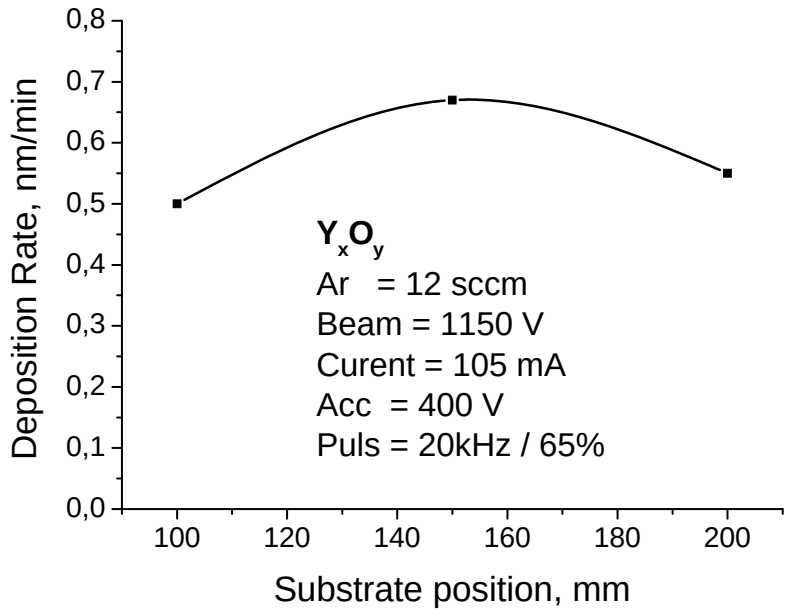

Fig. 4-21. Deposition rate of Y_xO_y material sputtered from compound ceramic target versus substrate position. The sputtering beam parameters are shown in the plot.

In Fig. 4-20 and Fig. 4-21 the dependence of the deposition rate of Al_xO_y and Y_xO_y materials from deposition position of the substrate (see Fig. 4-17) is shown. The bonding forces between the atoms of the ceramic materials are stronger compared to the metals. To break these bonds a high energy is required. The Al_xO_y and Y_xO_y materials are sputtered with energy of the beam 1150 eV. Even with such a high energy the maximum deposition rate of Al_xO_y is less than 0,6 nm/min and for Y_xO_y is less than 0,7 nm/min. From the shape of the graphic for the deposition rate the distribution of the sputtered cloud can be seen. It depends on the sputtered material, the energy of the ion beam and the angle between the target and the beam. For Al_xO_y the maximum deposition rate is obtained at position 100 mm and for Y_xO_y the maximum deposition rate is at position 150 mm. The deposition rate for Y_xO_y is 0,1 nm higher than Al_xO_y because the used argon flow for the plasma is 2 sccm higher. The amount of the argon gas introduced into the ion source is defined by the process parameters for stable plasma.

The calculated required time with this deposition rate for deposition of one VCSEL structure is about 70 hours. During this long deposition time the probability for deviation of the process parameters is bigger. As a sequence a drift in the multilayer structure can be observed. From economical point of view the long sputtering process is time consuming and the price of the device will be very high.

From other side very short deposition time can reduce the thickness accuracy of the deposited layers. The different materials in the multilayer structure are deposited by different recipe parameters. At every change of the process parameters lick gas flow and sputtering energy the deposition conditions are changed. The machine needs time to stabilize the parameters like target and substrate temperature. In the next experiments the optimum deposition rate and optical parameters are investigated.

The atomic bonds of metals are not as strong as in the ceramic materials. This leads to higher sputtering yield of the metal targets. In this work aluminum (Al), silicon (Si) and zirconium (Zr) materials are sputtered. With additional oxygen or nitrogen introduced into the chamber dielectric materials are deposited. The processes are optimized for deposition of materials with high refractive index contrast and low absorption.

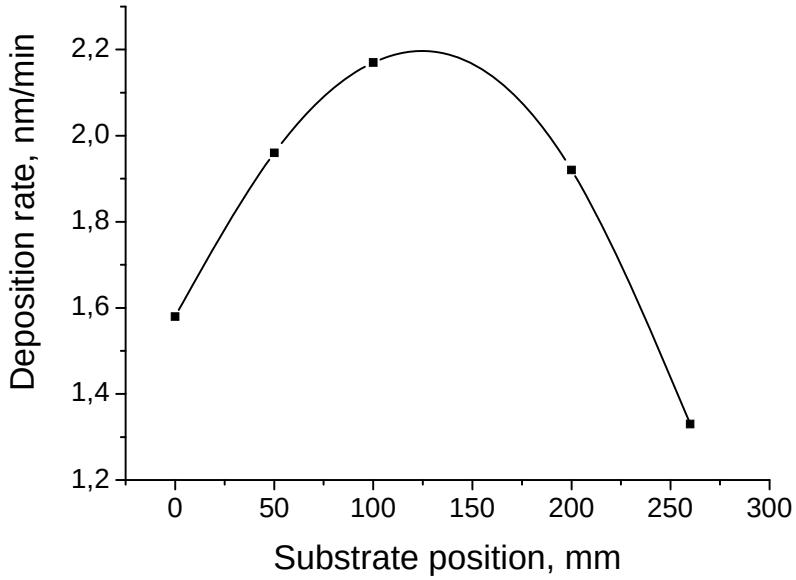

Fig. 4-22. Deposition rate of pure silicon material versus the lateral position of the substrate.

A silicon (Si) target with purity 99,9999 % is sputtered with beam energy of 500 eV. In Fig. 4-22 the deposition rate of pure silicon material in different lateral position of the substrate is shown. The depositions are performed on structured silicon substrate with photo resist AZ1518 by using optical lithography. By removing the photo resist with acetone by lift-off technique a step in the deposited material is formed. The high of the step represents the thickness of the deposited

material. By utilizing white light interferometer (WLI) the profile is measured. The maximum of the deposition rate is calculated to be at substrate position 100 mm. The shape of the graphic shows the distribution of the sputtered cloud.

Additional molecular or ionized oxygen is introduced into the chamber. The oxygen gas reacts with the sputtered silicon material and the dielectric material product is deposited on the silicon substrate as silicon dioxide thin film (SiO_2). In Fig. 4-23 the dependence of the deposition rate from the oxygen flow is shown. The thickness and the optical parameters are measured in-situ by spectroscopic ellipsomtry. It can be seen that the deposition rate is higher than the deposition rate of sputtered ceramic Al_2O_3 and Y_2O_3 targets (see Fig. 4-20 and Fig. 4-21). By increasing the gas flow the deposition rate decreases. The ionized oxygen is more reactive than the molecular oxygen and the required ionized oxygen flow for full oxidation of the sputtered silicon is lower. As a result the pressure in the chamber for the process with lower ionized oxygen flow is lower and the deposition rate is bigger.

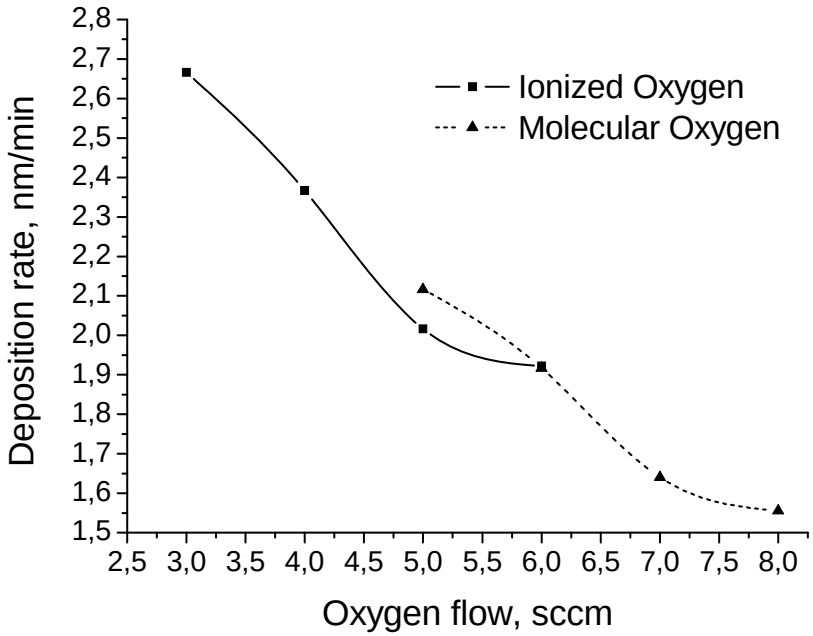

Fig. 4-23. Deposition rate of SiO_x material versus molecular (dotted line) or ionized (solid line) oxygen flow. The thickness and the optical parameters are measured by spectroscopic ellipsomtry.

The process parameters for deposition of silicon dioxide with molecular oxygen are shown in Appendix A, Table 5-6. In Appendix A. Table 5-7 the recipe

for deposition of silicon dioxide with ionized oxygen is shown. The oxygen is ionized by ignition of the plasma in the second assisted ion source. For the ignition of the oxygen plasma a power of the microwave generator 300 W is used and after stabilizing the process parameters is set to be 250 W.

The reflectivity of the DBR mirror depends very much on the refractive index contrast between the two materials and the absorption of the layers. To reduce the absorption and to achieve material with low refractive index the oxygen flow and the energy of the oxygen molecules are varied.

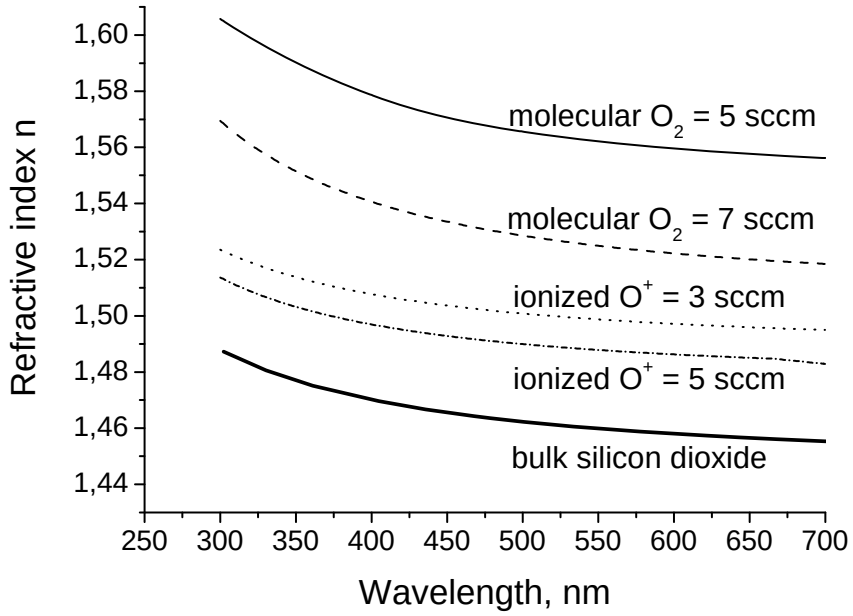

Fig. 4-24. Refractive index dispersion of SiO_x material with molecular and ionized oxygen with different gas flow

In Fig. 4-24 the refractive index dispersion of silicon dioxide materials deposited with molecular and ionized oxygen with different gas flow are compared. From the graphic it can be concluded that the refractive index of SiO_x deposited with 5 sccm molecular oxygen is higher than the refractive index of SiO_x deposited with 5 sccm ionized oxygen. The oxidation level of the sputtered silicon increases by increasing the oxygen flow and by changing the energy of the reactive gas from molecular to ionized molecules.

In Fig. 4-25 the dispersion of the extinction coefficient of the deposited silicon dioxide materials for different oxygen gas flow and for not ionized and ionized

molecules is shown. By increasing the oxygen flow the absorption of the silicon oxide material is decreasing and the absorption edge is shifted to the lower wavelength. In case of ionized oxygen with gas flow 5 sccm the absorption is zero in the wavelength range above 300 nm.

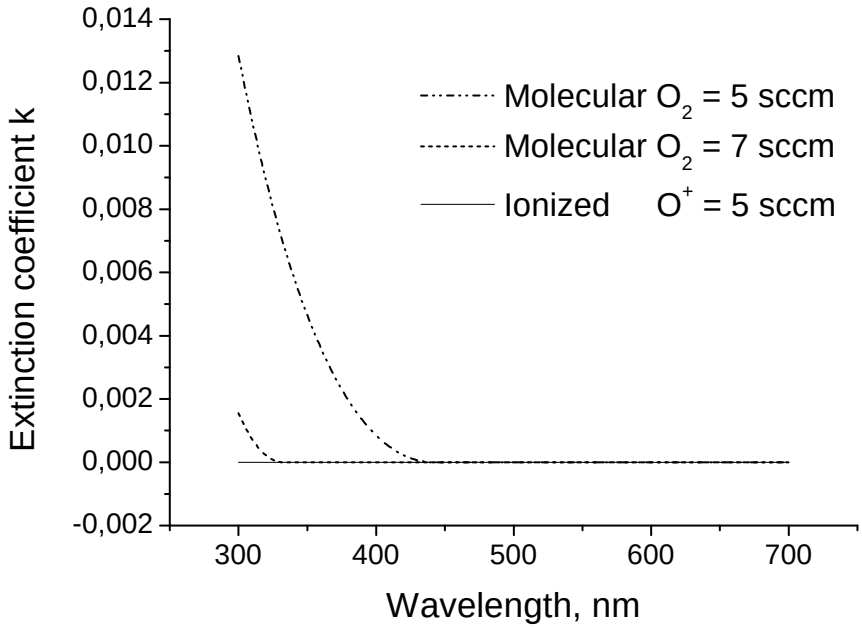

Fig. 4-25. Dependence of the extinction coefficient dispersion from the oxygen reactivity (molecular or ionized) and gas flow.

The silicon dioxide material has a refractive index of n = 1,5 at a wavelength of 395 nm (at this wavelength the active material Spiro-octopus-1 has maximum emission). In the multilayer VCSEL structure the material can be used as low refractive index material. In general the sputtering method is a high energetic technique and the atom structure of the deposited material very compact. The sputtered materials are optically denser than the materials deposited by PECVD. This explains the higher refractive index of the sputtered silicon dioxide compared to the literature value of the bulk silicon dioxide (see Fig. 4-24). By optimizing the process for deposition of the oxide material the difference in the refractive indices is reduced to 0,04.

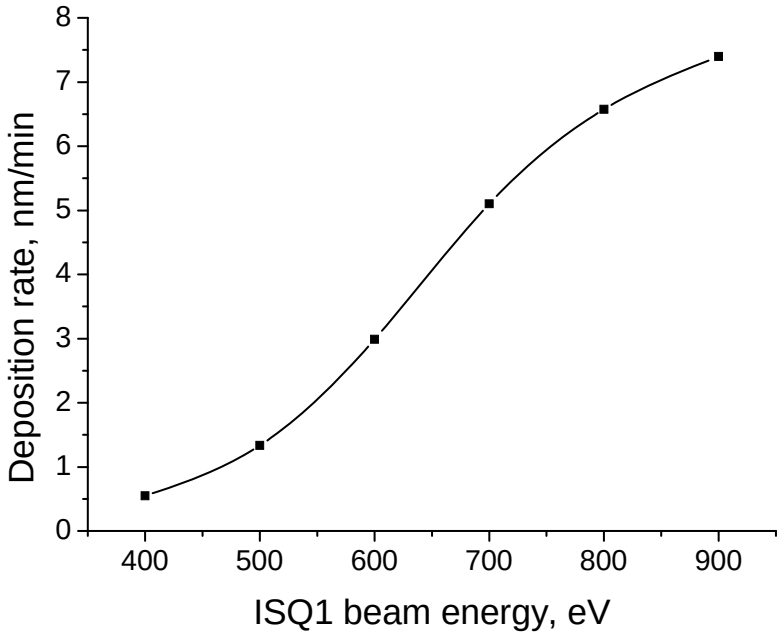

Fig. 4-26. Deposition rate of silicon dioxide material versus the energy of the sputtering beam from ISQ1.

The deposition rate of the silicon dioxide material from Fig. 4-23 is still very low. Calculations show that the thickness of the silicon dioxide layer for a multilayer structure with 395 nm design wavelength is 65,8 nm. The deposition time of this layer with a deposition rate of 2,3 nm/min is 29 min. Thus the time only for deposition of the silicon dioxide layers in the complete VCSEL structure with 30 periods is 870 min (14,5 hours). It is obvious that the deposition rate is still very low and the recipe should be optimized for high deposition rate. This can be done by increasing the amount of the sputtered material from the target. The most important parameter for this is the energy of the sputtering beam, which is extracted from the first ion source (ISQ1). In Fig. 4-26 the dependence of the deposition rate of silicon dioxide material from the energy of the sputtering beam is shown. With 400 eV the deposition rate is only 0,52 nm/min and by increasing the sputtering energy up to 900 eV the deposition rate becomes 7,4 nm/min. So the deposition time for one layer is only 8 min and 54 sec and for the same VCSEL structure with 30 periods the time is reduced to 267 min (4,45 hours).

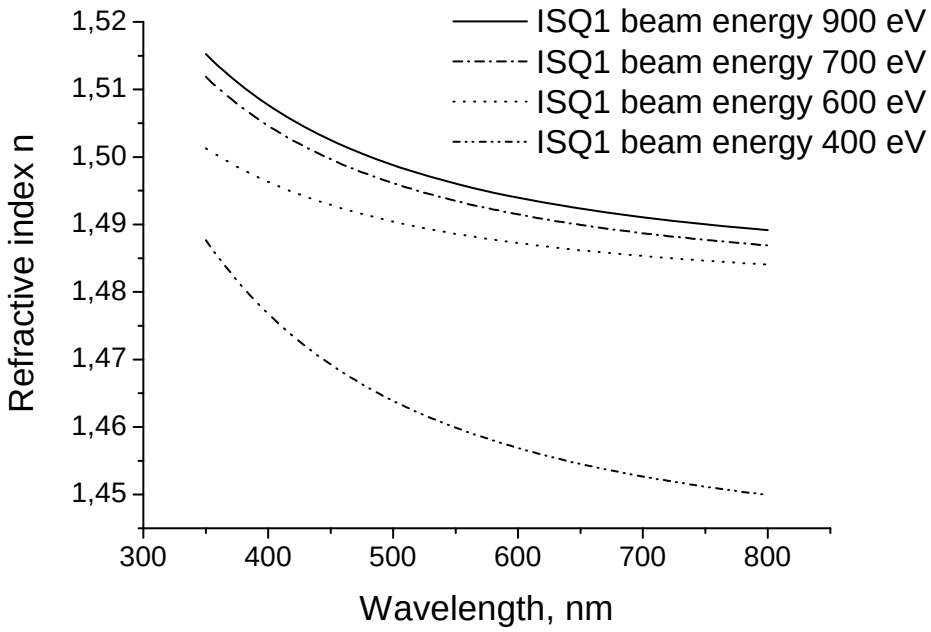

Fig. 4-27. Refractive index dispersion of silicon dioxide material with sputtered with different energies of the argon beam.

In Fig. 4-27 is shown that the silicon dioxide material sputtered with higher energy has higher refractive index dispersion. The deposition rate is very high and the oxygen introduced into the chamber is not sufficient to fully oxidize the sputtered silicon material. Therefore the refractive index at 395 nm for sputtering energy 900 eV is n = 1,51. With low sputtering energy the deposition rate is lower and the oxygen gas reacts longer with the silicon material. The result is fully oxidation of the silicon and the refractive index at 395 nm for sputtering energy 400 eV is n = 1,48.

The oxidation level of the sputtered silicon material and the deposition rate of the deposited silicon dioxide depend on the energy of the oxygen introduced into the chamber. In Fig. 4-28 the dependence of the deposition rate of silicon dioxide from the oxygen energy is shown. With the same energy of the sputtering beam (800 eV) and with the same oxygen flow (16 sccm) the process with molecular oxygen has the lowest deposition rate.

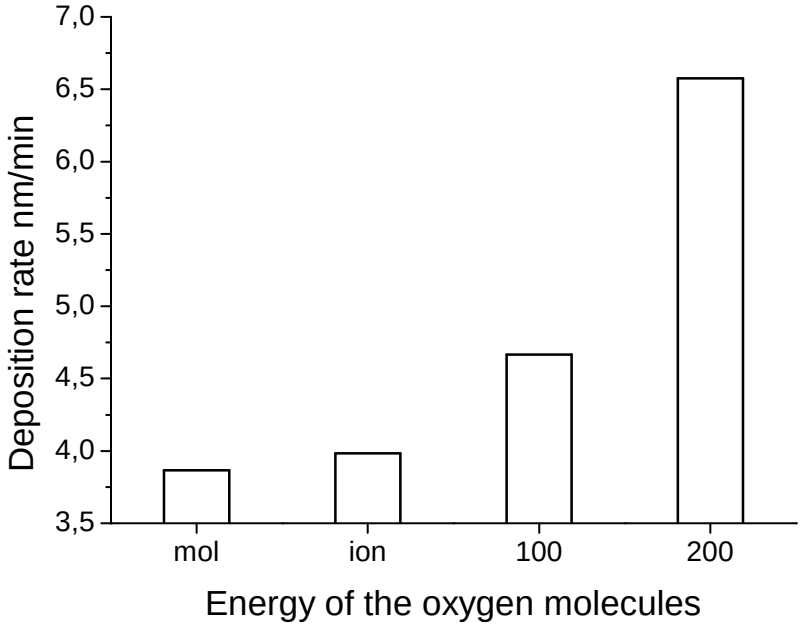

Fig. 4-28. Deposition rate of the silicon dioxide versus the energy of the oxygen introduced into the chamber. (with: mol – molecular oxygen, ion – ionized oxygen, 100 – 100 eV assisted beam with oxygen and 200 – 200 eV assisted beam with oxygen).

The oxygen ionized is by ignition of oxygen plasma from the second assisted ion source (ISQ2). In this case the ionized oxygen molecules are more reactive and can be easily bound with the silicon atoms. By extracting of the oxygen beam from the ion source and by directing it to the substrate, additional momentum energy of the oxygen molecules can be added. In this case the oxidation takes place not only in the chamber but also at the surface of the sample. The sputtered silicon clusters are partially oxidized in the chamber and can be deposited on the substrate surface. This can cause an absorption in the layer. The oxygen beam is used to destroy the clusters and ensure the full oxidation of the silicon atoms. At the same time the deposition rate increases. So with 200 eV energy of the oxygen beam from the assisted ion source (ISQ2) a deposition rate of 6,7 nm/min is reached.

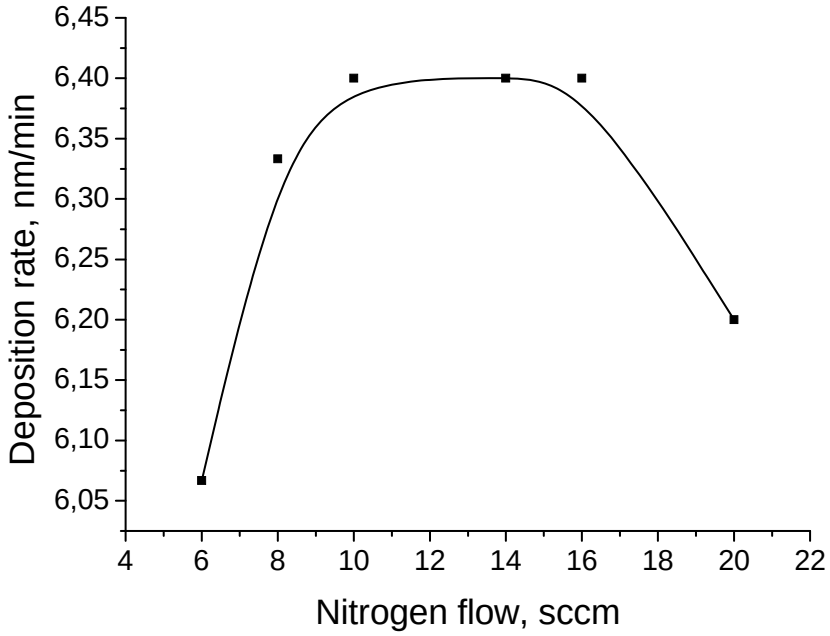

Fig. 4-29. Dependence of the deposition rate of silicon nitride (Si_3N_4) rate from the nitrogen flow into the chamber.

By utilizing the experience for sputtering processes and deposition of oxide materials, collected during the optimization of the silicon dioxide, other dielectric materials are deposited and investigated.

Silicon nitride (Si_3N_4) is deposited by introducing nitrogen into the chamber and sputtering of a pure silicon target. Molecular nitrogen is a low reactive gas. To increase the reactivity the depositions are carried out with an ionized nitrogen beam with energy of 200 eV. For sputtering of the silicon material an argon beam with energy of 800 eV is used.

In Fig. 4-29 the deposition rate of the silicon nitride from the nitrogen flow is shown. At the beginning the deposition rate increases by increasing the gas flow. Nitrogen gas participates in the nitridation of the silicon material. At 10 sccm nitrogen flow, the saturation level is reached and the deposition rate is constant. By a nitrogen flow higher than 16 sccm, an over-nitridation is achieved. In this case two sputtering phenomena take place. By a high nitrogen flow the target surface is nitrifide. In this way the ion beam should sputtered first the silicon nitride film from the surface of the material. The nitrides have stronger bonds compared to the bonds in the silicon material. To compensate this, a sputtering beam with higher energy should be used. By a high nitrogen flow the pressure into the

chamber is higher and the sputtered material collides with more particles. The material reaching and depositing the substrate is less.

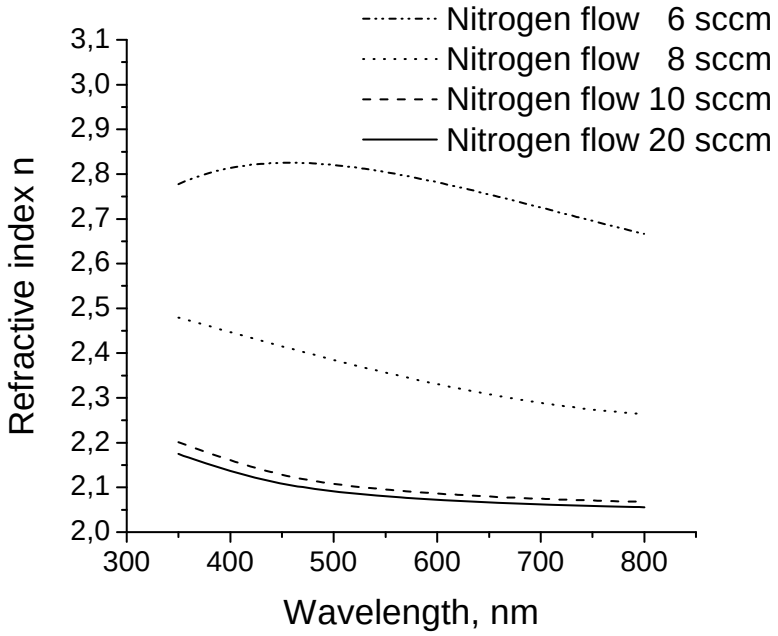

Fig. 4-30. Refractive index dispersion of silicon nitride material with different nitrogen flows.

In Fig. 4-30 the dependence of the refractive index dispersion of silicon nitride on the nitrogen flow is shown. With nitrogen flow of 6 sccm the refractive index of the layer is very high. This shows that the material is not sufficiently nitrified. By increasing the nitrogen flow the refractive index decreases. The difference between the refractive indices of the deposited material with nitrogen flow 10 sccm and 20 sccm is very small. All the silicon atoms are nitrified and additional nitrogen does not change the silicon nitride structure. Regarding Fig. 4-29 it can be calculated that the saturation level is reached at 16 sccm.

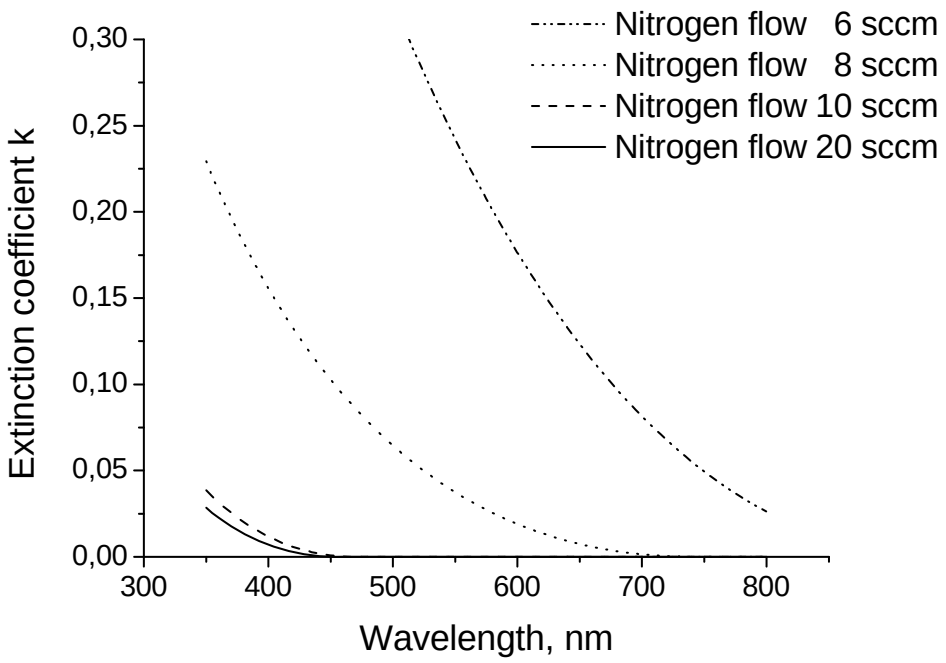

Fig. 4-31. Dependence of the extinction coefficient of silicon nitride from different nitrogen flow.

In Fig. 4-31 the extinction coefficient dispersion of the silicon nitride material for different nitrogen flow is shown. The extinction coefficient represents the absorption in the material. With low nitrogen flow the absorption of the deposited material is very high even in the visible range. Be increasing the nitrogen flow the absorption is decreasing. Again, only minor differences between the properties of the materials deposited with 10 sccm and 20 sccm nitrogen flows exist. The absorption edge is shifted to shorter wavelength. The silicon nitride deposited by the dual ion beam deposition machine has no absorption in the visible (VIS) and infra-red (IR) range. The silicon nitride material is not suitable for optical devices in the UV wavelength range.

Aluminum oxide (Al_xO_y) is deposited and optimized by sputtering of a pure aluminum (Al) target. Additional oxygen of 11 sccm is introduced into the chamber as ionized beam. The deposition rate is measured to 2,1 nm/min. Fig. 4-32 shows that the aluminum oxide has medium refractive index and can be combined with SiO_2. The measurements did not show any absorption in the UV range.

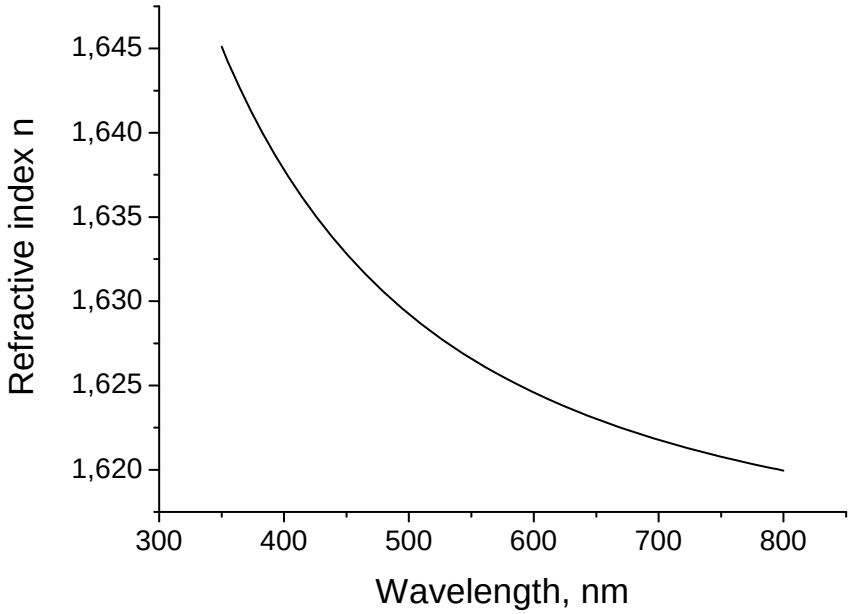

Fig. 4-32. Refractive index dispersion of aluminum oxide (Al_xO_y) deposited by sputtering of pure Al (Aluminum) target.

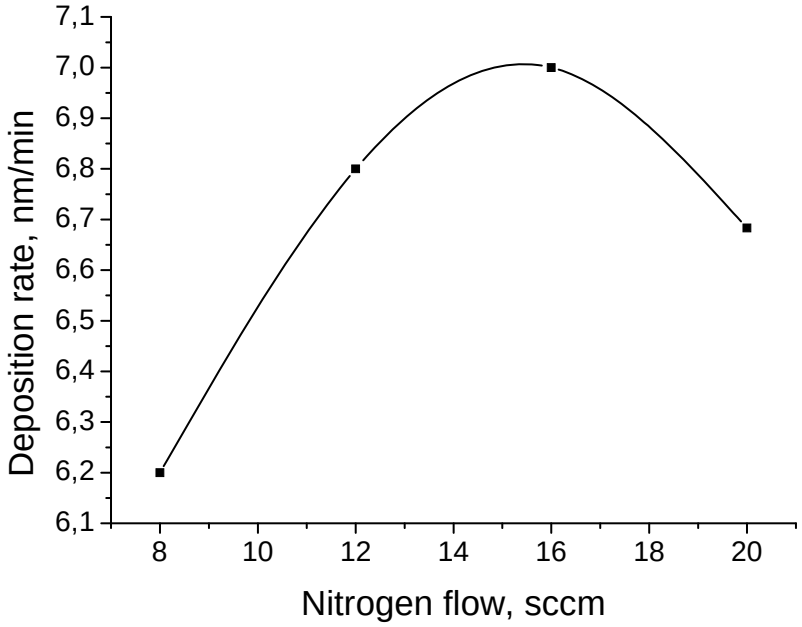

Fig. 4-33. Deposition rate of aluminum nitride (Al_xN_y) versus nitrogen flow. The sputtered target is pure Al material.

In Fig. 4-33 the deposition rate of aluminum nitride material versus the nitrogen flow is shown. The pure aluminum (Al) target is sputtered with energy of the argon (Ar) beam at 800 eV. The nitrogen is introduced into the chamber as an ionized beam with energy of 200 eV. With low nitrogen flow the deposition rate is smaller. The deposited material shows high refractive index (see Fig. 4-34) and high absorption (see Fig. 4-35). The nitrogen is not sufficient and the sputtered silicon is not fully nitrified. By increasing the nitrogen flow the deposition rate increases and the silicon material gets more nitrified. At the same time the refractive index decreases and the absorption edge is shifted to the lower wavelength. At nitrogen gas flow 16 sccm the deposition rate starts to decrease. As discussed before, the reason is the nitride layer on the surface of the target needs higher energy to be sputtered and the higher pressure in the chamber prevents the sputtered material to reach the substrate surface.

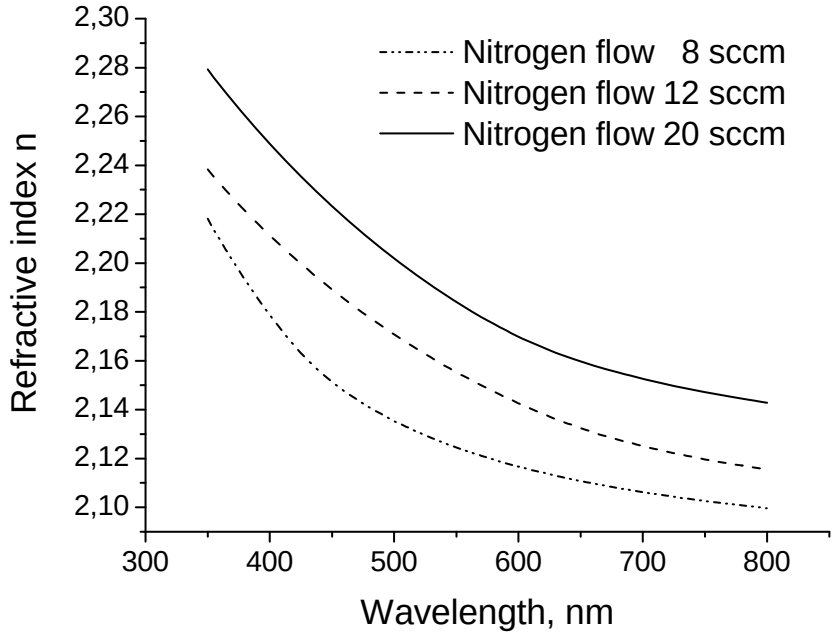

Fig. 4-34. Refractive index dispersion of the aluminum nitride (Al_xN_y) material with different nitrogen flows.

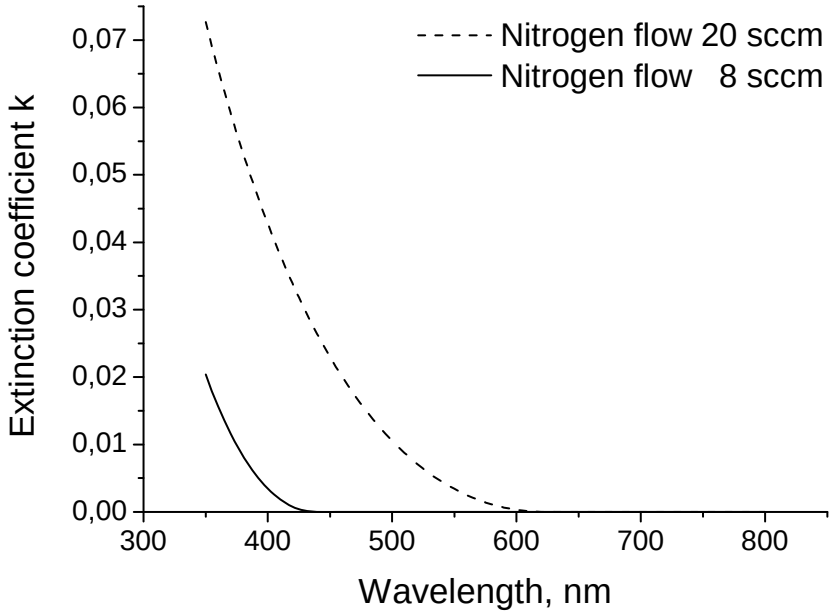

Fig. 4-35. Extinction coefficient of the aluminum nitride (Al_xN_y) with different nitrogen flow.

In Fig. 4-35 can be seen that the aluminum nitride deposited by ion beam assisted deposition method cannot be used for optical devices for wavelength range below 430 nm.

Only several materials deposited and optimized so far can be used for the optical devices operating in the range below 418 nm. Such a material is silicon dioxide (SiO_2). Its refractive index at 418 nm wavelength is n = 1,49 and can be utilized in the multilayer structure as low refractive index material. Another material without absorption in the ultra violet range is aluminum oxide (Al_2O_3). The refractive index at 418 nm wavelength is n = 1,64. The material is characterized as a material with medium refractive index. It can be used in multilayer structure and can be combined with silicon dioxide. The refractive index contrast between both materials is only $\Delta n = 0,15$. To achieve high reflectivity required of the VCSEL structure the DBR mirror should have many periods. In Fig. 4-36 the reflectivity of 20 periods SiO_2/Al_2O_3 DBR mirror is shown. The refractive index of silicon dioxide and zirconium dioxide are measured by spectroscopic ellipsometer. The results from the measurements are used for the simulations of the DBR structure. The reflectivity of the mirror is measured by spectroscopic reflectometry and the results are compared with the simulated reflectivity. The simulated and the measured results have very good overlap. This shows that the transfer matrix method used

by the simulations represents the behavior of the multilayer structure correct. At the same time this is a demonstration of the deposition accuracy of the sputtering method. The spectroscopic ellipsometer gives also very correct measurements results of the optical parameters.

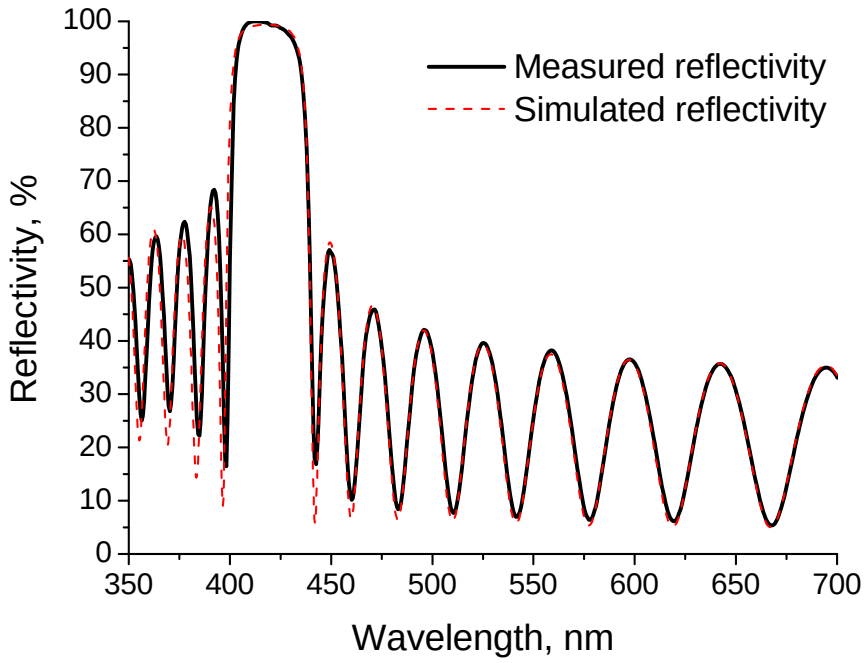

Fig. 4-36. Measured (solid line) and simulated (dashed line) reflectivity of 20 periods SiO_2/Al_2O_3 DBR mirror.

The structure has maximum reflectivity of 99,3 % at wavelength 418 nm (designed for organic material Spiro-6ϕ). The full-with half-maximum (FWHM) of the stop-band is mainly influenced by the refractive index contrast of the materials used in the multilayer structure. The reflectivity of the DBR from Fig. 4-36 has 38 nm FWHM of the stop-band. This narrow stop-band increases the mode competition of the side-modes and reduces the side-mode suppression-ratio (SMSR) of the VCSEL structure. The high number of the periods increases absorption and the scattering of the light. These losses can be caused by the defects in the material and the intermediate surface roughness during the deposition.

Zirconium dioxide (ZrO_2) is a material with high refractive index and no absorption at 395 nm. Combined with silicon dioxide zirconium dioxide is a perfect candidate for a multilayer structure with high refractive index contrast. In this work

zirconium dioxide material is deposited and optimized. As a target zirconium material with purity > 99,9% is used. The zirconium is sputtered with energy of the argon beam at 1000 eV. Additional molecular or ionized oxygen is introduced into the chamber. The thin zirconium dioxide layers used for the optimizations are deposited on silicon substrate. The optical properties are measured by spectroscopic ellipsometry and spectroscopic reflectometry.

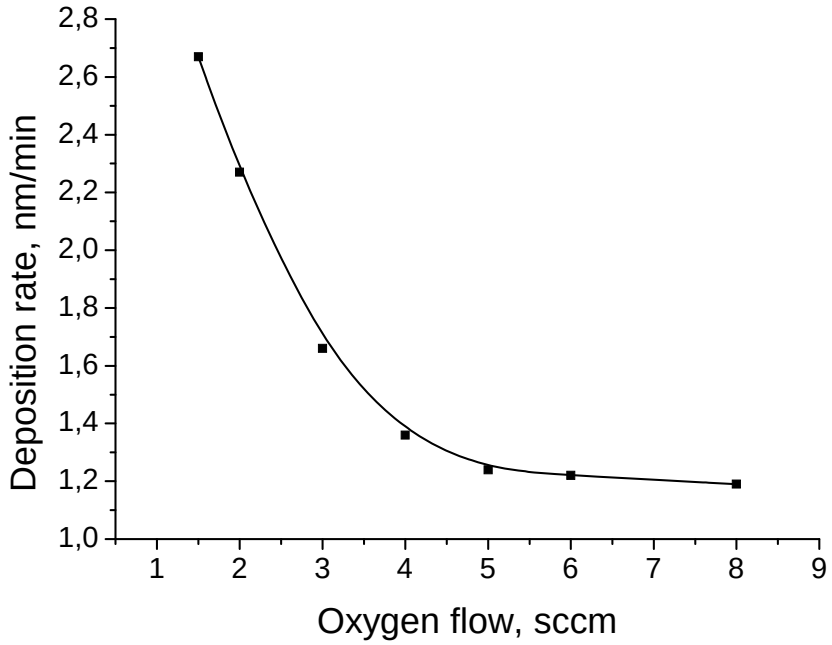

Fig. 4-37. Deposition rate of zirconium oxide (ZiO_x) material versus the oxygen flow.

In Fig. 4-37 the dependence of the deposition rate on the flow of molecular oxygen gas is shown. By increasing the oxygen flow the deposition rate decreases. At the same time the refractive index and the absorption of the material decreases. At the beginning the oxygen flow is not enough to fully oxidize the sputtered zirconium material. The refractive index is very high and the absorption has a very high value in the visible, ultra violet and infra red wavelength range. At oxygen flows bigger than 6 sccm the change of the deposition rate is very small. At this point the oxygen flow is sufficient to oxides the sputtered zirconium material. The change of the refractive index is not dramatic and the absorption is measured to be zero. This region of saturation is used for deposition of ZrO_2 layers in the optical devices. A small deviation of the oxygen flow does not change the optical and the mechanical properties of the material. By increasing of the oxygen flow up to 8 sccm a small absorption is measured (see Fig. 4-39). The reason is

that the materiel is over-oxidized with exceed of oxygen molecules in the material. This deviation from the stoichiometric material shows a lot of defects in the material structure. This can cause absorption or scattering of the light.

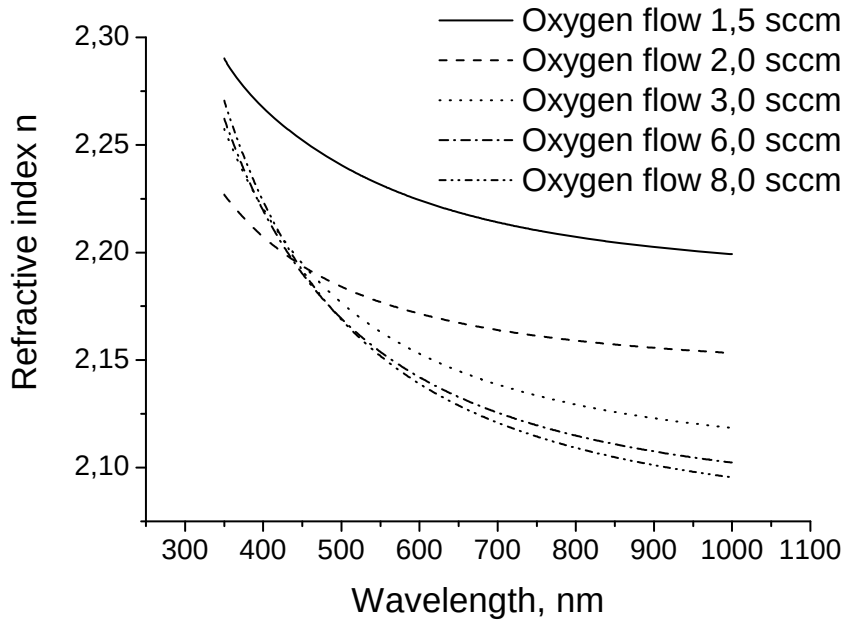

Fig. 4-38. Refractive index dispersion of ZrO_x material with different flows of molecular oxygen gas.

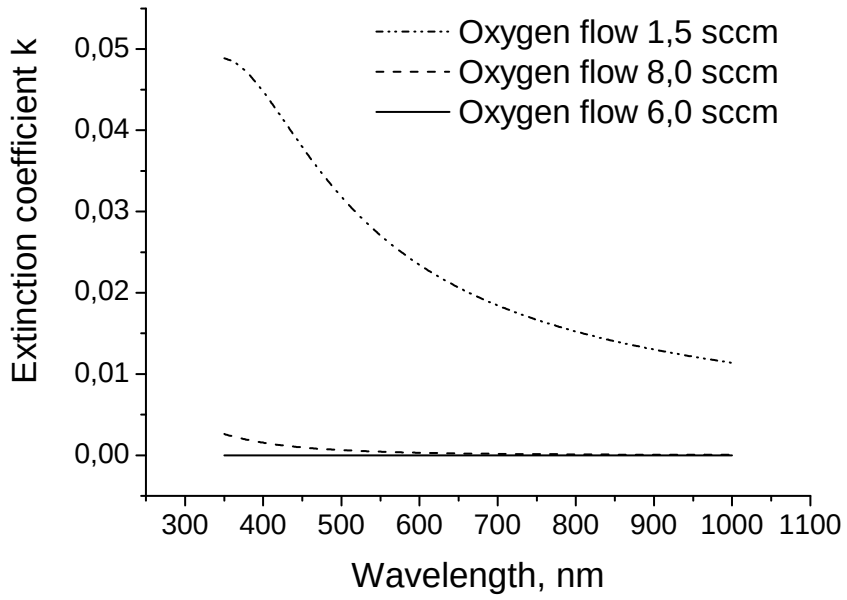

Fig. 4-39. Dispersion of the extinction coefficient of ZrO_x material with different flows of molecular oxygen gas

The zirconium oxide material has lower deposition rate compared to silicon dioxide. To reduce the deposition time of the entire multilayer structure the deposition recipe is optimized for high deposition rate and at the same time for low absorption. In Fig. 4-40 the dependence of the deposition rate from the energy of the oxygen gas is shown. The recipe with molecular (mol) oxygen shows the lowest deposition rate. The refractive index of the deposited material is very high. This can be seen in Fig. 4-41, where the refractive index dispersion for different energies of the oxygen gas is shown. The energy of the oxygen gas is increasing by ignition of oxygen plasma with the assisted ion source (ISQ2). The ionized (ion) oxygen is more reactive and the deposition rate is increased but the refractive index is decreased. By further increasing of the energy by utilizing an oxygen beam with different beam energies (100, 200, 300 eV) the deposition rate is increasing. The sputtered zirconium clusters are more oxidized and the refractive index is decreasing. At an oxygen beam energy of 300 eV the deposition rate is 2,1 nm/min and the refractive index is n = 2,12 at wavelength 395 nm.

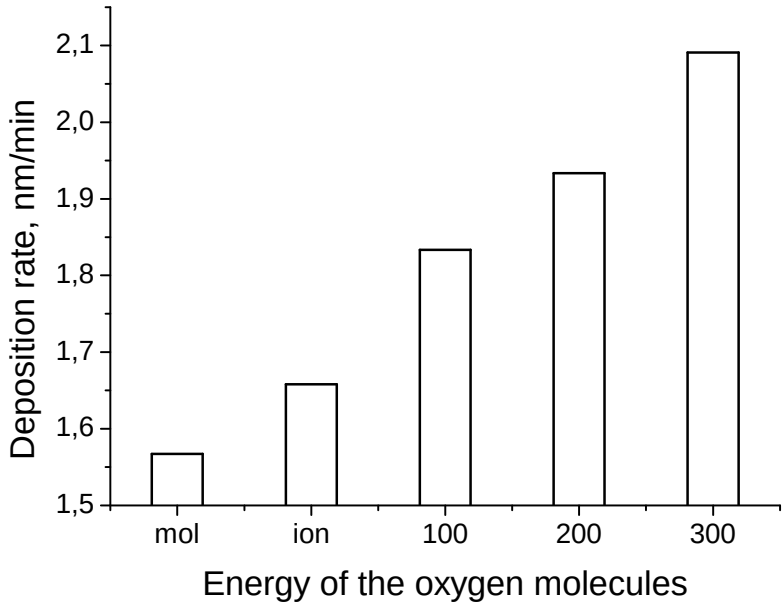

Fig. 4-40. Deposition rate of the zirconium dioxide (ZrO_x) versus the energy of the oxygen introduced in the camber. (where mol – molecular oxygen, ion – ionized oxygen, 100 – 100 eV assisted beam with oxygen, 200 – 200 eV assisted beam with oxygen and 300 – 300 eV assisted beam with oxygen).

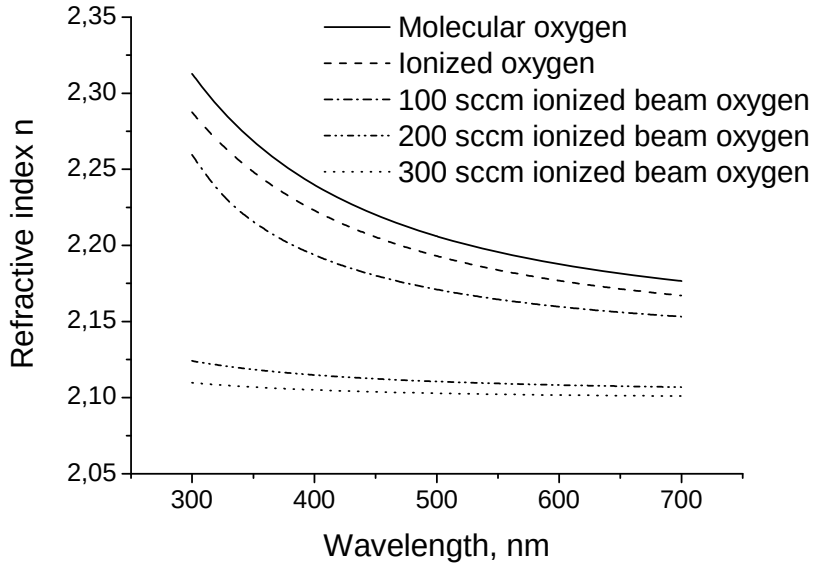

Fig. 4-41. Refractive index dispersion of ZrO_2 material deposited with different energies of the oxygen gas.

In Fig. 4-42 the surface roughness of silicon dioxide (SiO_2) and zirconium dioxide (ZrO_2) materials measured by atomic force microscope (AFM) is shown. The silicon dioxide materials show surface roughness with root mean square RMS = 0,15 nm and the zirconium dioxide has RMS = 0,61 nm. The very low RMS of the layer's surface roughness can be due to error in the measurement setup or error of the results evaluation with the AFM program. The low roughness of the intermediate surfaces reduces the light scattering of the multilayer structure.

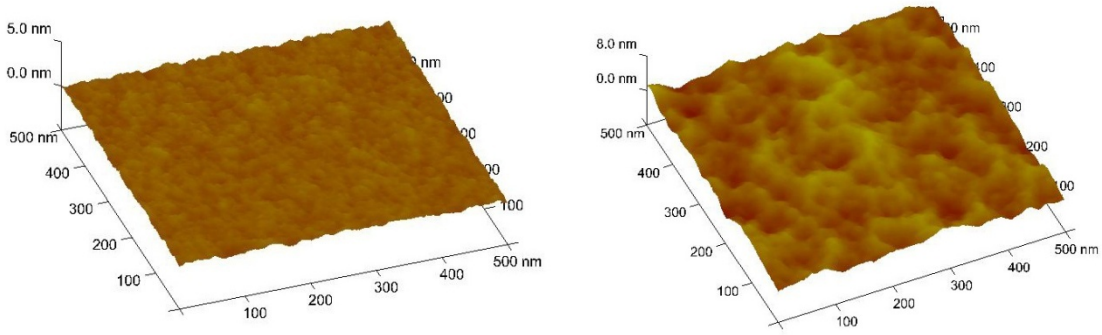

(a) (b)

Fig. 4-42. AFM measurements of the surface roughness of (a) silicon dioxide and (b) zirconium dioxide deposited by DIBD.

In Fig. 4-43 are shown the refractive index dispersion and refractive index contrast of the materials deposited by DIBS and suitable for optical devices working in the ultra violet range (i.e. no absorption in UV). The VCSEL structure requires the combination of at least two materials excluding the active material. The first possible combination is Al_xO_y and SiO_x, which is already discussed and shown in Fig. 4-36. The structure has very small refractive index contrast and requires many periods to achieve high reflectivity.

Another possible combination of materials is ZrO_x and Al_xO_y. The refractive index contrast is higher than the example before and has value of $\Delta n = 0{,}55$. In Fig. 4-44 the measured and the simulated reflectivity of 23 periods ZrO_2/Al_2O_3 mirror is shown [123]. The design wavelength is 395 nm.

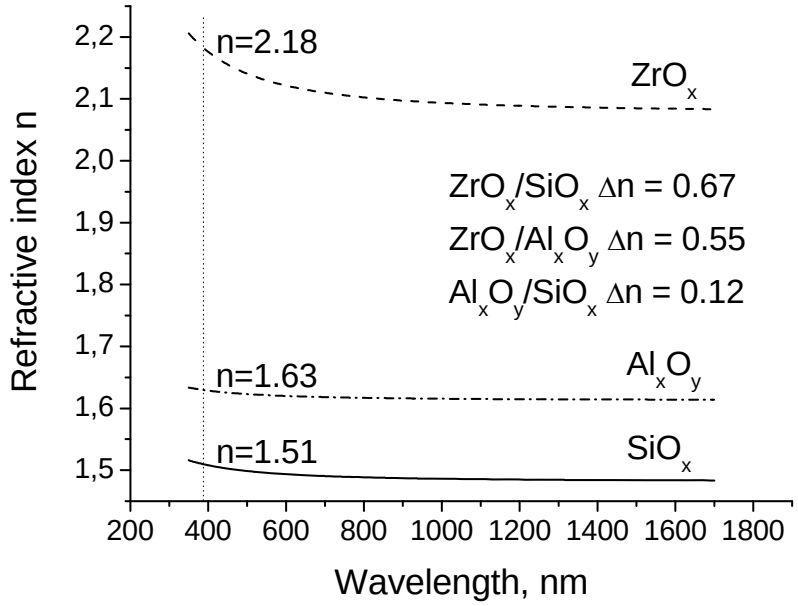

Fig. 4-43. Refractive index dispersion and refractive index contrast of ZrO_x, Al_xO_y and SiO_x materials.

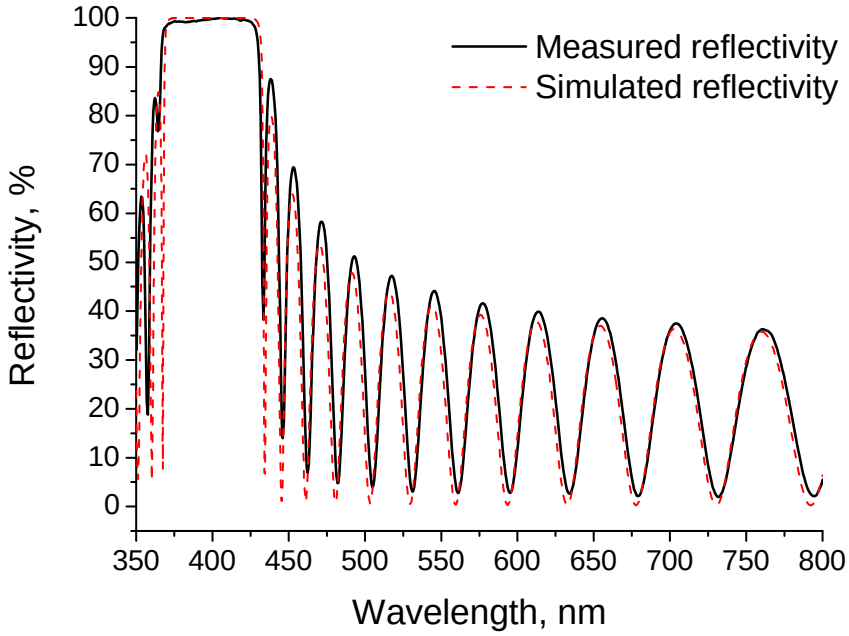

Fig. 4-44. Measured (solid line) and simulated (dashed line) reflectivity of 23 periods ZrO_2/Al_2O_3 DBR mirror [123].

The stop-band of the ZrO_2/Al_2O_3 DBR structure has 66 nm FWHM. Compared to Al_2O_3/SiO_2 (FWHM = 38nm) structure the stop-band is two times wider. In Fig. 4-45 the scanning electron microscope (SEM) picture of a 23 periods ZrO_2/Al_2O_3 DBR mirror is shown. It can be seen that the layers are perfectly parallel and the layer thicknesses are constant in the entire structure.

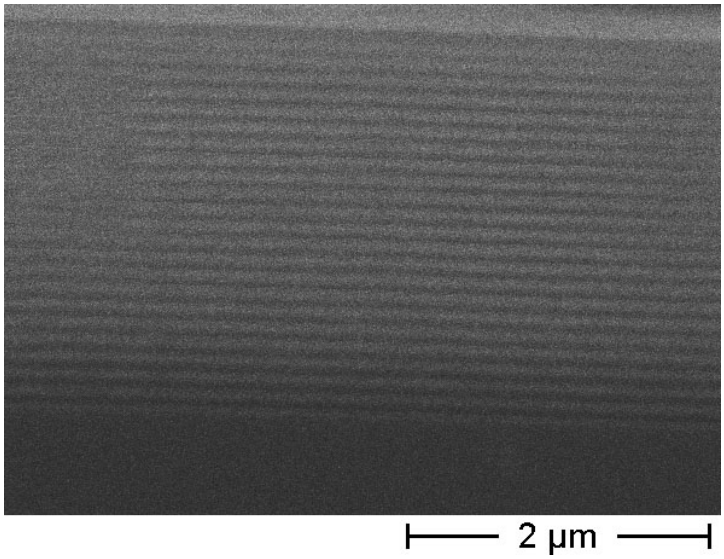

Fig. 4-45. Scanning electron microscope (SEM) picture of 23 periods ZrO_2/Al_2O_3 DBR mirror.

The material combination silicon dioxide (SiO_2) and zirconium dioxide (ZrO_2) has the maximum refractive index contrast of $\Delta n = 0{,}67$ compared to the other materials from Fig. 4-43. This makes deposition of multilayer structures with less periods and high reflectivity possible. Series of DBR depositions and optimizations are carried out. In Fig. 4-46 and Fig. 4-47 measured and simulated reflectivities of ZrO2/SiO2 DBR mirrors with design wavelengths in the ultraviolet and visible spectrum are shown. In Fig. 4-46 the reflectivity of 8 periods ZrO_2/SiO_2 DBR mirror with design wavelength 395 nm is shown. The maximum reflectivity is measured to be more than 99,9 %. The measurements are done in-situ with the spectroscopic reflectometer of the DIBS machine in the wavelength range from 350 to 800 nm. The results are compared with reflectivity measurements done with the reflectivity set-up in the wavelength range from 300 to 800 nm.

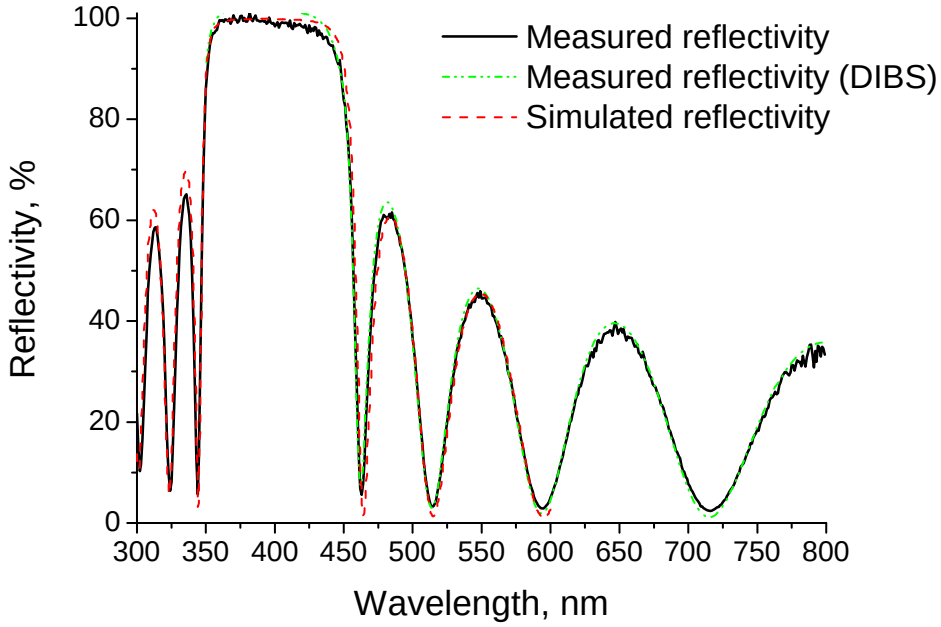

Fig. 4-46. Measured (solid and dash-dotted line) and simulated (dashed line) reflectivity of 8 periods ZrO_2/SiO_2 DBR mirror with design wavelength 395 nm.

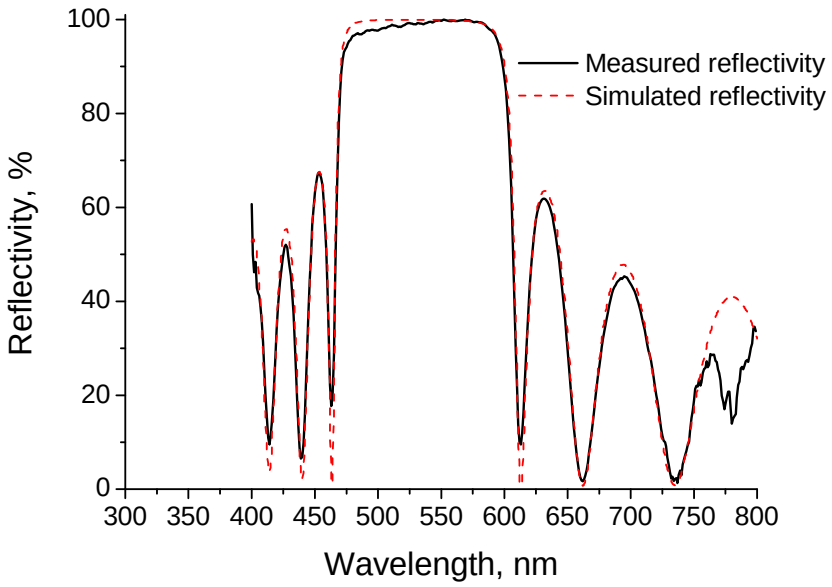

Fig. 4-47. Measured (continuous) and simulated (dashed line) reflectivity of 10 periods ZrO_2/SiO_2 DBR mirror with design wavelength in the visible range.

The FWHM of the stop-band is 110 nm for the DBR with 395 nm design wavelength. In the visible range it is wider and has value of 140 nm. Such a wide stop-band used for laser structures reduces the influence of the side-modes and increase the side-mode suppression-ratio (SMSR). In Fig. 4-48 a SEM picture of an 8 periods ZrO_2/SiO_2 DBR mirror is shown. The brighter lines are the zirconium dioxide layers and the darker lines are the silicon dioxide layers. The bottom part is the silicon substrate.

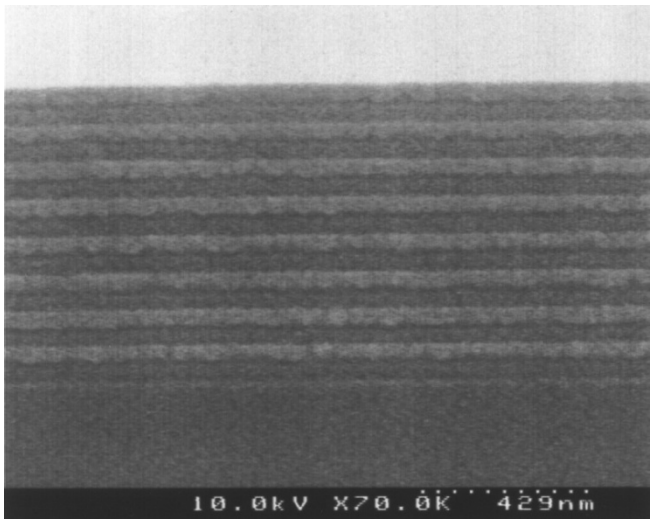

Fig. 4-48. Scanning electron microscope (SEM) picture of an 8 periods ZrO_2/SiO_2 DBR mirror

The deposited multilayer structures are used as bottom DBR mirror in the VCSEL devices. On top of them are deposited the active organic materials as cavity layer. As active materials are used Spiro-Octopus-1 and Spiro-6ϕ from chapter 4.1. (Deposition and optimization of the active organic semiconductor materials). The depositions are done with a dye evaporation machine in the clean room of the department Makromolekulare Chemie und Molekulare Materialien (mmCmm). The thickness is designed to fulfill the requirements for $\lambda_{design}/2$ cavity in an index coupled VCSEL.

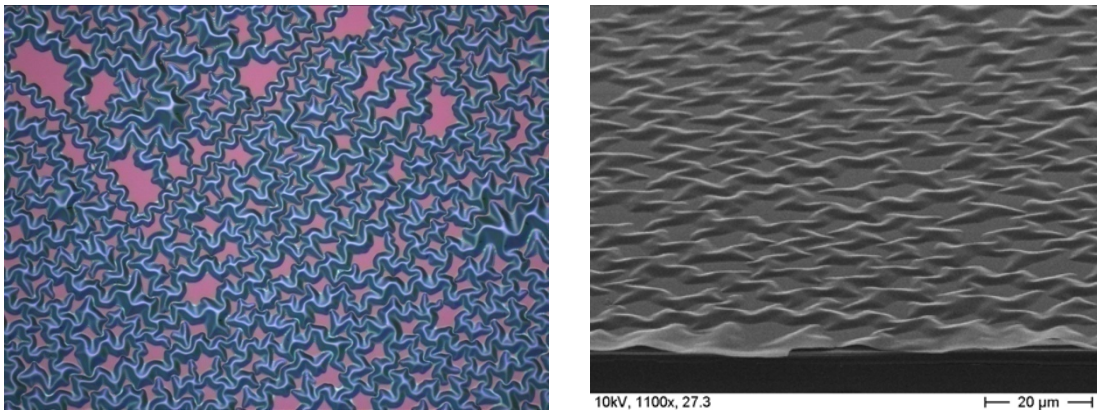

(a) (b)

Fig. 4-49. Pictures of VCSEL structure with top DBR mirror deposited by DIBS machine: (a) light microscope (b) SEM picture

The top DBR mirrors are deposited by utilizing DIBS and PECVD machines. The samples with top DBR mirror deposited by DIBS machine are destroyed by self organized structures on the surface of the samples. In Fig. 4-49 (a) and (b) the light microscope and SEM pictures of the VCSEL structure are shown. The sputtering method is a high energetic process and the atom structure of the deposited materials is very dense. The layers try to relax and to increase their surface in lateral direction. A compressive stress on the organic layer is applied. The shape of the layer of the sensible organic material is changed. As reported before experiments to control the shape and the size of the self organized structures are made [117].

The stress of the silicon dioxide and zirconium dioxide layers deposited by sputtering technique are measured by utilizing the bridge method [118; 119]. In

this method, bridges of 100 nm layer thickness are patterned and under etched. In Fig. 4-50 the schematic diagram of the bridge method and the SEM picture of the patterned and under etched silicon dioxide bridge structure is shown. The stress is calculated by using the following equation:

$$\sigma = \frac{\varepsilon}{1-\vartheta} E_0 \qquad 4.1$$

where

ε	strain
E_0	Young's module
ϑ	Poisson's ratio

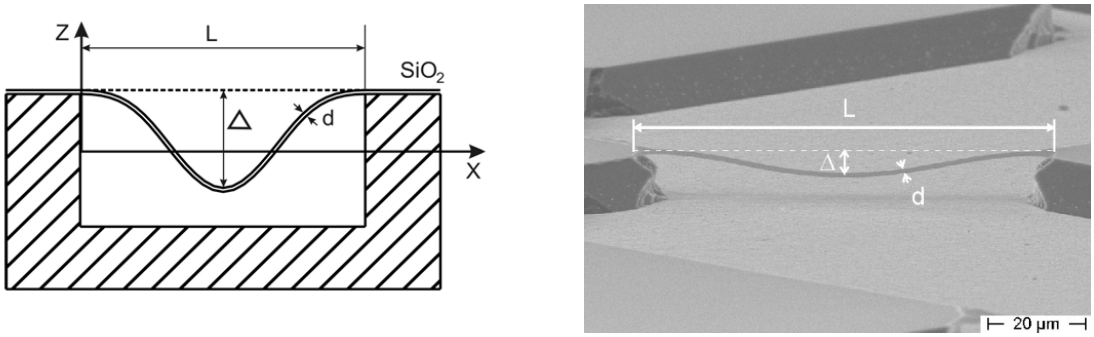

(a) (b)

Fig. 4-50. (a) Schematic diagram of the bridge method and (b) SEM picture of under etched SiO_2 bridge structure

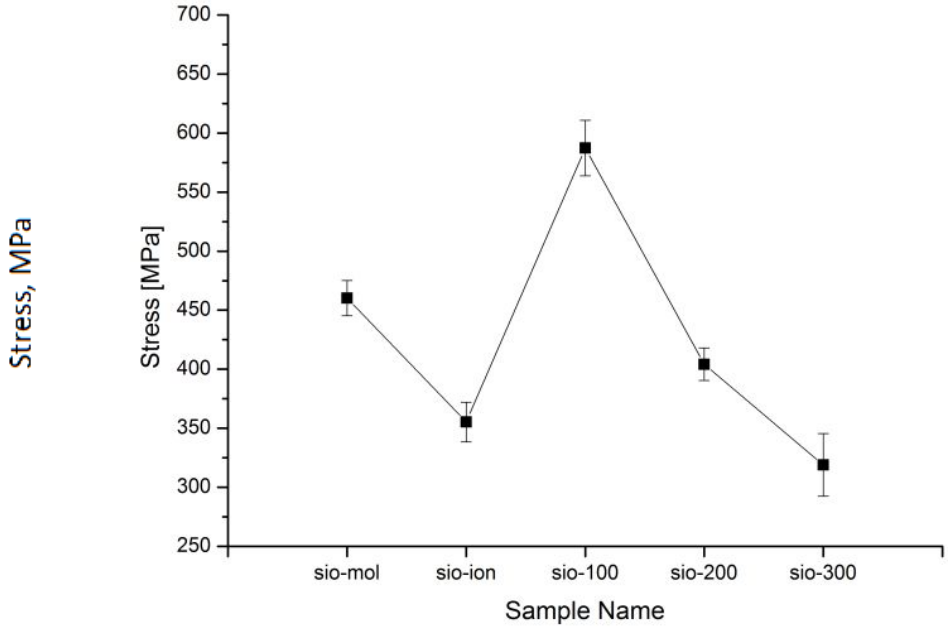

Fig. 4-51. Stress measurements of SiO2 material versus different energies of the oxygen beam (with: sio-mol – molecular oxygen, sio-ion – ionized oxygen, sio-100 – 100 eV assisted beam with oxygen and sio-200 – 200 eV assisted beam with oxygen).

To optimize the stress the energy of the oxygen from the second assisted ion source (ISQ2) has been changed. In Fig. 4-51 the stress in the silicon dioxide layer versus the oxygen energy is shown. By increasing the energy of the oxygen molecules the stress is reducing. Dielectric materials deposited with low energy of the oxygen ion beam show higher value of the stress than with molecular or ionized oxygen. By increasing the ion beam energy the stress is decreasing. The minimum value of the stress σ = 300 MPa is achieved by an oxygen beam with an energy of 300 eV. By utilizing the bridge method the minimum stress in the zirconium dioxide layer is measured to be σ = 1,5 GPa.

The stress of the dielectric materials deposited by sputtering technique cannot be reduced to zero or close to zero by utilizing different energies of the oxygen beam. The PECVD deposition method is a less energetic process and the stress in the layers is lower than by the sputtering process. As reported before [68] by changing the ratio between the low frequency (LF) and high frequency (HF) generated plasma the stress in the silicon nitride and silicon dioxide layers can be tuned.

A UV VCSEL structure with design wavelength λ_{design} = 395 nm is designed and deposited. The bottom DBR is prepared by DIBS machine and consists of 23 and ½ periods Al_2O_3/ZrO_2-Al_2O_3 multilayer structure. In the active region an

organic material Spiro-Octopus-1 is used, which has maximum emission at wavelength λ = 395 nm. On the organic material the top DBR mirror is deposited by a PECVD process and consists of 31 periods SiO_2/Si_3N_4 multilayer structure. More periods are required because the refractive index contrast of SiO_2/Si_3N_4 multilayer structure is smaller than Al_2O_3/ZrO_2. The deposited device shows stable mechanical and optical properties. The UV VCSEL structure is shown in Table 4-3 and SEM picture in Fig. 4-52:

Table 4-3. UV VCSEL structure with emission wavelength at 395 nm

31 periods top SiO_2/Si_3N_4 DBR (deposited by the PECVD)
organic semiconductor material Spiro-Octopus-1 with thickness d = 104 nm (which is 0,5 λ of λ_{design}=395 nm)
23 and ½ periods bottom Al_2O_3/ZrO_2- Al_2O_3 DBR (deposited by the DIBS)
Si-wafer as substrate

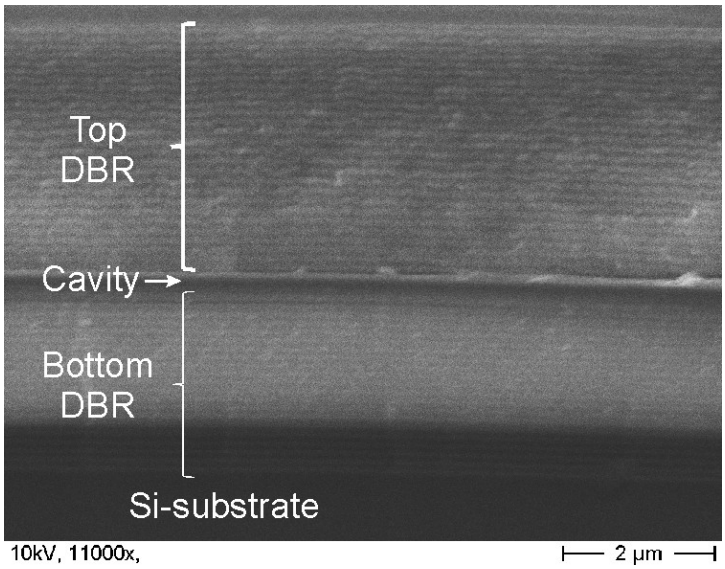

Fig. 4-52. SEM picture of the UV VCSEL structure from Table 4-3

The VCSEL structure is optically pumped from top with a nitrogen laser under angle an of 30 degree. The lasing emission is measured with a spectrometer in the wavelength range from 300 nm to 800 nm. In Fig. 4-53 (a) and (b) the schematic diagram of the pumping and emission direction of the VCSEL structure and the

measurement set-up are shown. The measurement results are shown in Fig. 4-54. Emission is observed only from the side-modes of the stop-band. The expected main-mode at wavelength 395 nm is not visible.

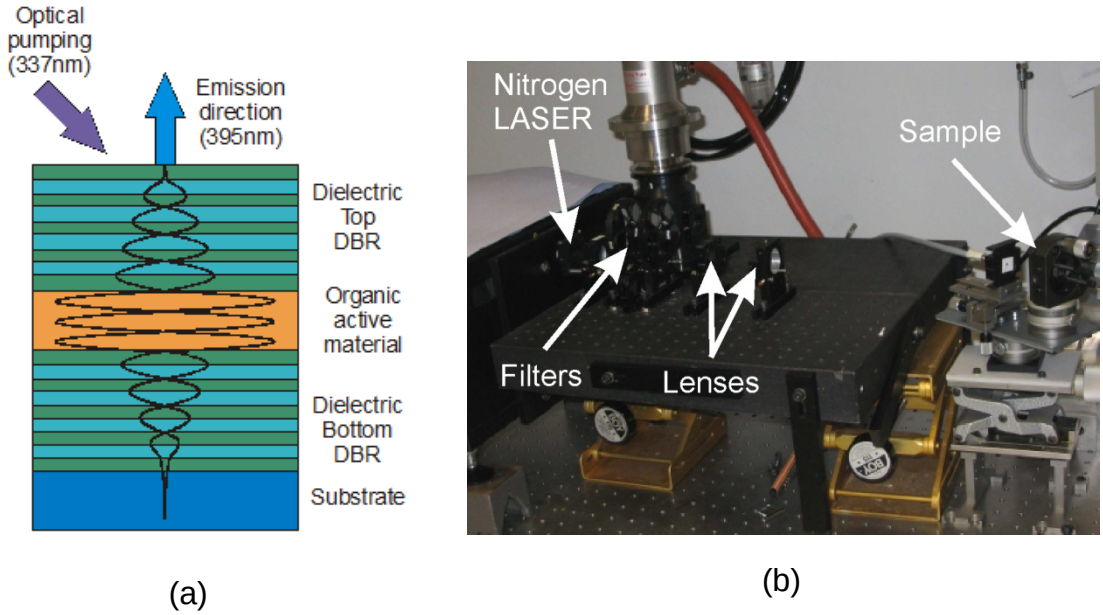

Fig. 4-53. Schematic diagram of (a) pumping and emission direction of the UV VCSEL structure and (b) the pumping measurement set-up at the optic laboratory of mmCmm.

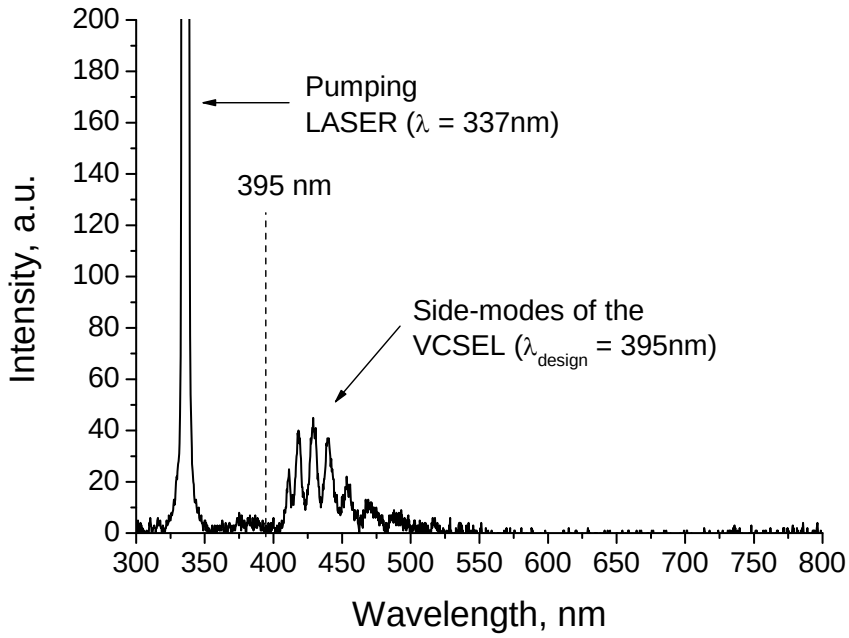

Fig. 4-54. Emission intensity spectrum of the optically pumped UV VCSEL structure from Table 4-3 (31 periods top SiO_2/Si_3N_4 DBR).

The same structure is deposited with 5, 10 and 15 periods of the top SiO_2/Si_3N_4 DBR. In Fig. 4-55 the emission intensity spectrum of the optically pumped UV VCSEL structure with 10 periods top DBR mirror is shown. The main mode can be seen at position λ = 393 nm. The 2 nm difference from the design wavelength of 395 nm is caused by the deposition error of the cavity and the top DBR. The side-modes still can be seen.

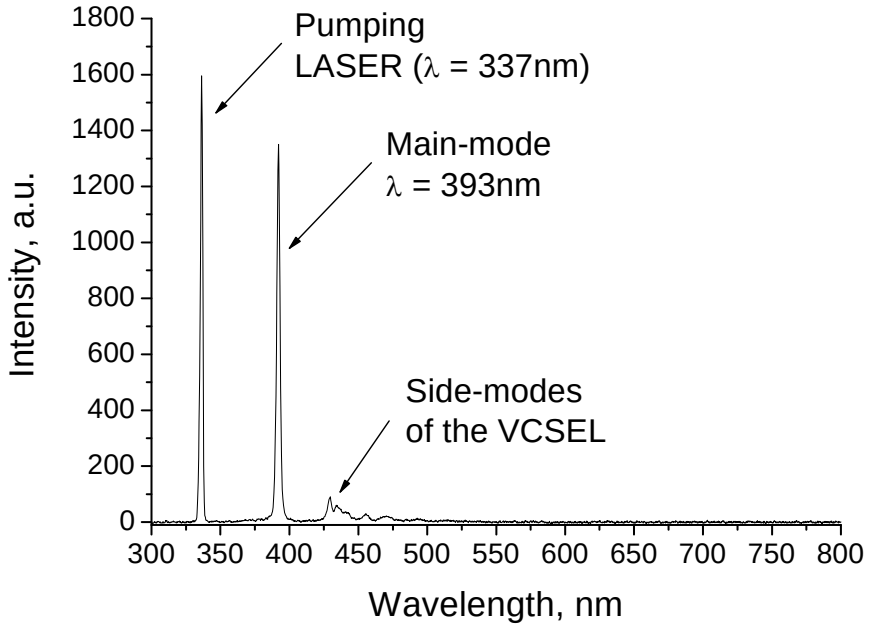

Fig. 4-55. Emission intensity spectrum of the optically pumped UV VCSEL structure with 10 periods top SiO_2/Si_3N_4 DBR.

In Fig. 4-56 dependence of the full-width half-maximum (FWHM) of the main-mode emission from the top DBR period numbers is shown. With 5 periods the FWHM is very wide. Also the reflectivity of the top DBR is low and the filtered light has a wider spectrum. By increasing the periods of the DBR the FWHM of the main-mode is decreasing. With 15 periods the FWHM is 2,5 nm. Even though, a laser behavior of the emitted light is not observed. It is calculated that the reflectivity of 15 periods top DBR is not enough to achieve the lasing threshold. Additionally, the low quality of the top DBR deposited by the PECVD process increases the losses in the VCSEL structure.

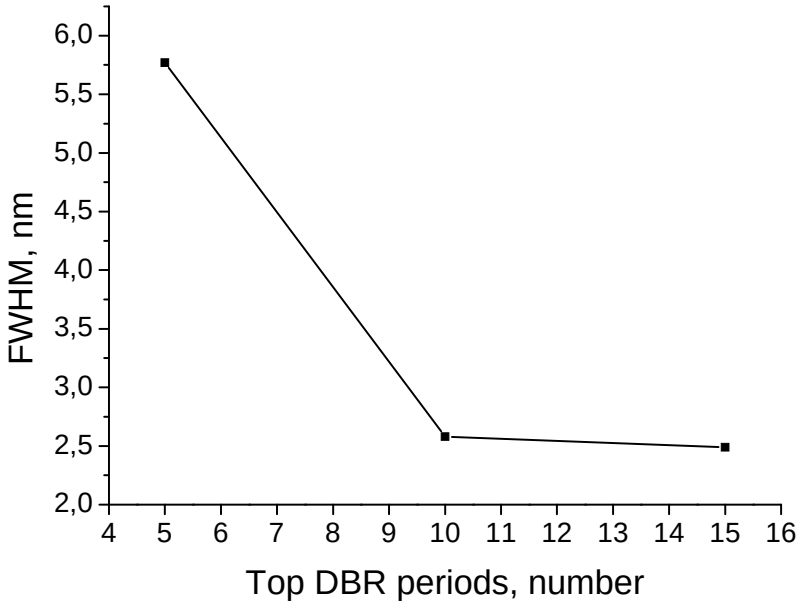

Fig. 4-56. Full-width half-maximum (FWHM) of the main-mode emission versus the periods numbers of the top DBR.

To improve the quality of the top DBR the silicon nitride (Si_3N_4) deposited by PECVD is replaced by zirconium dioxide (ZrO_2) deposited by DIBS. The top DBR consist of a 10 period multilayer structure of SiO_2 deposited by PECVD and ZrO_2 deposited by PECVD. The PECVD SiO_2 material has tensile stress and the DIBS ZrO_2 material has compressive stress. Combined the stress of both materials in the top DBR are compensated. The bottom mirror consist of 15,5 periods SiO_2/ZrO_2- SiO_2 DBR structure deposited by the DIBS on a silicon substrate. As an active material the organic material Spiro-6ϕ is used, which has the maximum emission at $\lambda = 418$ nm. The thickness is chosen to be 0,5 λ and has physical thickness of d = 102 nm. The UV VCSEL structure is shown in Table 4-4 and the SEM picture is shown in Fig. 4-57.

Table 4-4. UV VCSEL structure with emission wavelength at 418 nm

10 periods top SiO_2/ZrO_2 DBR (deposited by the PECVD and DIBS)
organic semiconductor material Spiro-6ϕ with thickness d = 102 nm (λ_{design}=418 nm)
15,5 periods bottom SiO_2/ZrO_2- SiO_2 DBR (deposited by the DIBS)
Si-wafer substrate

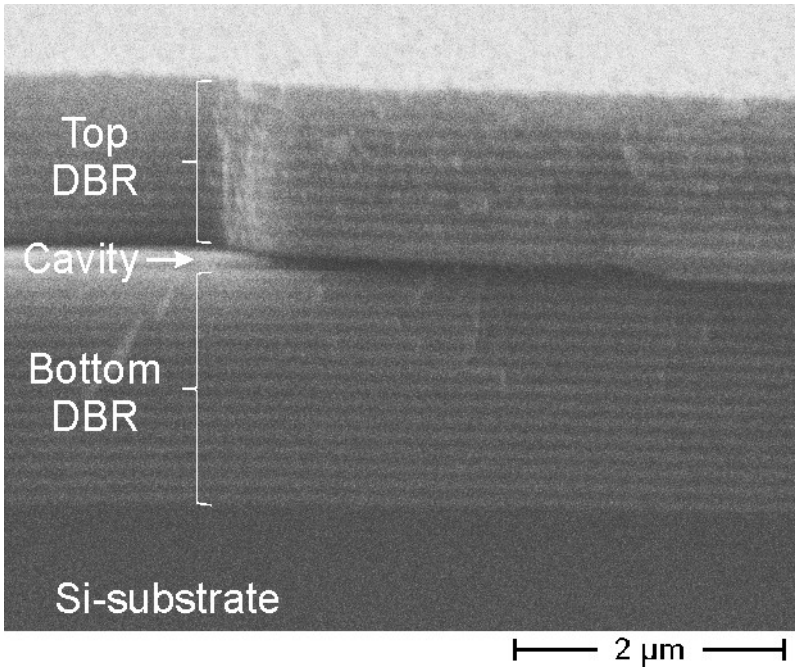

Fig. 4-57. SEM picture of the UV VCSEL structure from Table 4-4.

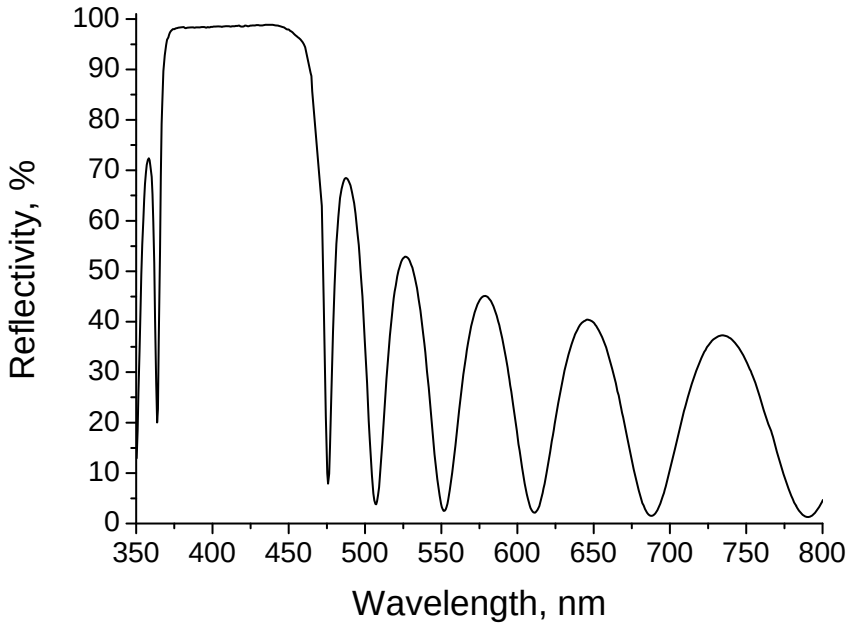

Fig. 4-58. Reflectivity measurements of 15 periods bottom SiO_2/ZrO_2 DBR structure

In Fig. 4-58 the reflectivity of the 15 periods bottom SiO_2/ZrO_2 DBR structure with design wavelength 418 nm is shown. The reflectivity is measured to be higher than 99,9 %. For the VCSEL structure the bottom DBR should have 15,5 periods SiO_2/ZrO_2-SiO_2 DBR mirror. The last SiO_2 layer of the bottom DBR has contact with the organic material and ensures constructive interference of the light (SiO_2 has low refractive index and the organic material has high refractive index).

The structure is optically pumped with a nitrogen laser at wavelength 377 nm under an angle of 30 degree. The emission is measured in the wavelength range from 300 nm to 800 nm. In Fig. 4-59 the emission spectrum of the VCSEL structure is shown. The maximum peek is measured at wavelength 420 nm. The deviation from the design wavelength 418 nm is a result of the deposition error of the organic material thickness and the top DBR structure.

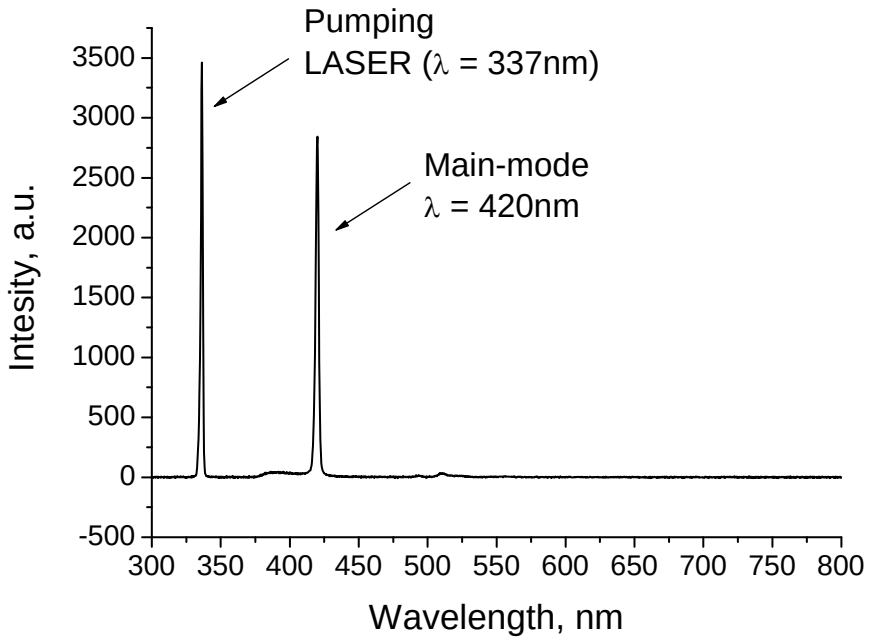

Fig. 4-59. Emission intensity spectrum of the optically pumped UV VCSEL structure with 10 periods top SiO_2/ZrO_2 DBR.

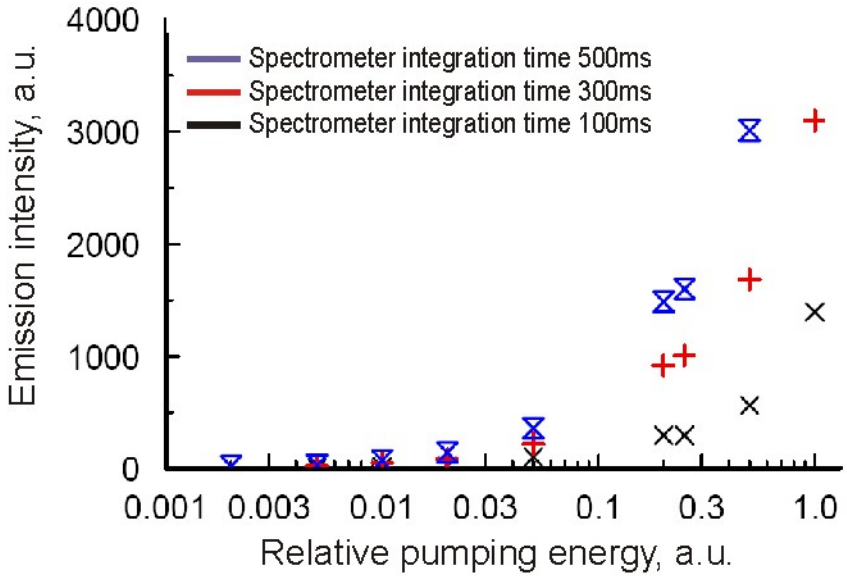

Fig. 4-60. Emission intensity versus the relative pumping power of the optically pumped VCSEL.

In Fig. 4-60 the dependence of the emission intensity from the relative pumping power is shown in logarithmic scale. To prove the tendency of the emission intensity, the structure is pumped and measured with three different integration times. A lasing threshold of the emission intensity is not observed. The top DBR is made by alternating usage of the PECVD and IBD machine. The structure is transported between both machines 20 times under vacuum. Even though, the exposures of the multilayer structure to atmosphere pressure and humidity have reduced the quality of the top DBR mirror.

Chapter 5

Conclusions and outlook

In the first part of this work a hybrid VCSEL structure in the ultraviolet range close to 300 nm has been studied by theoretical model calculation. The investigation shows that suitable materials for the distributed Bragg reflector (DBR) mirrors are the oxides and nitrides of silicon and the oxides of metals like zirconium (Zr) and aluminum (Al). The second part of this thesis deal with the technological implementation of devices and subsequent experimental characterization. Two deposition processes have been utilized for the technological deposition of the dielectric mirrors. Silicon nitride (Si_3N_4) and silicon dioxide (SiO_2) have been deposited with a plasma-enhanced chemical-vapor deposition (PECVD) machine. The deposition method shows absorption of the silicon nitride in the ultraviolet range. This leads to reduction of the optical properties of the DBR. The maximum reflectivity at 400 nm wavelength is measured to be R = 95%, which is not enough to be used as VCSEL resonator. Additionally, the surface roughness is higher and the atomic structure is not in stoichiometry. For the top DBR deposited on the organic material very important parameter is the stress of the layers. The stress in the silicon nitride layers can be tuned and reduced to zero by changing the deposition parameters.

To overcome this problem other dielectric materials have been deposited and optimized by utilizing dual ion beam sputtering (DIBS) machine. The layers have been deposited by sputtering of pure metal targets. By introducing of additional oxygen the sputtered material has been oxidized. The optical properties have been optimized be variation of the energy of the sputtering beam and variation of the oxygen flow. By utilizing the optimized materials it has been found that the best material combination for the DBR mirror is the SiO_2/ZrO_2 multilayer structure. Its

reflectivity has been measured to be more than R = 99,9%. Very important parameter for low scattering of the light is the surface roughness of the deposited layers. It has been measured that the silicon dioxide surface roughness has a root mean square value of RMS = 0,15 nm and the zirconium dioxide has a value of RMS = 0,61 nm. Since the sputtering method is a high energetic process and the structure of the deposited materials is very dense the deposited thin films tend to relax and to increase their surface. This results in stress of the layers, which destroy the organic material in the VCSEL structure. The problem has been solved by a combined deposition of the top SiO_2/ZrO_2 DBR. The silicon dioxide has been deposited by the low energetic PECVD process and the zirconium dioxide using the DIBS machine. In this way the compressive stress of ZrO_2 is compensated by the tensile stress of SiO_2 material.

In the active region an organic material has been used. This work was done in collaboration with the mmCmm department, where spiro based organic materials are synthesized and deposited. Laser structures have been optimized and fabricated by utilizing Spiro-Octopus-1 or Spiro-6ϕ organic materials. The devices have been pumped with a nitrogen laser at 337 nm. The VCSEL structure with Spiro-Octopus-1 shows an emission at 392 nm and the device with Spiro-6ϕ has an emission at λ = 420 nm. Organic materials with an emission lower than λ = 380 nm are under investigation in the laboratories of the mmCmm department.

The VCSEL structure for the ultra violet wavelength range shows high sensitivity to the quality of the deposited materials. The layers should have low surface roughness; defects free material atom structures and zero absorption at the emission and pumping wavelengths. The deposition method for the dielectric materials should produce materials with low stress and should enable a constant deposition rate for longer deposition times. The DIBS machine shows the best results. The stress of the layers deposited by sputtering method is still under investigation and optimization. To overcome the surface damage caused by high energy sputtering particles Chichibu has proposed the reactive helicon-wave-excited-plasma sputtering method [120].

The optimum procedure for deposition of the multilayer VCSEL structure is to use only one deposition machine with two chambers. The first chamber is for the deposition of the dielectric materials and the second – for the deposition of the organic materials. The transportation of the sample between the two chambers should be done under vacuum trough common load-lock. In this way the influence of the oxygen in the atmosphere and the humidity is excluded.

Appendix A

Recipes for deposition of dielectric materials by PECVD machine:

Table 5-1. PECVD process parameters for deposition of SixNy material at 120°C

Si_xN_y 120°C Sample name: TSn – 136 I			
1.	**Base Pressure**	**Abpumpen**	
2.	**Process**		
	Gas 1 – 2%SiH4-N2	1000	sccm
	Gas 2 – NH3	20	sccm
	Gas 3	-	sccm
	HF forword power	200	W
	LF power	20	W
	RF mode	Pulsed	
	RF first puls	LF	
	HF pulse time	20	sec
	LF pulse time	6	sec
	Process pressure	0.650	Torr
	Substrate temperature	120	deg.C
	Step time	0:07:42	hms
3.	**Process**	**18:00:00 Abpumpen und Halten**	
	RF mode	Continous	
	RF first pulse	HF	
	Substrate temperature	120	deg.C
	Step time	18:00:00	hms

Table 5-2. PECVD process parameters for deposition of SiOx material at 120°C

SiO_2 120°C Sample name: TSn – 136 II			
1.	**Base Pressure**	**Abpumpen**	
2.	**Process**		
	Gas 1 – 2%SiH4-N2	430	sccm
	Gas 2	-	sccm
	Gas 3 – N_2O	710	sccm
	HF forword power	200	W
	LF power	-	W
	RF mode	Continuouse	
	RF first puls	HF	
	HF pulse time	-	sec
	LF pulse time	-	sec
	Process pressure	1.0	Torr
	Substrate temperature	120	deg.C
	Step time	0:01:30	hms
3.	**Process**	**18:00:00 Abpumpen und Halten**	
	RF mode	Continous	
	RF first pulse	HF	
	Substrate temperature	120	deg.C
	Step time	18:00:00	hms

Recipes for deposition of dielectric materials by DIBS machine:

Table 5-3. Process parameters for deposition and optimization of Al_2O_3 material by using DIBS machine and ceramic target.

Process name:	**ts2n002alo1**	
Goal:	**Optimization of Al_2O_3**	
Substrate:	**Si-sub**	
Technologie:	**Sputtering**	
Wafer name:	**Ts2n11-2**	
Date:	**08.06.2005**	
Holder Position (Po)	100	mm
Holder Kipping (Ki)	90	grad
Holder Rotation (Ro)	150	rpm
Target Position (T)	235	mm
Deposition Time	3600	sec
ArMFC1 (Ar for ISQ1)	10	sccm
XeMFC2 (Xe for ISQ1)	0	sccm
ISQ1	**on**	
Programe name:	ISQ1_PS1	
MW Power:	250	W
Beam Voltage:	1150	V
Bean Current:	105	mA
Accelerator Voltage:	400	V
Pulsfrequenz:	20000	Hz
Pulsweite:	65	%
Beam switch	on	
ArMFC3 (Ar for ISQ2)	-	sccm
O2MFC4 (O_2 for ISQ2)	-	sccm
ISQ2	**off**	
Programe name:	-	
MW Power:	-	
Beam Voltage:	-	
Bean Current:	-	
Accelerator Voltage:	-	
Pulsfrequenz:	-	
Pulsweite:	-	
Beam switch	-	

Table 5-4. Process parameters for deposition and optimization of SiO_2 material by using pure silicon target and additional oxygen.

Process name:	**08sio-tsn217iv**	
Goal:	**Optimization of SiO_x**	
Substrate:	**Si-sub**	
Technologie:	**Sputtering**	
Wafer name:	**Tsn217iv**	
Date:	**09.10.2005**	
Holder Position (Po)	0	mm
Holder Kipping (Ki)	90	grad
Holder Rotation (Ro)	150	rpm
Target Position (T)	55	mm
Deposition Time	1800	sec
ArMFC1 (Ar for ISQ1)	8	sccm
XeMFC2 (Xe for ISQ1)	0	sccm
ISQ1	**on**	
Programe name:	ISQ1_sio01	
MW Power:	250	W
Beam Voltage:	500	V
Bean Current:	45	mA
Accelerator Voltage:	100	V
Pulsfrequenz:		Hz
Pulsweite:		%
Beam switch	on	
ArMFC3 (Ar for ISQ2)	-	sccm
O2MFC4 (O_2 for ISQ2)	7	sccm
ISQ2	**off**	
Programe name:	-	
MW Power:	-	
Beam Voltage:	-	
Bean Current:	-	
Accelerator Voltage:	-	
Pulsfrequenz:	-	
Pulsweite:	-	
Beam switch	-	

Table 5-5. Process parameters for deposition and optimization of SiO_2 material by using pure silicon target and additional ionized oxygen.

Process name:	**08sio-tsn217iv**	
Goal:	**Optimization of SiO_x**	
Substrate:	**Si-sub**	
Technologie:	**Sputtering**	
Wafer name:	**Tsn217iv**	
Date:	**09.10.2005**	
Holder Position (Po)	0	mm
Holder Kipping (Ki)	90	grad
Holder Rotation (Ro)	150	rpm
Target Position (T)	55	mm
Deposition Time	1800	sec
ArMFC1 (Ar for ISQ1)	8	sccm
XeMFC2 (Xe for ISQ1)	0	sccm
ISQ1	**on**	
Programe name:	ISQ1_sio01	
MW Power:	250	W
Beam Voltage:	500	V
Bean Current:	45	mA
Accelerator Voltage:	100	V
Pulsfrequenz:		Hz
Pulsweite:		%
Beam switch	on	
ArMFC3 (Ar for ISQ2)	-	sccm
O2MFC4 (O_2 for ISQ2)	6	sccm
ISQ2	**on**	
Programe name:	ISQ2_sio01	
MW Power:	250	W
Beam Voltage:	-	V
Bean Current:	-	mA
Accelerator Voltage:	-	V
Pulsfrequenz:	-	Hz
Pulsweite:	-	%
Beam switch	off	

Abbreviations:

AFM	Atomic Force Microscope
ASE	Amplified spontaneous emission
DBR	Distributed Bragg reflector
DFB	Distributed feedback (laser)
DIBS	Dual ion beam sputtering
FWHM	Full width half maximum
GUI	Graphical user interface
HF	High frequency
IBAD	Ion beam assisted deposition
IBD	Ion beam deposition
IR	Infra-red wavelength range
ISQ1	Ion source one – sputtering ion source
ISQ2	Ion source two – assisted ion source
LED	Light emitting diode
LF	Low frequency
MFC	Mass flow controller
MW	Micro wave
NIR	Near infrared
OLED	Organic light emitting diode
PECVD	Plasma Enhanced Chemical Vapor Deposition
RF	Radio frequency
RMS	Root Mean Square
SE	Spectroscopic ellipsometer
SEM	Scanning Electron Microscope
SMSR	Side-mode suppression-ratio
SR	Spectroscopic reflectometer
UV	Ultra-violet wavelength range
VCSEL	Vertical-cavity surface-emitting laser
VECSEL	Vertical external cavity surface-emitting laser
VIS	Visible wavelength range
vs.	versus
WLI	Whit-Light Interferometer

References

[1]. **Klepser, B. und Hillmer, H.** "Investigation fo thermal crosstalk in Laser arrays for WDM applications". *Journal of Lightwave Technology.* 10. October 1998, Vol. 16, 10, S. 1888-1894.

[2]. **Hillmer, H. und Klepser, B.** "Low-cost edge-emitting DFB laser arrays for DWDM communication systems implemented by bent and tilted waveguides". *IEEE Journal of Quantum Electronics.* 10. October 2004, Vol. 40, 10, S. 1377-1383 .

[3]. **Wöste, L.H. und Sauerbrey, R.** "Mit dem Laser gegen Blitz und Donner". *Naturwissenschaften.* 2006, S. 19-21.

[4]. **Thomson, G.** "How Products Are Made - Volume 6". [Online] 2006. http://www.madehow.com/.

[5]. **Kim, G.B., et al.** "End-pumped green and blue vertical external cavity surface emitting laser devices". *Applied Physics Letters.* 2006, Vol. 89, S. 181106-1 - 181106-3.

[6]. **Canedy, C.L., et al.** "High-power and high-efficiency midwave-infrared interband cascade lasers". *APPLIED PHYSICS LETTERS.* 2006, Vol. 88, S. 161103-1 - 161103-3.

[7]. **Park, S.H., et al.** "Room-temperature GaN vertical-cavity surface-emitting laser operation in an extended cavity scheme". *APPLIED PHYSICS LETTERS.* 15. September 2003, Vol. 83, 11, S. 1212 - 1223.

[8]. **Hillmer, H., et al.** "Ultra-wide continuously tunable 1.55µm vertical air-cavity filters and VCSEL’s based on micromachined electrostatic actuation". *Proceedings of SPIE.* 19-25. Jan 2002, Vol. 4646, S. 145.

[9]. **Hillmer, H.** "Bent waveguides improve DFB laser performance". *Laser Focus World 31.* 1995, S. 117-122.

[10]. **Daleiden, J. und Hillmer, H.** "Multiple air-gap filters and constricted mesa lasers - material procesing meets the front of optical device technology". *Appl. Phys. B.* 2003, Vol. 76, S. 821-832.

[11]. **Tarraf, A., et al.** "Continuously tunable 1.55µm VCSEL Implemented by precisely curved Dielectric top DBR involving tailored stress". *IEEE Photonics Technology Letters.* 3. March 2004, Vol. 16, 3, S. 720-722.

[12]. **Schneider, D., et al.** "An Ultraviolet Organic Thin-Film Solid-State Laser for Biomarker Applications". *Adv. Mater.* 6. January 2005, Vol. 1, 17, S. 31-34.

[13]. **Salbeck, J., Schörner, M. und Fuhrmann, T.** "Optical amplification in spiro-type molecular glasses". *Thin Solid Films 417.* 2002, S. 20-25.

[14]. **Lemmer, U., Kallinger, C. und Feldmann, J.** "Laserlicht aus Polymern". *Physikalische Blätter.* 2000, Vol. 56, 1, S. 25-30.

[15]. **Jordan, G., et al.** "Light amplificationat 501 nm and large nanosecond optical gain in organic dye-doped polymerc wavegiudes". *Applied Physics Letters.* 2006, Vol. 88, S. 161114-1 - 161114-3.

[16]. **Sakanoue, T., Yahiro, M. und Abachi, C.** "Ambipolar light-emitting organic field-effect transistors using a wide-band-gap blue emittin small molecule". *Applied Physics Letters.* 2007, Vol. 90, S. 171118-1 - 171118-3.

[17]. **Hagen, J.A., et al.** "Enganced emission efficiency in organic light-emittion diodes using deoxyribonucleic acid complex as an electron blocking layer". *Applied Physics Letters.* 2006, Vol. 88, S. 171109-1 - 171109-3.

[18]. **Zhang, Y., et al.** "Organic pure-blue-light-emitting devices based on terfluorenes compounds". *Applied Physics Letters.* 2005, Vol. 87, S. 241112-1 - 241112-3.

[19]. **Salbeck, J, Bauer, J und Weisörtel, F.** "Spiro Linked Compaunds as Active Materials in Organic Light Emitting Diods". *Polymer Preprints.* 1997, 38, S. 349.

[20]. **Heeger, A.J.** "Light emission from simiconducting polymers: Light-emitting diods, light-emitting electrochemical cells, lasers and whtie light for the future". *Solid State Communications.* 1998, Vol. 107, 11, S. 673-679.

[21]. **Berrgren, M., Dodabalapur, A. und Slusher, R.E.** "Stimulated emission and lasing in dye-doped organic thin films with Forster transfer". *Appl. Phys. Lett.* 1997, Vol. 71, 16, S. 2230-2232.

[22]. **Salbeck, J.** "Electroluminescence with Organic Compounds". *Ber. Bunsenges. Phys Chem.* 1996, Vol. 100, 10, S. 1667-1677.

[23]. **Steuber, F., et al.** "White Light Emission from Organic LEDs Utilising Spiro Compaunds with High-Temperature Stability". *Adv. Mater.* 2000, Vol. 2, 12, S. 130-133.

[24]. **He, G., et al.** "Very high-efficiency and low voltage phosphorescent organic light-emitting diods based in a p-i-n junction". *Journal of applied physics.* 15. May 2004, Vol. 95, 10, S. 5773-5777.

[25]. **Schneider, D., et al.** "Deep blue widely tunable organic solid-state laser based on a spirobifluorene derivative". *Applied Physics Letters.* 7. June 2004, Vol. 84, 23, S. 4693-4695.

[26]. **Tessler, N., Denton, G.J. und Friend, R.H.** *Nature.* 1996, Vol. 382, S. 395.

[27]. **Bulovic, V., et al.** *Science.* 1998, Vol. 279, S. 553.

[28]. **Kozlov, V.G., et al.** *Nature.* 1997, Vol. 389, S. 362.

[29]. **Mackowiak, P. und Nakwaski, W.** "Some aspects of designing an efficient nitride VCSEL resonator". *Journal of Physics D: Applied Physics.* 2001, Vol. 34, S. 954-958.

[30]. **Song, Y.K., et al.** "Resonant cavity InGaN quantum-well blue light-emitting diodes". *Applied Physics Letters.* 2000, Vol. 77, 12, S. 1744 - 1746.

[31]. **Martin, R.W., et al.** "Dielectric Bragg Mirrors for InGaN Surface-Emitting Lasers". *Phys. Stat. Sol. (a).* 1999, Vol. 176, 67, S. 67 -71.

[32]. **Persano, L., et al.** "Monolithic polymer microcavity lasers with on-top evaporated dielectric mirrors". *Applied Physics Letters.* 2006, Vol. 88, S. 121110-1 - 121110-3.

[33]. **Persano, L., et al.** "Low-threshold blue-emitting monolithic polymer vertical cavity surface-emitting lasers". *Applied Physics Letters.* 2006, Vol. 89, S. 121111-1 - 121111-2.

[34]. **Schuegraf, K.K.** "Handbook of thin film deposition processes and techniques : principles, methods, equipment and application". 1988, S. 3.

[35]. **Devasahayam, A.J., et al.** "Material properties of ion beam deposited oxides for the optoelectronic industry". *J. Vac. Sci. Technol. A.* 2002, Vol. 20, 3, S. 1135-1140.

[36]. **Kaufman, H., Kahn, J. und Nethery, R.** "Modular Linear Ion Source". *Society of Vacuum Coaters.* 2004, S. 505.

[37]. **Wadley, H., Zhou, X. und Quan, J.** "Biased Target Ion Beam Deposition of GMR Multilayers". *4Wave, Inc. Sterling, VA 20166.*

[38]. —. "Biased Target Ion Beam Deposition of Spin-valves". *4Wave, Inc. Sterling, VA 20166.*

[39]. **Wasa, K. und Hayakawa, S.** "Handbook of sputter deposition technology: principles, technology and applications". 1992.

[40]. **4Wave.** "Ion Beam Depositon". [Online] 2007. http://www.4waveinc.com/iVol.html.

[41]. **Mashkova, E.S. und Molchanov, V.A.** *Radiat. Eff. 16.* 1972. S. 143.

[42]. **Verbeek, H.** "Material characterisaion using ion beams". 1978, S. 303.

[43]. **Mashkova, E.S. und Molchanov, V.A.** *ibid. 23.* 1974. S. 215.

[44]. —. *ibid. 110.* 1989. S. 227.

[45]. **Eckstein, W. und Verbeek, H.** "Data compendium for plasma surface interction". *Nucl. fusion special issue.* 1984, S. 12.

[46]. **Maskova, E.S. und Molchanov, V.A.** "Medium energy ion scattering from solids". *Modern problems in condensed matter science.* 1985, 11, S. 408.

[47]. **Behrisch, R. und Wittmaack, K.** *"Sputtering by Partical Bombardment III. Characteristics of sputtered paricals, Technical applications".* 1991. S. 1-15.

[48]. **Scherzer, B.M.U. und Behrisch, R.** "Sputtering by particle bombardment II. Sputtering of alloys and compounds, electron and neutron sputtering, surface topography.". 1983, S. 271.

[49]. **Taglauer, E. und Heiland, W.** "Inelastic particle-surface collisions". *Springer Ser. Chem. Phys.* 1981, S. 52.

[50]. PVD coatings. *"The theory of PVD coatings".* [Online] 2005. http://pvd-coatings.co.uk/.

[51]. **Robinson, M.T. und Behrisch, R.** "Sputtering by ion bombardment I. Physical sputtering of single-element solids". 1981, S. 73.

[52]. **Yamamura, Y. und Bohdansky, J.** *Vacuum 35.* 1985, S. 561.

[53]. **Eckstein, W. und Biersack, J.** *Z. Phys. B 63.* 1986, S. 109.

[54]. **Mulders, J., Winter, D. und Duinkerken, W.** "Measurements and calculations of FIB milling yield of bulk metals". *Nanoscale Engineering and Fabrication.* 2006, S. 1540-1543.

[55]. **Ziegler, J.** "Particle interactions with matter". [Online] http://www.srim.org/.

[56]. **Gray, M.D. und Edmunds, M.G.** "Modification of Dust Grain Structure by Sputtering". *Mon.Not.Roy.Astron.Soc. 349.* 2004, S. 491.

[57]. **Stoltz, P.H. und Veitzer, S.** "Simulation of heavy ion induced electron yield at grazing incidence". *Physical Review Special Topics - Accelerators And Beams.* 2004, 7, S. 103201.

[58]. **Lorch, S.** "Herstellung, Charakterisierung und Anwendungen von ionenstrahlgesputterten optischen Schichten". *Dissertation Universität Ulm.* 2006.

[59]. **Cuomo, J.J. und Rossnagel, S.M.** "Handbook of ion beam processing technology: principles, deposition, film modification and synthesis". 1989.

[60]. **Kienel, G.** "Vakuumbeschichtung 3. Anlagenautomatisierung - Meß- und Analysetechnik". 1994.

[61]. **Mackenzie, K., et al.** "Optimization of low stress PECVD silicon nitride". *Compound Semi & Microtechniligy.* S. 28.

[62]. **Quinn, L.J., et al.** "Plasma-enhanced silicon nitride deposition for thin film transistor application". *Jurnal of Non-Crystalline Solids.* 1995, Vol. 187, S. 347-352.

[63]. **Rossnagel, S.M.** "Handbook of plasma processing technology : fundamentals, etching, deposition, and surface interactions". 1990 : s.n., S. 11.

[64]. **Coburn, J.W.** "Plasma chamistry nad plasma processing". 1982, Vol. 2, S. 1.

[65]. **Tarraf, A.** *"Low-Cost Micromechanically Tunable Optical Devices: Strained Resonator Engineering, Technological Implementation and Characterization", Thesis, Kassel University.* 2005.

[66]. **Kim, Y.J. und Boo, J.H.** "Effects of showerhead shapes on the flowfields in a RF-PECVD reactor". *Surface & Coatings Technology 193.* 2005, S. 88-93.

[67]. **Reinberg, A.R.** Electrochem. Soc. Extend. Abstr. No. 74-1. 1974, S. 4.

[68]. **Tarraf, A., et al.** "Stress investigation of PECVD dielectric layers for advanced optical MEMS". *J. Micromech. Microeng. 14.* 2004, S. 317–323.

[69]. **Konuma, M.** "Film deposition by plasma technology". *Vakuum in Forschung und Praxis.* 1992, S. 53 - 54.

[70]. **Lanford, W.A. und Rand, M.J.** *J. Appl. Phys. 49.* 1978, S. 2473.

[71]. **Claassen, W., Valkenburg, W. und Willemsen, M.** *J. Electrochem. Soc., 132.* 1985, S. 893.

[72]. **Cotler, T.J. und Chapple-Sokol, J.** *J. Electrochem. Soc., 140.* 1993, S. 2071.

[73]. **Maeda, N. und Nakamura, H.** *J. Appl. Phys., 58.* 1985, S. 484.

[74]. **Samuelson, G.M. und Mar, K.M.** *J. Electrochem. Soc., 129.* 1982, S. 1773.

[75]. **Habraken, F.H.P.M. und Kuiper, A.E.T.** "Silicon nitride and oxynitride films". *Materials Science and Engineering.* 1994, S. 130-139.

[76]. **Hillmer, H., et al.** "Micromachined tunable 1.55µm vertical cavity, multiple aur-gap filters and lasers: fabrication, characterisation, scaling potential and application". *technical Digest, OECC/IOOC 2007 Yokohama, 12E2-1.* S. 428.

[77]. **Hillmer, H., et al.** "Potential for micromachined actuation of ultra-wide continuously tunable optoelectronic devices". *Appl. Phys. B.* Vol. 75, S. 3-13.

[78]. **Hasse, A., et al.** "Wide continuous tuning range of 221 nm by InP/air-gap vertical-cavity filters". *Electronics Letters.* 17. August 2006, Vol. 42, 17.

[79]. **Kasap, S.O.** "Optoelectronics and photonics : principles and practices". 2001, S. 1.

[80]. **Macleod, H.A.** "Thin-film optical filters". 2001, S. 37.

[81]. **Pervak, V.Y. und Poperenko, L.V.** "Wide-band Interference filters with suppresion of the 5th-7th-order reflection bands". *Journal of Applied Spectroscopy.* 2005, Vol. 72, 5, S. 751-756.

[82]. **Salbeck, J.** "New low molecular organic compounds with high glass transition temperature as materials for blue electroluminescence". *Inorganic and Organic Electroluminescence /EL96 Berlin.* 1996, S. 243-246.

[83]. **Spehr, T, et al.** "Highly efficient light emitters based on the spiro concept". *Organic Electronics.* 2003, Vol. 4, S. 61-69.

[84]. **Pisignano, D., et al.** "Amplified spontaneous emission from a conjugated polymer undergone a high-temperature lithigraphy cycle". *Applied Physics Letters.* 2005, Vol. 86, 261104, S. 261104-1 - 261104-3.

[85]. **Brackmann, Ulrich.** "Laser Dyes". *Dyes.* Götingen : Lambda Physik AG, 2000, S. 4.

[86]. **Koschorreck, M., et al.** "Dynamics of a high-Q vertical-cavity organic laser". *Applied Physics Letters.* 2005, Vol. 87, S. 181108-1 - 181108-3.

[87]. **Valeur, B.** "Absorption of UV-visible light". *"Molecular fluorescence - Principles and Applications".* Weinheim : WILEY-VCH Verlag GmbH, 2002, S. 363-429.

[88]. **Hillmer, H., Hansmann, S. und Burkhard, H.** "Facet influence on wavelength tunability and linewidth chirp in InGaAs/InAlGaAs quantum-well distributed feedback lasers under high-bit-rate modulation". *Optical Engineering.* 1995, Vol. 34, 10, S. 2985-2992.

[89]. **Hillmer, H., et al.** "Continuously chirped DFB gratings by specially bent waveguides for tunable lasers". *Jurnal of Lightwave Technology.* September 1995, Vol. 13, 9, S. 1905-1912.

[90]. **Schwarz, J., Butendeich, R. und Schweizer, H.** "Interpretation of VCSEL reflectivity spectra as longitudinal resonances in VCSELs". [Online] http://www.physik.uni-stuttgart.de/ExPhys/4.Phys.Inst./en/.

[91]. **Hillmer, H.** *Patent: Komplex gekoppelter Laser. DE 103 31 586* 2003.

[92]. **Hillmer, Hartmut, et al.** "Lasers and Coherent Light Sources". *"Springer handbook of lasers and optics".* New York : Springer, 2007, S. 583-864.

[93]. **Svelto, Orazio.** *"Principles of Lasers-Fourth edition".* 1998.

[94]. **Kogelnok, H. und Shank, C.V.** "Stimulated Emission in a Periodic Structure". *Appl. Phys. Letters 18.* 1971, S. 152.

[95]. **Kogelnik, H. und Shank, C.V.** "Coupled-wave theory of distributed Feedback lasers". *J. Appl. Phys.* 1972, Vol. 43, 5, S. 2327-2335.

[96]. **Hillmer, H., et al.** "Ultrahigh resolution chirped distributed feedback gratings fabricated by electron-beam lithography using bent waveguides for low-cost photonic components". *J. Vac. Sci. Technol. B.* 1995, Vol. 13, 6, S. 2853-2858.

[97]. **Hillmer, H., et al.** "Tailored DFB laser properties by individually chirped gratings using bent waveguedes". *IEEE Jurnal of Selected Topics in Quantum Electronics.* June 1995, Vol. 1, 2, S. 356-362.

[98]. **Haus, H. A. und Shank, C. V.** "Antisymmetric Taperof Distributed Feedback Lasersy". *IEEE J. Quantum Electron. QE-12.* 1976, S. 532.

[99]. **Alvisi, M., et al.** "Ion assistance effects on electron beame deposited MgF2 films". *J. Vac. Sci. Technol. A.* 2002, Vol. 20, 3, S. 714-720.

[100]. **Dumas, L., et al.** "Optical properties of magnesium fluoride thin films produced by argon ion-beam assisted deposition". *J. Vac. Sci. Technol. A.* 2002, Vol. 20, 1, S. 102-106.

[101]. **Larruquert, J.I. und Keski-Kuha, R.A.M.** "Far ultraviolet optical properties of MgF2 films deposited by ion-beam sputtering and their application as protactive coatings for Al". *Optics Communications.* 2003, Vol. 215, S. 93-99.

[102]. **Quesnel, E., et al.** "Optical and microstructural propeties of MgF2 UV coatings grown by ion beam sputtering process". *J. Vac. Sci. Technol. A: Vacuum, surfaces, and films.* 2000, Vol. 18, 6, S. 2869-2876.

[103]. **Ouellette, M.F., et al.** "Experimental studies of inhomogeneous coatings for optical applications". *Journal of Vacuum Science & Technology A: Vacuum, Surfaces, and Films.* May 1991, Vol. 9, 3, S. 1188-1192.

[104]. **Al-Robaee, M.S., et al.** "Properties of Al2O3 films prepared by argon ion assisted deposition". *Journal of Materials Resurch.* 1996, Vol. 9, 10, S. 2688.

[105]. **Daugy, E., et al.** "Dependence between optical and chemical propeties of Y2O3 and ZrO2 thin films produced by ion beam sputtering". *J. Optics.* 1990, Vol. 21, 3, S. 99-106.

[106]. **Gaboriaud, R.J., Pailloux, F. und Paumier, F.** "Yttrium oxide thin films, Y2O3, grown by ion beam sputterign of Si". *J. Phys. D: Appl. Phys.* 2000, Vol. 33, S. 2884-2889.

[107]. **Jensen, T.R., Warren, J. und Johnson, R.L.** "Ion-Assisted Deposition of Moisture-Stable Hafnium Oxide Films for Ultraviolet Applications". *Appl. Opt.* 2002, Vol. 41, S. 3205-3210.

[108]. **Miyata, N.** "Two-step behavior of initial oxidation at HfO2 /Si interface". *APPLIED PHYSICS LETTERS.* 2006, Vol. 89, S. 102903-1 - 102903-3.

[109]. **Riviére, J.P., et al.** "Strusture of ZrO2 optical thin films prepared by dual ion beam reactive sputter deposition". *Surface and Coatings Technology.* 1996, Vol. 84, 1-3, S. 470-475.

[110]. **Zhang, D., et al.** "Laser-induced damage threshold of ZrO2 thin films prepared at different oxygen partial pressures by electron-beam evaporation". *J. Vac. Sci. Technol. A.* 2005, Vol. 23, 1, S. 197-200.

[111]. **Cho, H.J. und Hwangbo, C.K.** "Optical ingomogeneity and microstructure of ZrO2 thn films prapared by ion-assisted deposition". *Appl. Opt.* 1996, Vol. 35, S. 5545-5552.

[112]. **Abe, Y., et al.** "Target surface oxide layer formed by reactive sputtering of Ti target in Ar+O2 mixed gas". *J. Vac. Sci. Technol. A.* Sept/Oct 2005, Vol. 23, 5, S. 1371-1374.

[113]. **Alayo, M. und Pereyra, I.** "Improvement of the structural Properties of near stoichiometric PECVD SiO2". *Brazilian Jurnal of Physics.* 4. December 1997, Vol. 27/A, 4, S. 146-149.

[114]. **Kerr, M.J. und Cuevas, A.** "Recombination at the interface between silicon and stoichiometric plasma silicon nitride". *Semicond. Sci. Technol.* 2002, Vol. 17, S. 166-172.

[115]. **Han, G.C., et al.** "Growth and characterizatiion fo silicon nitride films on various underlying materials". *Appl. Phys. A.* 2002, Vol. 74, S. 243-247.

[116]. **Gottschalch, V., et al.** "Plasma-enhanced chemical vapor deposition of SiOx/SiNx Brag reflectors". *Thin Solid Films.* 2002, Vol. 416, S. 224-232.

[117]. **Müller-Wiegand, M, et al.** "Spinodal patterning in organic-inorganic hybrid layer systems". *Applied Physics Letters.* 2002, Vol. Volume 81, Number 26, S. 4940.

[118]. **Lin, S.C.H. und Pugacz-Muraszkiewicz, I.** "Local Stress Measurement in Thin Thermal SiO2 Film on Si Substrate". *J. Appl. Phys.* Vol. 43, 1972, 1.

[119]. **Chang, Shih-Chia und Hicks, D.B.** "The formation of microbridges on (100)-oriented silicon". *J. Micromech. Microeng.* 1990, Vol. 1, S. 25-29.

[120]. **Chichibu, S.F., et al.** "Dielectric SiO2/ZrO2 distributed Bragg reflectores for ZnO microcavities prepared by the reactive helicon-wave-excited-plasma sputtering method". *Applied Physical Letterss.* 2006, Vol. 88, S. 161914-1 - 161914-3.

[121]. **Bottiger, J., et al.** Radiat. Eff. 11. 1971, S. 69.

[122]. **Till Spehr**, Dissertation: "Fluoreszenz und Lasertätigkeit in dünnen amorphen Schichten von Spirobifluorenderivaten", University of Kassel, 2007

[123] **Ferdinand J. Messow**, Diplom: Entwicklung und Herstellung eines Vertical-Cavity Surface-Emitting-Laser mit ultraviolett emittierendem, organischem, aktivem Material, University of Kassel, 2008

Acknowledgements

My thanks go to:

Prof. Dr. Hartmut Hillmer for giving me the possibility to join his group, be my supervisor and for his support all-out the time of my PhD.

Prof. Dr. J. Salbeck (mmCmm) for the project cooperation and for accepting to be my second supervisor.

Dr. Martin Bartels for the scientific discussions and the creative ideas in the physic of the deposition processes.

Dipl.-Ing. Yanqi Wang for the discussions and the exchange of ideas.

Dr. Till Spehr und Dipl.-Chem. Cornelia Brendel for the support in the optical measurements and Dipl.-Chem. Thorsten Gerloff for the depositions of the organic materials.

Dipl.-Ing. Thomas Kusserow for reading and making comments and corrections on the manuscript and for the creative scientific discussions.

Dr.-Ing. Amer Tarraf for the discussions about the DIBS machine and sputtering processes.

Ina Wensch for the administrative support.

Ina Kommalein, Dietmar Gutermuth, Albert Malkomes, Michael Plätzer, Dirk Albert and Dr.Wenzel Scholz for the technical support.

The diplomands Vadim Daneker, Markus Schulz and Ferdinand Messow for the help in the scientific work and discussions.

The INA department and all my colleagues for the nice working atmosphere and support.

The mmCmm department for the organic active material used in this work and for the nice discussions.

Dr. Thomas Riedl and his coworkers from the group of Prof. Dr. Kowalsky, TU-Braunschweig, for the gain measurements

Nils Anspah from Genetic's Department for the AFM measurements

The Otto-Braun Foundation for the stipend during the first two years of my PhD time.

My wife for reading the thesis and correcting the grammar.

My parents and my brother for their support throughout the years.